Wavefront and nanostructure characterisation with X-ray ptychography

Author: Simone Sala
Supervisor: Prof. Pierre Thibault

A thesis submitted in fulfilment of the requirements for the degree of Doctor of Philosophy.

University College London
Department of Physics & Astronomy

September 2018

Declaration of Authorship

I, Simone Sala, confirm that the work presented in this thesis is my own. Where information has been derived from other sources, I confirm that this has been indicated in the thesis.

September 2018
Simone Sala

Abstract

X-ray ptychography is a scanning diffraction microscopy technique suited for the phase-sensitive investigation of wavefronts and specimens. It returns complex-valued wave functions and transmission functions producing high-resolution (nanoscale) phase-contrast images. This work focuses on the implementation and application of X-ray ptychography in the context of synchrotron radiation facilities.

It presents an experimental protocol developed for multiscale X-ray imaging and tested at the I13-1 Coherence Branchline at Diamond Light Source. This protocol combines both near-field and far-field ptychography with other imaging methods, providing a flexible way of conducting experiments on hierarchical structures at any high-brilliance X-ray facility.

This work also reports ptychography experiments performed at free-electron lasers, aimed at characterising their pulsed beam. Both the average and individual wavefronts are retrieved through a novel application of a reconstruction algorithm based on singular-value decomposition, giving direct insight on pulse-to-pulse fluctuations and confirming ptychography as a powerful beam diagnostics technique.

Additional ptychography experiments are also discussed, which were carried out at storage rings on flat, weakly-scattering biogenic samples to characterise their 3D nanostructures. Their data analysis pipeline is presented in detail, from data acquisition to rendered volumes. Furthermore, one of these last experiments constitutes the first successful 3D ptychography experiment run on real-life samples at the I13-1 Coherence Branchline at Diamond Light Source.

Impact statement

The results and the methodological developments presented in this work are expected to impact the fields of X-ray physics and synchrotron-based science.

The multiscale imaging experimental protocol, presented in Chapter 3, is intended to guide users of X-ray imaging beamlines in preparing and managing imaging experiments. Particular consideration is given to time-efficiency in achieving desired outcomes – namely field-of-view and resolution of retrieved images.

The novel application of the ptychographic reconstruction algorithm including a singular-value decomposition (SVD) step presented in Chapter 4 is the first of a new branch of wavefront characterisation experiments, of which pulsed X-ray sources are expected to be the main beneficiaries. In this study, it gave unprecedented insight into single femtosecond X-ray pulses delivered at two different end stations at free-electron lasers. It is foreseen that similar experiments exploiting the approach will soon be carried out at end stations worldwide, contributing to the commissioning and operation of free-electron lasers.

The quantitative 3D results presented in Chapter 5 provide information for ongoing studies in the field of evolutionary developmental biology and established a method now applicable to countless similar samples relevant to that field. Furthermore, the success of one of these experiments validated and demonstrated 3D X-ray ptychography on real-life samples for the first time at the I13-1 Coherence Branchline at Diamond Light Source, paving the way for similar experiments which will be carried out at that beamline in the future.

More broadly, all these experiments and results contribute to the body of knowledge available to the international X-ray imaging community, reducing the access barriers which non-specialist users currently face, which keep ptychography a high-investment technique – at least in terms of specialisation. These, together with future advancements, will lower these barriers and make this high-resolution phase-contrast imaging technique more widely and easily available, possibly even outside cutting-edge, large-scale research facilities.

Contents

List of Figures

Abbreviations

1D	one-dimensional / one dimension
2D	two-dimensional / two dimensions
3D	three-dimensional / three dimensions
AFM	**a**tomic-**f**orce **m**icroscopy
AMO	**A**tomic, **M**olecular and **O**ptical
ASIC	**a**pplication-**s**pecific **i**ntegrated **c**ircuit
BM	**b**ending **m**agnet
BW	**b**and**w**idth
CAT	**c**omputed **a**xial **t**omography / **c**omputer-**a**ided **t**omography
CCD	**c**harge-**c**oupled **d**evice
CDI	**c**oherent **d**iffraction **i**maging
CLS	**c**ompact **l**ight **s**ource
CMOS	**c**omplementary **m**etal-**o**xide-**s**emiconductor
CRL	**c**ompound **r**efractive **l**ens
CS	**c**entral **s**top
CSPAD	**C**ornell-**S**LAC **p**ixel **a**rray **d**etector
CT	**c**omputed **t**omography
CXI	**C**oherent **X**-ray **I**maging
DiProI	**Di**ffraction and **Pro**jection **I**maging
DLS	**D**iamond **L**ight **S**ource
DLSR	**d**iffraction-**l**imited **s**torage **r**ing
DM	**d**ifference **m**ap
EM	**e**lectron **m**icroscopy
ePIE	**e**xtended **p**tychographical **i**terative **e**ngine
ESRF	**E**uropean **S**ynchrotron **R**adiation **F**acility
EUV	**e**xtreme **u**ltra**v**iolet
FBP	**f**iltered **b**ack-**p**rojection
FEL	**f**ree-**e**lectron **l**aser
FERMI	**F**ree **E**lectron laser **R**adiation for **M**ultidisciplinary **I**nvestigations
FF	**f**ar-**f**ield

FFP **f**ar-**f**ield **p**tychography
FOV **f**ield-**o**f-**v**iew
FT **F**ourier **t**ransform
FWHM **f**ull **w**idth at **h**alf **m**aximum
FXI **f**lash **X**-ray **i**maging
FZP **F**resnel **z**one **p**late
HHG **h**igh **h**armonic **g**eneration
HWHM **h**alf **w**idth at **h**alf **m**aximum
ID **i**nsertion **d**evice
KB **K**irkpatrick **B**aez
LCLS **L**inac **C**oherent **L**ight **S**ource
linac **lin**ear **ac**celerator
LWFA laser **w**ake**f**ield **a**ccelerator
MBA **m**ultiple-**b**end **a**chromat
ML **m**aximum **l**ikelihood
NF **n**ear-**f**ield
NFP **n**ear-**f**ield **p**tychography
OPRP **o**rthogonal **p**robe **r**elaxation **p**tychography
ORC **O**ptoelectronics **R**esearch **C**entre
OSA **o**rder-**s**orting **a**perture
PBH **p**arallel-**b**eam **h**olography
PIE **p**tychographical **i**terative **e**ngine
PSF **p**oint **s**pread **f**unction
PXCT **p**tychographic **X**-ray **c**omputed **t**omography
RF **r**adio **f**requency
ROI **r**egion **o**f **i**nterest
SASE **s**elf-**a**mplified **s**pontaneous **e**mission
SEM **s**canning **e**lectron **m**icroscopy
SLAC **S**tanford **L**inear **A**ccelerator **C**enter
SLS **S**wiss **L**ight **S**ource
SPI **s**ingle **p**article **i**maging
STXM **s**canning **t**ransmission **X**-ray **m**icroscopy
SVD **s**ingular-**v**alue **d**ecomposition
TXM **t**ransmission **X**-ray **m**icroscopy
WFS **w**ave**f**ront **s**ensor
XAS **X**-ray **a**bsorption **s**pectroscopy
XFEL **X**-ray **f**ree-**e**lectron **l**aser
XRF **X**-**r**ay **f**luorescence

Chapter 1

Introduction

X-rays were discovered over a century ago (1895) by W. Röntgen who immediately carried out experiments on their interactions with matter, producing the much famous X-ray of his wife's hand, legitimately considered the first instance of medical X-ray imaging. Since then, X-rays have become increasingly relevant to the scientific endeavour as acknowledged by the awarding of several Nobel prizes to the field, e.g. W. Röntgen 1901, M. von Laue 1914, W. H. Bragg and W. L. Bragg 1915 and many others. X-ray crystallography has been one of the first techniques exploiting this new region of the electromagnetic spectrum and is still widely used today to determine the structure of periodic objects with atomic resolution, based on the diffraction patterns generated by the interaction of X-rays with the objects studied. This technique found applications throughout science and technology and in fields other than physics. For example the renowned "discoveries concerning the molecular structure of nucleic acids" (DNA) that led to the awarding of 1962's Nobel prize in Physiology or Medicine to F. Crick, J. Watson and M. Wilkins were largely based on X-ray crystallography experiments. Later, also the field of X-ray microscopy developed, bridging the resolution gap between visible light and electron microscopy and at the same time offering the great advantage over these other techniques of a larger penetration depth which makes the imaging of bulk materials accessible.

As in the very first images generated using X-rays and produced by their discoverer, the most straightforward interaction of X-rays with matter exploited for imaging purposes is absorption. However, the most advanced X-ray imaging methods are based on refraction which can deliver better contrast and resolution. In fact the component of the refraction index determining the angle of refraction is typically orders of magnitude larger than the component related to absorption, as discussed later (cf Chapter 2). This effect is more significant for light elements and hard X-rays, which in turn translates to a higher contrast being achievable exploiting refraction rather than absorption. This leads to the

field of X-ray imaging techniques known as phase-contrast imaging based on concepts first applied in visible light and electron microscopy and of which wider reviews are available (Momose, 2005).

Diffraction imaging was conceived as a way of solving the phase problem and returning real space images via inverse Fourier transformation of the complex-valued diffraction patterns generated by the interaction of X-rays, or other kinds of radiation, with the imaged object. This was based on ideas first brought up by Hoppe (1969) and Hegerl and Hoppe (1970). The technique grew thanks to the development of iterative phase retrieval algorithms (Fienup, 1978), based on previous work by Gerchberg and Saxton (1972). At first, these were only available for isolated objects (Miao et al., 1999) and were later applied to extended ones (Faulkner and Rodenburg, 2004; Rodenburg and Faulkner, 2004) in the form of a lensless scanning X-ray diffraction microscopy technique known as ptychography. In order to provide reconstructions of complex-valued images of objects, they relied on in-depth knowledge of the probe, i.e. the complex-valued wavefront of the coherent radiation impinging on those objects. This limitation was overcome with the introduction of new reconstruction algorithms which do not require any *a priori* knowledge on either object and probe (Thibault et al., 2009; Maiden and Rodenburg, 2009). Currently X-ray ptychography is able to routinely produce images of objects with submicron resolution (Holler et al., 2014) and simultaneously deal with issues of partial coherence in the probe (Thibault and Menzel, 2013; Enders et al., 2014). Details and applications of these features are discussed in the following chapters.

It is also worth noting that the availability of high brilliance sources, such as synchrotron sources at storage rings around the world, led to the success of many of the most cutting-edge X-ray -based experiments which would be unfeasible otherwise. Furthermore, for little under a decade X-ray free-electron laser (XFEL) facilities have started operation, open to users from the worldwide X-ray community. This has opened the doors to a new realm of experiments ranging from ultrafast science to single particle imaging and flash imaging experiments and raised new challenges such as that of the characterisation of the high-brilliance X-ray beams produced by FELs. In fact these XFEL beams are so bright that it is non-trivial to detect them both accurately and non-destructively.

This work is centred around ptychography, its development as an X-ray imaging technique and its applications. It is structured such that Chapter 2 builds its theoretical foundations, summarising and providing references to the body of knowledge necessary to tackle the subsequent chapters. The concepts presented therein are drawn from established knowledge and published research. Chapter 3 describes an experimental protocol developed as a flexible tool to perform X-ray imaging experiments at a wide range of

length scales exploiting ptychography to obtain images at the highest resolutions among those achievable via phase-contrast techniques. General considerations are backed up with experimental results, both published in Sala et al. (2018). Chapter 4 presents the application of ptychography in a novel implementation based on singular-value decomposition (SVD) applied to the problem of wavefront characterisation at high-brilliance pulsed sources. This issue is of interest for the wider XFEL community and the developed approach has been proven successful in retrieving single-pulse information, providing unprecedented insight. At the time of writing, part of these results have been gathered into a manuscript ready to be submitted to a peer-reviewed journal. Chapter 5 focuses on the application of X-ray ptychography for the high-resolution phase-contrast quantitative characterisation of nanostructures found in butterfly wing scales. Experimental results are presented from data suited for tomographic analysis and the whole data analysis pipeline is discussed, leading to 3D characterisation of the butterfly scales. One of these experiments also validated ptychographic X-ray computed tomography (PXCT) on real-life samples at the I13-1 Coherence Branchline at Diamond Light Source for the first time and has been made into a manuscript undergoing peer-review at the time of writing. Finally, Chapter 6 draws the general conclusions by summarising the main results presented in this work and their wider implications.

1.1 Contributions

A significant fraction of the novel research presented in this work stems from studies carried out within the framework of wider international collaborations. As with most impact-bearing research in modern science, this work was only possible within such framework and whenever individual contributions could be assigned, this has been explicitly pointed out.

The local teams of each of the large-scale facilities involved were solely responsible for beamlines being in working conditions and provided support throughout each experiment. These were staff from the I13-1 Coherence Branchline at Diamond Light Source (DLS) (Chapters 3,5), the Atomic, Molecular and Optical (AMO) and the Coherent X-ray Imaging (CXI) end stations at the Linac Coherent Light Source (LCLS) (Chapter 4), the Diffraction and Projection Imaging (DiProI) beamline at the Free Electron laser Radiation for Multidisciplinary Investigations (FERMI) facility (Chapter 4) and the ID16A Nano-Imaging beamline at the European Synchrotron Radiation Facility (ESRF) (Chapter 5).

Measurements at storage rings (Chapters 3,5) were supported by members of the X-ray Nano-imaging Group (XNIG) of University College London (UCL) and the University of Southampton. Measurements at free-electron lasers (Chapter 4) were supported

by members of the Molecular Biophysics group of Uppsala University, the Centre for Bioimaging Sciences (CBIS) of the National University of Singapore (NUS) and the Optoelectronics Research Centre (ORC) of the University of Southampton.

The collaborators from Uppsala University were also responsible for carrying out the pre-characterisation of the test pattern via SEM as well as most of the pre-processing on raw data collected at LCLS. Michal Odstrcil from the University of Southampton contributed to the pre-processing on raw data collected at FERMI. Anupama Prakash from the National University of Singapore (NUS) was responsible for collecting SEM images of the butterfly scales.

This is further detailed in the text where appropriate.

Chapter 2

Nibbles of X-ray physics

This chapter presents a wide variety of topics related to X-rays in general and ptychography in particular. Many concepts are briefly touched on which all belong to a wider body of established knowledge which does not constitute an original contribution of this work but is however instrumental in setting the basis for the following chapters. First (Section 2.1) an overview of X-ray waves is given including some of the ways they interact with matter which are relevant to this work. The discussion then moves on to X-ray sources (Section 2.2) with particular attention to synchrotron radiation from both storage rings and free-electron lasers as this has been the one used to carry out all experiments figuring in this work. A brief overview of scanning transmission X-ray microscopy appears (Section 2.3) followed by a more extensive discussion on ptychography (Section 2.4) which is the main imaging technique both used and developed within this work. Phase-retrieval algorithms are presented, along with a few of the several developments that ptychography saw within the past decade. Finally, some concepts in tomography are introduced (Section 2.5) as that is the technique commonly exploited to achieve 3D imaging.

As many of the notions discussed are considered common knowledge in the field, explicit reference to an original source is sometimes not provided. Wherever that is the case, the reader should refer to common handbooks in the field, such as Als-Nielsen and McMorrow (2011) or Willmott (2011).

2.1 X-rays

2.1.1 Wave theory

Maxwell's equations describe the classical theory of electrodynamics and for the case of electric $\mathbf{E}(x, y, z, t)$ and magnetic $\mathbf{B}(x, y, z, t)$ fields in vacuum they read

$$\begin{aligned} \nabla \cdot \mathbf{E} &= 0 \\ \nabla \cdot \mathbf{B} &= 0 \\ \nabla \times \mathbf{E} &= -\frac{\partial \mathbf{B}}{\partial t} \\ \nabla \times \mathbf{B} &= \varepsilon_0 \mu_0 \frac{\partial \mathbf{E}}{\partial t} \end{aligned} \tag{2.1}$$

where ε_0 and μ_0 are respectively the electrical permittivity and magnetic permeability of free space. Exploiting the mathematical identity

$$\nabla \times (\nabla \times \mathbf{f}) = \nabla(\nabla \cdot \mathbf{f}) - \nabla^2 \mathbf{f} \tag{2.2}$$

and keeping in mind that the speed of light in vacuum $c = 1/\sqrt{\varepsilon_0 \mu_0}$, one can rearrange Maxwell's equations to obtain

$$\begin{aligned} \frac{1}{c^2}\frac{\partial^2 \mathbf{E}}{\partial t^2} - \nabla^2 \mathbf{E} &= 0 \\ \frac{1}{c^2}\frac{\partial^2 \mathbf{B}}{\partial t^2} - \nabla^2 \mathbf{B} &= 0 \end{aligned} \tag{2.3}$$

which are partial differential equations of the form of d'Alembert wave equation and can be represented in scalar theory using the single complex scalar $\Psi(x, y, z, t)$ associated to the electromagnetic disturbance as

$$\left(\frac{1}{c^2}\frac{\partial^2}{\partial t^2} - \nabla^2\right)\Psi = 0\,. \tag{2.4}$$

Solutions Ψ to this equation represent electromagnetic waves propagating in free-space.

Applying some spectral decomposition to Ψ through a Fourier integral, one gets

$$\Psi(x, y, z, t) = \frac{1}{\sqrt{2\pi}} \int_0^\infty \psi_\omega(x, y, z) e^{-i\omega t} \mathrm{d}\omega \tag{2.5}$$

including the angular frequency ω.

Substituting Eq. 2.5 into Eq. 2.4 then gives

$$\int_0^\infty \left[\left(\nabla^2 + \frac{\omega^2}{c^2}\right)\psi_\omega(x, y, z)\right] e^{-i\omega t} \mathrm{d}\omega = 0\,. \tag{2.6}$$

Therefore considering the wavelength λ and plugging in the wavevector $k = 2\pi/\lambda = \omega/c$ one can infer

$$(\nabla^2 + k^2)\psi_\omega(x, y, z) = 0 \tag{2.7}$$

which is the time-independent form of the wave equation known as Helmholtz equation. For a monochromatic wave propagating into a medium Eq. 2.7 reads

$$\nabla^2\psi + k^2 n^2 \psi = 0 \tag{2.8}$$

where n is the refraction index discussed later (Section 2.1.3).

A possible solution of Helmholtz equation is that of a plane wave. Such plane wave propagates along the direction $\mathbf{r}(x, y, z)$ following

$$\psi(x, y, z) = e^{i(k_x x + k_y y + k_z z)} \tag{2.9}$$

with $k_x^2 + k_y^2 + k_z^2 = k^2$.

Rearranging for $k_z = \sqrt{k^2 - k_x^2 - k_y^2}$ one can write such a plane wave at an arbitrary position z_0 as

$$\psi(x, y, z_0) = e^{i(k_x x + k_y y)} e^{iz_0\sqrt{k^2 - k_x^2 - k_y^2}} \tag{2.10}$$

where the second component on the right-hand side is a form of the free-space propagator

$$P^{\text{free space}} = e^{iz_0\sqrt{k^2 - k_x^2 - k_y^2}}. \tag{2.11}$$

Using Fourier decomposition one can represent any monochromatic wavefield as a linear combination of plane waves. At an initial position $z = 0$ this reads

$$\psi(x, y, 0) = \frac{1}{2\pi} \iint \tilde{\psi}(k_x, k_y, 0) e^{i(k_x x + k_y y)} \mathrm{d}k_x \mathrm{d}k_y \tag{2.12}$$

where $\tilde{\psi}$ denotes the Fourier transform (FT) operation $\mathcal{F}\psi$.

Inserting 2.11 into this equation leads to the wavefield at the position $z_0 > 0$, i.e. propagated along the axis z by the distance z_0. One can then define an operator $\mathcal{P}_{z_0}$ such that applied to an arbitrary monochromatic wavefield it would return the free-space propagated wavefield at a distance z_0 in the x-y plane

$$\mathcal{P}_{z_0} = \mathcal{F}^{-1} P^{\text{free space}} \mathcal{F} = \mathcal{F}^{-1} e^{iz_0\sqrt{k^2 - k_x^2 - k_y^2}} \mathcal{F} \tag{2.13}$$

which is another form of the free-space propagator.

This can be seen as the general operator for free-space diffraction. A special case is that of Fresnel diffraction which is diffraction occurring in the near-field while the following paraxial approximation holds. If one considers Fresnel number $N_F = a^2/z_0\lambda$

where a is the characteristic dimension of the source of radiation typically referring to an aperture size, then a propagation distance z_0 such that $N_F \approx 1$ is said to be in the near-field propagation regime. Furthermore when $|k_x| \ll k_z$ and $|k_y| \ll k_z$ the wavefield is said to be paraxial and the following binomial approximation holds

$$\sqrt{k^2 - k_x^2 - k_y^2} \approx k - \frac{k_x^2 + k_y^2}{2k} \tag{2.14}$$

and $\mathcal{P}_{z_0}$ becomes

$$\mathcal{P}_{z_0}^{\text{Fresnel}} = e^{ikz_0}\mathcal{F}^{-1}e^{\frac{-iz_0(k_x^2+k_y^2)}{2k}}\mathcal{F} \tag{2.15}$$

where the free-space propagator has been substituted by the Fresnel propagator.

As in the general case, one can rewrite the operation as a convolution

$$\psi(x, y, z_0) = \mathcal{P}_{z_0}^{\text{Fresnel}}\psi(x, y, 0) = \psi(x, y, 0) * P^{\text{Fresnel}}(x, y, z_0) \tag{2.16}$$

where $P^{\text{Fresnel}}(x, y, z_0)$ is the real-space form of the Fresnel propagator

$$P^{\text{Fresnel}}(x, y, z_0) = -\frac{ike^{ikz_0}}{2\pi z_0}e^{\frac{ik(x^2+y^2)}{2z_0}}. \tag{2.17}$$

Fresnel diffraction then reads

$$\psi(x, y, z_0) = -\frac{ike^{ikz_0}}{2\pi z_0}\left[\psi(x, y, 0) * e^{\frac{ik(x^2+y^2)}{2z_0}}\right] \tag{2.18}$$

which is a mathematical representation of Huygens-Fresnel principle stating that the propagation of a wavefield $\psi(x, y, z_0)$ can be represented as the coherent superposition of spherical waves originating at every point of the initial wavefront $\psi(x, y, 0)$.

Turning now to the far-field case for which the Fresnel number $N_F \ll 1$, one obtains Fraunhofer diffraction

$$\psi(x, y, z_0) \approx -\frac{ike^{ikz_0}}{2\pi z_0}e^{\frac{ik(x^2+y^2)}{2z_0}} \times \iint_{-\infty}^{\infty}\psi(x', y', 0)e^{\frac{-ik(xx'+yy')}{z_0}}\mathrm{d}x'\mathrm{d}y' \tag{2.19}$$

which can be written as

$$\psi(x, y, z_0) \approx A \times \tilde{\psi}(kx/z_0, ky/z_0, 0) \tag{2.20}$$

with

$$A = -\frac{ike^{ikz_0}}{z_0}e^{\frac{ik(x^2+y^2)}{2z_0}}. \tag{2.21}$$

This shows how in the far-field limit the free-space propagated diffraction pattern is a transversely scaled version of the 2D Fourier transform of the initial wavefield $\psi(x, y, 0)$

multiplied by a phase factor and a paraxial spherical wave described by A.

The wave theory just presented holds for any kind of electromagnetic wave and is solely based on a classical description of such phenomenon. It is therefore relevant to recall the quantised nature of radiation which describes electromagnetic waves as made up of photons and states the relationship between the energy E carried by each photon and its wavelength λ and frequency ν

$$E = h\nu = hc/\lambda \tag{2.22}$$

where h is Planck's constant and c the speed of light in vacuum.

Furthermore, this text mainly focuses on X-rays which refer to only a limited energy range of the electromagnetic spectrum which spans roughly from 100 eV ($\sim$ 12 nm) to 100 keV ($\sim$ 12 pm). This range is further divided into soft and hard X-rays where the former typically carry energies below 2-5 keV and the latter above 5-10 keV. Sometimes the intermediate range between soft and hard X-rays (1-10 keV) is referred to as tender X-rays. Finally the 10-100 eV energy range is often called extreme ultraviolet (EUV), especially within the laser users community.

2.1.2 Coherence

The discussion so far treated the ideal case of parallel and monochromatic plane waves as initial wavefield $\psi(x, y, 0)$ which can be said to be fully coherent. The beams available for any experiment however deviate from the ideal case so the concept of coherence length becomes a useful estimate of such a deviation. Given two plane waves in phase at the source, the transverse and longitudinal coherence lengths define at which distance, perpendicular and parallel to the optical axis respectively, such waves will be out of phase.

The transverse (or spatial) coherence length ξ_t describes the effect of the divergence of different plane waves composing a beam and is defined as

$$\xi_t = \frac{1}{2}\frac{\lambda R}{D} \tag{2.23}$$

with λ as the wavelength, R as the distance from the source and D as the distance between point sources which corresponds to the characteristic size a of the source. One can further distinguish between vertical and horizontal coherence lengths which differ for most experiments.

On the other hand the longitudinal (or temporal) coherence length ξ_l describes the effect of the polychromaticity of the beam and is roughly identified by

$$\xi_l \approx \frac{1}{2}\frac{\lambda^2}{\Delta\lambda} \tag{2.24}$$

where $\Delta\lambda$ represents the difference in wavelength between two waves and is related to the bandwidth of the beam which in turn is defined by the energy resolution $\Delta\lambda/\lambda$ of the monochromator. In fact, most X-ray experiments use of monochromators, even those exploiting X-ray sources with naturally narrow emission spectra, such as undulators (cf Section 2.2.1).

The concept of coherence length is useful as it determines the largest distance between scatterers for them to be able to generate interference effects which is a requirement of several experiments. In the limit of a completely incoherent beam no interference is produced and the total scattered intensity is just the sum of the contribution of each individual scatterer, whilst in the limit of a fully coherent beam interference occurs. In the intermediate cases the beam is said to be partially coherent and often interference fringes are visible though blurred. This latter condition is very common experimentally and can still be used for some diffraction experiments which would normally require highly coherent beams, as it will be discussed in Section 2.4.

2.1.3 Interaction with matter

In optics in general, the index of refraction n is a useful concept used to deal with radiation at the interface between different media. It already appeared in Helmholtz equation (Eq. 2.8) and for X-rays it is commonly defined as

$$n = 1 - \delta + i\beta \tag{2.25}$$

where β is related to absorption and δ to refraction. The latter also has a direct relation to the phase shift φ a wave experiences while travelling through a medium along the optical axis z:

$$\varphi = k \int \delta(x, y, z)\mathrm{d}z\,. \tag{2.26}$$

The main categories of radiation-matter interaction are now briefly outlined which are routinely exploited in different ways within X-ray imaging experiments. Some are used as contrast mechanism to form pixelated images and some are used within focusing devices to manipulate X-ray beams, especially with the purpose of concentrating coherent radiation within a limited area. This is not intended as an exhaustive list of all kinds of known radiation-matter interactions.

In classical optics, when waves encounter an interface they experience reflection and refraction. This is due to elastic scattering or Thomson scattering which, for X-rays, causes scattered waves to preserve their amplitude and undergo a phase shift of π. Both of these types of interaction affect X-rays when exploited within experiments involving interfaces between some external environment – typically vacuum or some low-interacting fluid, such as air – and, for instance, a sample. As in the sub-UV range materials usually show an index of refraction smaller than unity, this leads to the occurrence of a critical angle $\alpha_c = \sqrt{2\delta}$ below which grazing incident X-rays undergo total external reflection. This is the physical principle on which Kirkpatrick Baez (KB) focusing mirrors are based (Kirkpatrick and Baez, 1948). These are highly polished mirrors – not rarely down to the atomic scale – designed with a very low curvature in order to achieve total external reflection and therefore focus X-rays along a specific direction. They are typically used in pairs, i.e. to focus X-rays along both directions perpendicular to the optical axis.

Unless they undergo total external reflection, X-rays at an interface also experience refraction. This too can be treated with classical geometric optics – and Snell's law in particular – and be interpreted as a change in the propagation direction of a wave caused by a change in the refraction index of the medium, i.e. at an interface. As it depends on the medium-dependent δ factor of the refraction index, morphological information on a material can be retrieved exploiting this interaction. This is the principle on which the phase-contrast methods outlined in Section 2.3 are based, which are sensitive to the small angular deviation of an X-ray beam caused by refractive interaction with a specimen.

Refraction is also the principle on which focusing lenses are based. In fact, as for visible light ($n > 1$) there exist convex lenses focusing such radiation, so for X-rays ($n < 1$) compound refractive lenses (CRLs) have been designed which are arrays of concave lenses able to focus the weakly refracted X-rays (Snigirev et al., 1996).

Absorption is another kind of radiation-matter interaction and occurs whenever a photon is captured by a charged particle such as an electron in an atom and is then annihilated. Together with Compton scattering which becomes more relevant at high energies, this phenomenon accounts for the attenuation that radiation undergoes whenever travelling through a medium. Some useful formalism to describe attenuation is summarised by Lambert-Beer law

$$I(z) = I_0 e^{-\mu z} \tag{2.27}$$

with I and I_0 being respectively the intensity of the radiation at z and $z = 0$ assuming the radiation is propagating along the z direction and μ representing the medium-specific

and wavelength-dependent absorption coefficient. This latter has a direct relation with the imaginary part of the refraction index n through $\mu = 2k\beta$.

Finally, when radiation is scattered by an inhomogeneous medium, interference phenomena lead to diffraction. This is the product of wave-wave interaction but arises in the presence of scatterers and can hence be considered the indirect product of radiation-matter interaction. Diffraction has already been implicitly used in Section 2.1.1 and can be described as the special case of refraction where interference between multiple waves occurs according to Huygens-Fresnel principle. It is the physical principle on which diffraction X-ray imaging techniques are based as well as Fresnel zone plates (FZPs) (Baez, 1961), which are another kind of focusing optics suited for X-rays and frequently used in imaging experiments.

Diffraction is also the foundation of X-ray crystallography which shares with X-ray diffraction imaging the so-called phase problem. Upon measurement, the information regarding the phase of a complex-valued function such as a wavefunction is lost. In an ideal probe-object interaction, the probe $P(x, y)$ is the complex-valued function representing the wavefront as it is just before interacting with the specimen, while the object $O(x, y)$ is the complex-valued transmission function of the specimen and accounts for both the absorption and the phase shift that radiation undergoes while travelling through the specimen. This latter is a solution of the inhomogeneous Helmholtz equation (Eq. 2.8) and it reads

$$O(x, y) = e^{ik\int[n(x,y)-1]\mathrm{d}z} = e^{-k\int\beta(x,y)\mathrm{d}z}e^{-ik\int\delta(x,y)\mathrm{d}z}\,. \tag{2.28}$$

Recording the wavefront right after the object corresponds to measuring the modulus squared of the exit wave $\psi(x, y, z) = P(x, y, z) \cdot O(x, y, z)$, so that

$$I(x, y, z) = \left|\psi\right|^2 = \psi\,\psi^\star = (PP^\star)e^{-2k\int\beta\,\mathrm{d}z} \tag{2.29}$$

where the phase factor $e^{-ik\int\delta(x,y)\mathrm{d}z} = e^{i\varphi}$ disappeared.

Recognizing $I_0 = PP^\star$, Eq. 2.29 clearly is a more general version of Lambert-Beer law which for a homogenous sample becomes again Eq. 2.27 via $2k\int\beta\mathrm{d}z = 2k\beta z = \mu z$.

This simple example shows how the phase component of the exit wave is lost in an X-ray diffraction experiment while the absorption component is preserved and can therefore be measured in a more straightforward way. Nonetheless as the phase information is necessary to fully characterise the complex-valued exit wave, only solving the phase problem can return the full information carried by the complex-valued transmission function of the object.

2.2 X-ray sources

Since their discovery by Röntgen in 1895, X-rays have become a widespread tool in modern science and technology so that interest continues to be maintained into improving existing sources and designing new ones. The first X-ray sources were X-ray tubes of the kind used by Röntgen and later improved and somehow standardised by Coolidge. These see the electrons emitted by a glowing filament accelerated through an evacuated tube towards a metal anode acting as a target. The interaction between the electrons and the target generates electromagnetic radiation within the X-ray spectrum through two mechanisms. One is *bremsstrahlung* or braking radiation which produces a continuous spectrum with its highest energy determined by the tube's voltage. The other is fluorescent emission by core vacancies induced in the target which produces sharp peaks, typically significantly more intense than the *bremsstrahlung*, whose energy depends on the excited elements. X-ray flux increases by increasing the number of electrons reaching the target, i.e. by increasing the current through the filament. However for this kind of setup the limiting factor is overheating of the water-cooled metal target which an excessive electron flux would melt or damage. In the 1960s a significant improvement on this design came along by establishing a rotating anode: conceptually identical to the X-ray tube, the rotation of the metal target offers more surface to the electrons making it a more thermally stable X-ray source and hence bringing up the X-ray flux it can produce. In the 2000s a further step in the same direction was made with the design of the first liquid-metal-jet anode X-ray sources which exploiting a continuously regenerated liquid target increase both anode speed and thermal load limit leading to the generation of an X-ray flux at least two orders of magnitude higher than with the previous rotating anode design (Hemberg et al., 2003).

In order to describe and compare different X-ray sources, it is now useful to introduce the concept of brilliance or brightness. Brilliance is a conventional figure of merit that describes the quality of an X-ray beam and is defined taking into account several factors typically relevant when running X-ray experiments, namely flux, emittance and bandwidth. The flux is as usual $\Phi = \mathrm{d}N_{ph}/\mathrm{d}t$, the emittance corresponds to the product of the beam divergence (or collimation) relative to the propagation axis z and the source $\varepsilon = \delta\theta\,\sigma$ and for the energy bandwidth (BW) conventionally 0.1% is taken as a relative value. This gives

$$\text{brilliance} = \frac{\Phi[\mathrm{s}^{-1}]}{\delta\theta_x\delta\theta_y[\mathrm{mrad}^2]\;\sigma_x\sigma_y[\mathrm{mm}^2]\;(0.1\%\;\mathrm{BW})} \tag{2.30}$$

and qualitatively implies that for the average X-ray experiment it is desirable to have many photons travelling parallel to each other, coming from a point source and carrying the same energy.

Using brilliance as a comparison tool one can assess the brilliance of a standard X-ray tube, a rotating anode and a liquid-metal-jet source at around 10^8, 10^9 and 10^{12} ph/s/mrad^2/mm^2/0.1%BW respectively.

2.2.1 Synchrotrons

It becomes then apparent how the anode-based sources presented so far could make a rather rudimental kind of X-ray source in many contexts. They in fact produce polychromatic X-rays in a wide solid angle. This explains why by the beginning of the 1960s with the coming of increasingly large particle accelerators some scientists started exploiting the synchrotron radiation produced by such machines in parasitic mode, i.e. by drilling holes through particle beam guides. Synchrotron radiation is the electromagnetic radiation that accelerated relativistic particle beams emit and was known since the 1940s based on mathematics by Liénard from the 1890s and mostly considered an unwanted yet intrinsic inefficiency of any circular accelerator. Its properties however were soon found so desirable that in the 1980s the first purposely-designed particle accelerators started to be built and operated which became known as 2nd generation synchrotron sources, to underline the improvement with respect to previous parasitic sources. 2nd generation sources are able to produce X-ray beams at least two orders of magnitude brighter than previous ones via bending magnets (BM), i.e. strong dipole magnets used to bend a particle beam – typically electrons – in order to keep it along a circular path. Fig. 2.1a shows part of a 2nd generation synchrotron source, removed from the particle accelerator for exhibition purposes. X-rays are emitted along the optical axis z each time a particle bunch travels through the bending magnet. The X-ray beam is delivered downstream via a photon guide while the particle beam keeps moving around a circular path within the particle guide after its trajectory has been bent.

By the 1990s, insertion devices (ID) were designed to fit within the straight sections in between bending magnets leading to the configuration of most synchrotron sources currently active worldwide. The further increase in terms of brilliance that insertion devices brought along with respect to the best bending magnets has been so significant – up to 6-7 orders of magnitude – that the synchrotron facilities exploiting them became known as 3rd generation sources.

Finally the multiple-bend achromat (MBA) concept initially developed in the 1990s (Einfeld et al., 2014) has been recently reconsidered for implementation (Hettel, 2014): it aims at reaching a photon beam emittance $\varepsilon = \delta\theta\,\sigma \leq \lambda/4\pi$, i.e. below the diffraction limit and is hence known as the diffraction-limited storage ring (DLSR) design. As DLSRs will have a smaller emittance and higher coherence than current synchrotrons, the achievable brilliance is expected to increase by 2 further orders of magnitude, enough

for such sources to constitute a 4th generation of sources. At the time of writing, there are 2 such facilities under commissioning and construction: respectively MAX IV in Sweden (Tavares et al., 2014) and Sirius in Brazil (Liu et al., 2014).

Again for the purpose of comparison, one can consider the increase in average brilliance among the different generation of synchrotron sources: from 1st to 4th, these are about 10^{12}, 10^{14}, 10^{20} and 10^{22} ph/s/mrad^2/mm^2/0.1%BW.

Most synchrotron sources operating today abide by 3rd generation layout in which a linear accelerator (linac) followed by a booster ring speed up electron bunches emitted by an electron gun. Electron bunches circulate the booster ring several times and are there accelerated to relativistic speed typically in the GeV range through magnetic fields synchronised with their increasing kinetic energy, hence the name synchrotron. Once reached the desired energy, electron bunches are injected into the storage ring, a large ring-shaped building so-named because originally its main purpose was to store the particle beam by preserving its energy. Storage rings still do so by exploiting radio frequency (RF) cavities which preserve the bunching and at the same time counterbalance for the kinetic energy lost through radiation at each lap. However they also host a number of other magnetic devices. Dipole magnets are used as bending magnets (BM) in order to keep the particle beam along a circular trajectory by at the same time causing it to emit continuous synchrotron radiation. Higher multipole magnets are also present, typically as quadrupole and sextupole magnets (cf Fig. 2.1a) where the former act in pairs to focus the particle beam along the two dimensions orthogonal to its average trajectory and the latter correct for chromatic aberrations caused by such focusing. Finally in the straight sections in between the other components wigglers and undulators are found – hence their name insertion devices (ID) – which are both made up of alternated static magnetic fields which cause the charged particles to oscillate or wiggle which, once more, causes them to emit synchrotron radiation. Fig. 2.1b shows the inside of an unmounted undulator with the electron bunches travelling along z, towards the viewer. When such charged particles experience the alternated vertical – i.e. along y – magnetic fields produced by the undulator's magnets they oscillate along x, emitting electromagnetic radiation.

As both bending magnets and insertion devices produce synchrotron radiation, a beamline is located tangentially downstream to each one of them. Beamlines are the radiation-controlled laboratories where synchrotron-based experiments take place, typically divided in three wide categories: diffraction, spectroscopy and imaging. The front end is the most upstream part of a beamline and separates the particle beam guide from the harvested radiation, insulating both vacua from one another, monitoring various beam parameters and often shielding from unwanted radiation. It is followed by the optics hutch which hosts beam-manipulating equipment: usually a monochromator

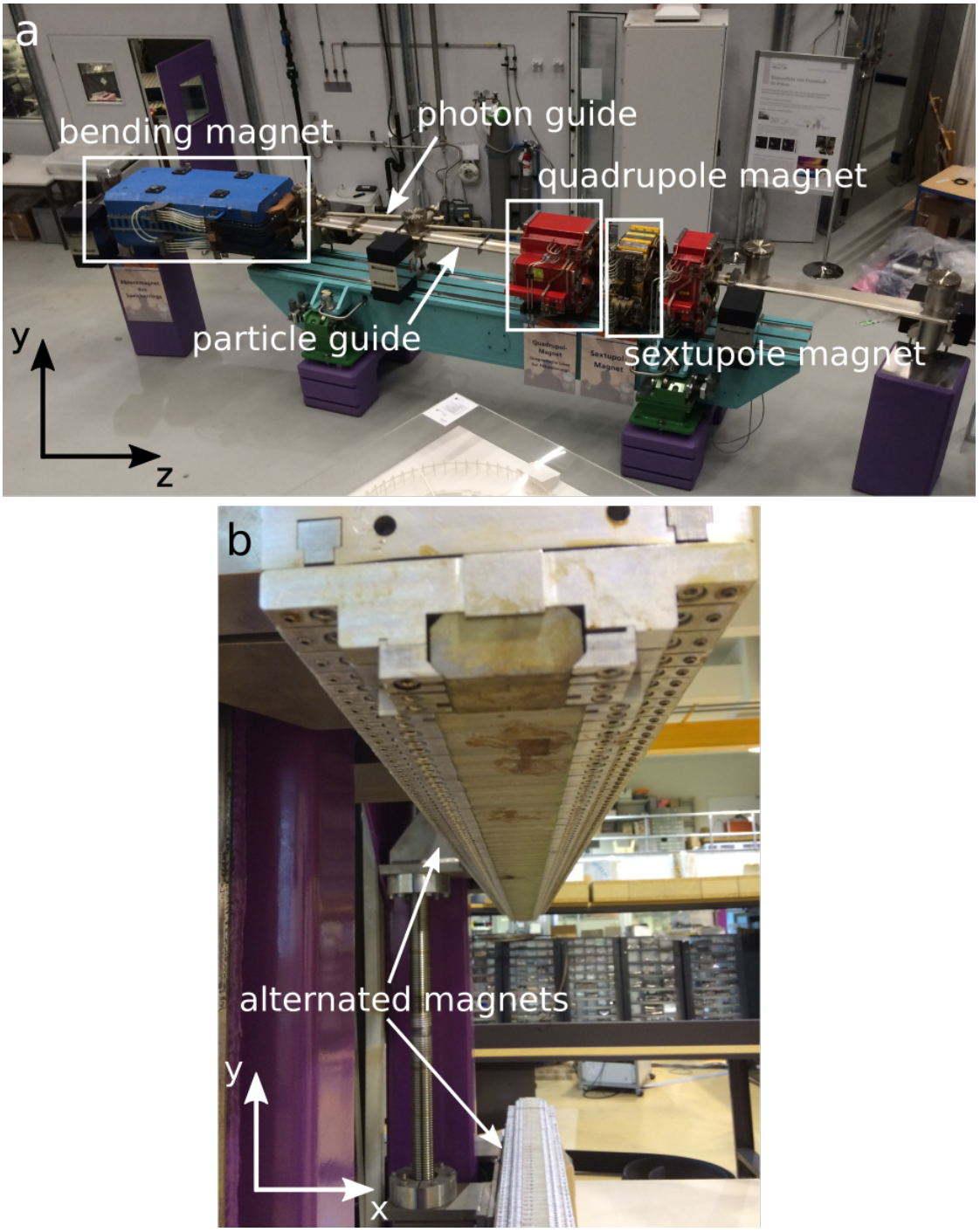

FIGURE 2.1: Photographs of components of a synchrotron source. (a) Unmounted section of storage ring featuring a bending magnet (blue), two quadrupole magnets (red) and a sextupole magnet (yellow). Particle bunches travel along z through the bending manget which bends their trajectory to keep them following the particle guide around the storage ring and at the same time emit radiation through the photon guide. Multipole magnets are used to preserve the properties of the particle beam, namely by focusing it and correcting for chromatic aberrations. (b) Unmounted undulator revealing rows of magnets in alternated N/S and S/N pairs, each pair with one pole in the top row and the other in the bottom row. The resulting alternated vertical (along y) magnetic fields cause the particle beam to oscillate horizontally (along x) and emit electromagnetic radiation. Relativistic effects cause this radiation to concentrate in a tight cone along the optical axis z.

as well as focusing KB mirrors. And finally, the experimental hutch is where actual beamline user experiments take place involving various sample environments, motors and detectors, depending on the specific requirements of each kind of experiment.

As the most advanced X-ray sources today exploit bright highly-coherent synchrotron radiation produced by having particle beams travelling through undulators, it is now useful to briefly outline their working principle. Undulators are based on the emission of electromagnetic waves by accelerated particles, much like a radio antenna, although the wavelengths emitted by undulators are much shorter than what their periodicity might suggest. The alternating magnetic fields making up an undulator are in fact typically a few cm apart but the wavelength of the emitted radiation results much shorter due to a combination of Doppler effect and Lorentz contraction.

An electron travelling through an undulator as observed from the laboratory inertial reference frame constitutes a moving source of radiation whose wavelength therefore appears shortened due to Doppler effect. When observed from an angle $\theta_L = 0$ from the optical axis, the wavelength is given by

$$\lambda_L \approx \lambda_e / 2\gamma \tag{2.31}$$

with λ_e as the wavelength in the electron reference frame and $\gamma = 1/\sqrt{1 - \frac{v^2}{c^2}} = E_e/m_e c^2$ as the Lorentz factor which here corresponds to the energy of the electron in units of rest mass energy and can be expressed as $\gamma \approx 10^3\, E_e[\mathrm{GeV}]$. This shortening of the observed wavelength which would occur also for non-relativistic particles is further stressed by the relativistic speed at which the electron typically travels in synchrotron sources, thus requiring relativistic corrections to the classical Doppler effect. Furthermore the wavelength emitted by the electron λ_e is equal to the period of the undulator λ_u as seen from the electron reference frame which also needs relativistic treatment as it undergoes Lorentz contraction and leads to

$$\lambda_e = \lambda_u / \gamma\,. \tag{2.32}$$

Combining Eq. 2.31 and Eq. 2.32 gives the general relationship

$$\lambda_L \approx \frac{\lambda_u}{2\gamma^2}\,. \tag{2.33}$$

Reintroducing a variable angle θ and considering the magnetic field B within the undulator, the general equation for the wavelength emitted by an undulator then reads

$$\lambda_L(\theta_L,\, B) \approx \frac{\lambda_u}{2\gamma^2}\left(1 + \frac{K^2}{2} + \gamma^2\theta_L^2\right) \tag{2.34}$$

with $K \propto \lambda_u\, B$ as a parameter used to characterise the undulator and usually close to unity. Eq. 2.34 implies that a possible way of varying the wavelength of the radiation

produced by an undulator is to alter the magnetic field B onto the particle beam. This is typically achieved by changing the insertion device (ID) gap, i.e. the distance between the opposite poles of the permanent magnets making up each period of the undulator. So, opening the ID gap by moving the magnetic arrays apart causes the undulator to produce radiation at a shorter wavelength and vice versa.

Furthermore the number of periods N_u of an undulator determines both its energy bandwidth and the angular spread of the emitted radiation. The bandwidth depends on $\Delta\lambda_n/\lambda_n = 1/N_u n$, with the integer n indicating the harmonic, and the full width at half maximum (FWHM) of a section of the beam perpendicular to the optical axis is given by $\theta_{\mathrm{FWHM}} \approx 1/\gamma\sqrt{N_u}$ which implies that undulators are naturally highly collimated sources. The overall divergence from an undulator is however the result of the convolution of the photon-beam divergence with that of the electron beam circulating the storage ring which is typically larger in the horizontal direction. In the case of 3rd generation sources, this results in the undulator divergence being roughly one order of magnitude larger in the horizontal direction than in the vertical which also implies different emittances $\varepsilon_x > \varepsilon_y$.

Following the spread of large-scale synchrotron facilities many efforts have been made to find ways of producing electromagnetic radiation of similar quality from smaller sources to contain both costs and space requirements and make cutting-edge X-ray experiments more accessible, even to smaller university-based laboratories rather than large dedicated research centres. Beside the liquid-metal-jet source introduced at the beginning of Section 2.2 which can be considered an improvement on previous anode-based X-ray source designs, also other designs have been proposed and developed inspired more closely by synchrotrons.

A first example is a compact light source (CLS) (Huang and Ruth, 1998) which recently became commercially available (Eggl et al., 2016) and produces hard X-rays from inverse Compton scattering. Namely relativistic electron bunches of a few tens of MeV circulating in a room-sized storage ring are made interact with infrared laser pulses in an enhancement cavity which acts similarly to an undulator hence producing bright short-wavelength radiation.

A different approach is that of laser-driven sources which exploit plasma excitations and evolved from ultra-fast high harmonic generation (HHG) concepts. One example of such design is one that produces ultra-relativistic electron bunches (up to 1 GeV) from the wakefield in a diluted plasma obtained by ionising a gas target with an intense femtosecond laser pulse (Fuchs et al., 2009). The electron bunches then go through a cm-long undulator with a period of a few millimetres thus producing soft X-ray / extreme ultraviolet (EUV) synchrotron radiation. A further development of that concept removed the undulator altogether in a design in which the focusing fields of the wakefield

itself induce electron transverse (betatron) oscillations which in turn cause the electrons to radiate X-rays with a brilliance comparable to that of 3rd generation large-scale synchrotron sources (Kneip et al., 2010). While HHG sources have been historically limited by the relatively long wavelength they produced, more recent demonstrations showed they too can reach 3rd generation-like brilliance in the EUV regime (Dromey et al., 2006). On the other hand the main limitation of laser wakefield accelerators (LWFA) has always been their low repetition rate (<Hz) which makes their use unpractical for most synchrotron science applications. Both HHG sources and LWFAs however attract great interest because of both their tabletop and ultra-fast (femtosecond) nature.

Going back to the definition of brilliance one can compare the quality of the different X-ray sources and notice that the brilliance of large-scale 3rd generation synchrotron radiation is typically 10 orders of magnitude higher than that produced by traditional laboratory sources such as rotating anodes. This explains the success of synchrotron facilities which can perform experiments which would otherwise be unfeasible but also improve on existing ones by achieving better results, e.g. faster measurements, higher precision, better resolution. For example high-brilliance sources allow to determine the structure of nanocrystals or other weakly scattering specimens via diffraction experiments whose signal-to-noise ratio would be excessively low were they performed with conventional sources. This great advantage comes at the cost of radiation damage which increases as the flux of ionising radiation impinging on a specimen grows, till the point where an increase in brilliance could adversely affect the outcome of an experiment (Henderson, 1995). This can be partly overcome by the use of cryogenic cooling (Howells et al., 2009; Holton, 2009) which is widely used for biological samples as these are particularly sensitive to radiation and accounts for the recent success of imaging techniques exploiting it, mainly cryo-electron microscopy (cryo-EM).

The issue of radiation damage can be completely bypassed thanks to the development of X-ray free-electron lasers (XFEL) which are discussed in more details in Section 2.2.2. Their peak brilliance gains another 10 orders of magnitude with respect to 3rd generation continuous synchrotron sources, reaching 10^{32} ph/s/mrad^2/mm^2/0.1%BW and thus leading to the destruction by Coulomb explosion of any specimen hit by any single radiation pulse. Nonetheless, due to the pulsed nature of XFEL sources, any of these single pulses can be short enough - typically $\lesssim$ 100 fs - to achieve diffraction before destruction (Neutze et al., 2000; Chapman et al., 2006a), i.e. the scattering events producing the measured diffraction pattern occur over a timescale which is shorter than that required by electrons to leave the specimen and causing its structure to be damaged and ultimately destroyed. Single particle imaging (SPI) or flash X-ray imaging (FXI) experiments are based on this principle exactly: the extremely high brilliance of the XFEL beam is exploited to produce a resolvable diffraction pattern of an individual

particle which is enough to reconstruct its 2D projection. By collecting and reconstructing several of such patterns it is in principle possible to retrieve the full 3D volume of the particle. The proof-of-concept of this idea has already been demonstrated for both non-biological (Loh et al., 2012; Barke et al., 2015) and biological particles (Seibert et al., 2011; Hantke et al., 2014; Van Der Schot et al., 2015; Ekeberg et al., 2015; Munke et al., 2016; Reddy et al., 2017; Hosseinizadeh et al., 2017) and, although there remain several experimental complications yet to overcome, it significantly contributed to the growing interest of the scientific community for XFELs.

2.2.2 X-ray free-electron lasers (XFELs)

3rd generation synchrotron sources make use of undulators and wigglers as insertion devices within a storage ring along with the bending magnets necessary to keep the electron bunches travelling on their bent trajectory. Therefore several bunches keep running through each device which behaves as an individual continuous X-ray source. At X-ray free-electron lasers, instead, only one longer undulator is used and every electron bunch is generated, sent through the undulator once (one-pass) and dumped right after. The injection of individual bunches leads to the characteristic femtosecond pulsed time structure mentioned earlier whilst a storage ring would barely be able to reach the subpicosecond time resolution at the expense of a great loss in peak flux, e.g. in single-bunch mode.

The large gain in flux of XFELs with respect to traditional insertion devices is mainly due to their longer undulators and higher bunch compression: in fact the higher number of periods of alternating transverse magnetic fields N_u along with the high density of the electron gas making up the particle beam enables self-amplified spontaneous emission (SASE) to occur (Margaritondo and Rebernik Ribic, 2011; Marangos, 2011; Huang and Kim, 2007). This is a process in which stochastic density variations within an electron bunch - namely electron shot noise - lead to spontaneous microbunching, i.e. the formation of periodic density modulations at the same wavelength of the emitted radiation which, once started, amplifies itself. This phenomenon is based on the interaction between the electrons and the electromagnetic waves they produce while travelling through the undulator, in a similar way to what happens in an RF cavity but at a smaller length scale. In fact the electrons move under the influence of a ponderomotive potential resulting from the combination of the undulator and the radiation fields: under such conditions and after some distance within the undulator, the energy modulation of the fields is translated into density modulations within the electron beam. The consequence is that the intensity of the radiation emitted by the electron beam grows exponentially along the undulator as the electrons within each microbunch start emitting in phase. This process continues until saturation and the total emitted radiation intensity results

greatly amplified by the quasicoherent combination of the radiation emitted by any of the N_e electrons making up the beam. For comparison, at a typical synchrotron source the total intensity of the emitted radiation from the uncorrelated electrons each generating an electric field of the same magnitude $E_n = E$ is

$$I_{\text{tot}}^{\text{uncorrelated}} \propto \sum_{n}^{N_e} \left|E_n\right|^2 = E^2 N_e \tag{2.35}$$

whilst that of the correlated electrons within the microbunches in an XFEL is

$$I_{\text{tot}}^{\text{correlated}} \propto \left|\sum_{n}^{N_e} E_n\right|^2 = E^2 N_e^2 \,. \tag{2.36}$$

At saturation both the microbunching and the intensity of the emitted radiation reach their maximum as afterwards the resonant condition is lost due to the loss of kinetic energy of the electron beam, so extending the undulator further does not lead to any gain. Nonetheless in order for saturation to be reached long undulators are required, typically several tens of meters long with $\sim 10^3$ periods. Although earlier examples of SASE FELs generating soft X-rays exist (e.g. FLASH in Hamburg, Germany), the first facility to become operational within the hard X-ray regime has been the Linac Coherent Light Source (LCLS) at SLAC National Accelerator Laboratory (previously Stanford Linear Accelerator Center) in Menlo Park, US, which opened its doors to user operation in late 2009 (Emma et al., 2010).

FELs based on such amplification principle are known as high-gain FELs and, unlike low-gain FELs, they are able to produce high intensity radiation without any optical cavity, which would be unpractical for X-rays. On the other hand SASE XFELs produce only quasicoherent radiation due to the intrinsically limited temporal coherence implicit in the SASE process. The microbunching depends on stochastic density modulations within the electron beam which are further amplified in the undulator. Therefore every electron bunch contains several distinct microbunches and every radiation pulse contains $\sim 10^2$ of phase uncorrelated fs pulses which can be represented as several coherent modes. The plot on the left-hand side of Fig. 2.2 shows the temporal distribution of such smaller pulses via the power distribution along the optical axis which clearly reveals several and distinct spikes. The number of such spikes is approximately given by the ratio between the overall length of the electron bunch and the cooperation length, i.e. the distance within the electron bunch at which self-organization occurs.

The stochastic nature of the spontaneous emission also causes similar spikes to occur within the power distribution in the spectral domain as shown in the plot on the right-hand side of Fig. 2.2. These result in a pulse bandwidth at FWHM in the range 0.2-1.0%

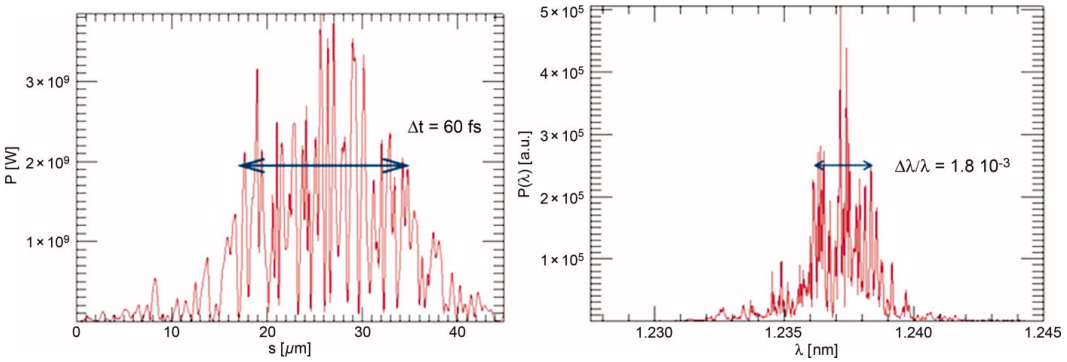

FIGURE 2.2: Simulations of temporal and spectral domain of a single pulse generated by a SASE FEL operating at 1 keV (Marangos, 2010). Permission to reproduce this figure has been granted by the Science and Technology Facilities Council (STFC).

which is significantly larger than the lowest value that could be achieved given the pulse duration.

Considering radiation pulses generated by different electron bunches, a similar stochastic variation is observed once more due to the SASE process. This implies that significant temporal and spectral variations occur also among pulses leading to shot-to-shot fluctuations of the pulsed radiation beam. For example, for SASE XFEL beams the power stability is typically of the order of 3-12% and the wavelength stability of the order of 0.1-0.2% (Emma et al., 2010)[1].

A method to reduce both pulse-to-pulse and single pulse fluctuations is to exploit a seed signal, i.e. to initiate the microbunching and amplification process with some radiation rather than leaving it occurring spontaneously from the stochastic shot noise. This approach can be applied to soft X-rays and EUV sources for which a coherent input source acting as seed can be produced, e.g. via high harmonic generation (HHG) exploiting a laser beam (Yu, 1991). On the other hand such a seed is not available for hard X-rays for whose generation a self-seeding scheme can be used instead, in which the radiation produced via the SASE process is filtered through a monochromator and then exploited as seed (Feldhaus et al., 1997; Saldin et al., 2001). In both schemes the use of a seed ensures increased stability of the pulsed beam and higher coherence of the individual radiation pulses whose temporal and spectral distributions take the form of narrow gaussian distributions. For comparison, the product of temporal duration and spectral bandwidth both taken at FWHM of a SASE pulse can be up to two orders of magnitude larger than that of a seeded pulse, highlighting the advantages that the seeded scheme offers. An example of such EUV seeded FEL is the Free Electron laser Radiation for Multidisciplinary Investigations (FERMI) facility at Elettra in Basovizza, Italy (Allaria et al., 2015).

[1]These estimates correspond to the root mean square of values collected over a few minutes of measurements at different wavelengths at the LCLS with a 30 Hz repetition rate.

Currently, seeded XFELs remain the minority due to the technical and experimental complexity of a self-seeded scheme to be compared to the SASE XFEL technology which is more established and relatively simpler. However it is clear that it is towards the former that most technological development is heading.

2.3 Scanning transmission X-ray microscopy (STXM)

As mentioned earlier, phase-contrast imaging techniques are based on the fact that light is bent when travelling through a medium by an amount related to its index of refraction. Therefore, measuring the refraction of a straight beam returns morphological information on the medium. In the case of real specimens, typically made up of several non-homogeneous media, the image obtained by measuring refraction changes constitutes a projection of the illuminated sample onto a plane perpendicular to the beam direction. Given that in the X-ray range of the electromagnetic spectrum the index of refraction (cf Eq. 2.25) of most materials typically shows values for δ much larger than β, exploiting δ-dependent refraction rather than β-dependent absorption for imaging experiments generates better contrast. Fig. 2.3 shows a comparison between β and δ for two different materials highlighting the advantage of exploiting refraction over absorption in both cases.

An application of this concept is scanning transmission X-ray microscopy (STXM) (Horowitz and Howell, 1972; Morrison and Chapman, 1983). In this technique an X-ray beam is focused to a small size and scanned onto the surface of a specimen while the transmitted signal at each scanning position is recorded by a detector downstream. Fig. 2.4 shows a typical experimental configuration suited to perform STXM scans, in which the sample is scanned in the x-y plane in order to produce a relative displacement

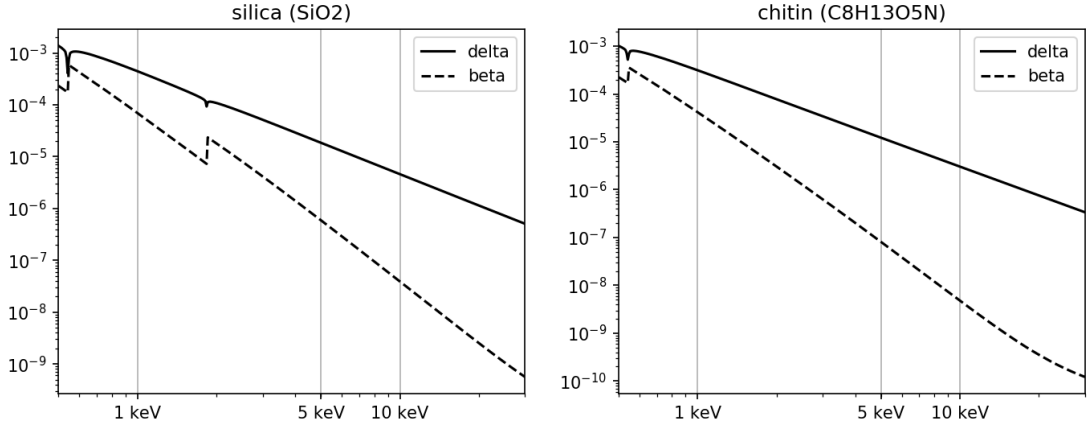

FIGURE 2.3: Comparison between δ and β values from indices of refraction of silica SiO_2 and chitin $(C_8H_{13}O_5N)_n$ within the X-ray regime. Log-log scales. Values taken from Henke et al. (1993).

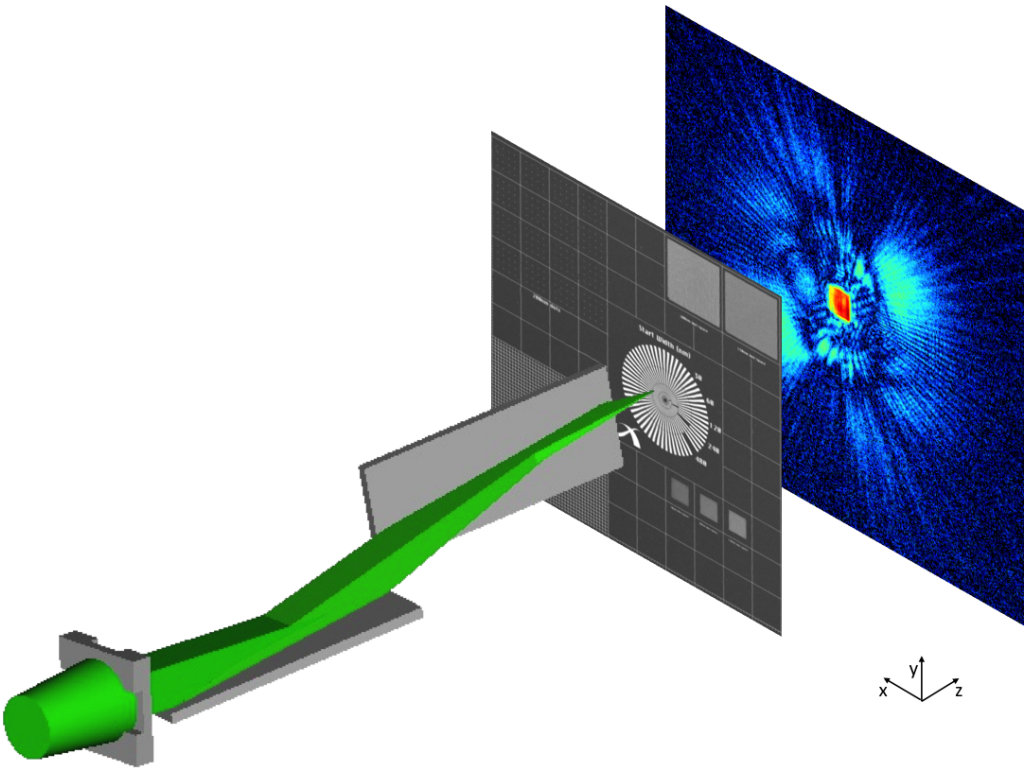

FIGURE 2.4: Diagram of an experimental setup suited for scanning X-ray microscopy experiments: with this geometry both scanning transmission X-ray microscopy (STXM) and ptychography experiments can be performed. Some adjustable slits act as secondary source by shaping the X-ray beam (represented in green) coming from the source upstream. A pair of KB mirrors focuses the beam onto a small area of a sample. The size of the illuminating focused beam onto the sample – i.e. the probe size – is adjusted by translating the sample along the optical axis z. The beam is scanned onto the sample by translating the sample in the x-y plane. The free-space propagated exit waves (i.e. the diffraction patterns) are recorded by a detector downstream. The main difference between the data acquisition processes of STXM and ptychography is that the latter requires some degree of overlap between adjacent scanning positions (cf Section 2.4).

between probe and object. Beside KB mirrors, also other kinds of focusing optics are often used for scanning X-ray microscopy experiments, such as FZPs and CRLs (cf Section 2.1.3).

Regardless of the choice of detecting system, a first imaging mode STXM provides is absorption-contrast. Rather intuitively, this is based on recording the beam attenuation at every scanning position for which a simple integration of every collected frame is sufficient, effectively reducing any detector to a point detector. Another imaging mode is that of phase-contrast and is based on the use of a segmented or pixelated detector. Determining the centre of mass of every diffraction pattern in fact is equivalent to determining the angle of refraction α of the X-ray beam at every scanning position, given the detector's pixel size and its distance from the sample. In the conventional

reference system in which the optical axis corresponds to the axis z, the relationships

$$\frac{\partial\varphi(x,y)}{\partial x} = k\alpha_x\,,\ \frac{\partial\varphi(x,y)}{\partial y} = k\alpha_y \tag{2.37}$$

hold, with the wavevector $k = 2\pi/\lambda$, the phase φ and the horizontal and vertical refraction angles α_x and α_y respectively. This implies that measuring the refraction angle α allows to produce a pair of differential phase contrast images – horizontal and vertical – which through integration lead to a phase image. Even just the differential phase-contrast images are especially useful in returning information on the specific orientation of interfaces within the specimen and often reveals features unnoticeable from the absorption signal alone. Furthermore, by integrating only the signal outside the direct beam, also a dark field image of the specimen can be obtained, which results in a third imaging mode accessible via STXM. Dark field images are sensitive to scattering which causes a change in the amplitude of interference patterns.

The resolution STXM images achieve is dictated by the probe size used to perform the scanning measurements. It follows that in most instances in which STXM has been implemented at X-ray imaging beamlines there has been a significant push to reduce the smallest achievable spot size produced by beamline optics (Chapman et al., 1995; Gianoncelli et al., 2006; Stampanoni et al., 2010; Kaulich et al., 2011). In fact focusing optics constitutes the main limiting factor in terms of achievable resolving power for this technique and the smallest focal spot sizes achieved to date have been able to generate images with resolution in the 10 nm range (Mohacsi et al., 2017).

STXM can also be combined with simultaneous X-ray fluorescence (XRF) measurements which enrich the collected dataset with chemical information and elemental contrast. Also X-ray absorption spectroscopy (XAS) is compatible with the STXM geometry although it is typically performed using a point detector which prevents the collection of differential phase contrast and dark field images.

Other techniques exist which are able to achieve phase-contrast imaging but they fall outside the scope of this work. Some of these are analyser-based and grating-based imaging which are increasingly widespread even for macroscopic applications such as medical imaging at hospitals and in general also outside high-brilliance X-ray facilities. For a wide overview of some of them the reader is referred to David et al. (2002), Momose (2005) and Weitkamp et al. (2005).

2.4 Ptychography

First X-ray microscopy techniques relied on geometries analogous to those used for visible light microscopy which very roughly consist of a source, some optics to focus light onto

the sample under study, an objective and a detector. For example such a geometry is employed in full-field transmission X-ray microscopy (TXM) where the main factor limiting resolution is the objective lens. As the index of refraction of X-rays varies only slightly from unity, the manufacture of X-ray optics components is particularly challenging and often results in aberrations occurring and leads to low efficiency or low numerical apertures, all features compromising the performance of a microscopy setup. The role of the objective lens in such setups is to invert the free-space propagated image of the sample back to a real space image which is then recorded by the detector. Lensless microscopy approaches exist which bypass the need for an objective lens. In such experiments the light from the sample is directly recorded by the detector without the use of image-forming optics. An image of the sample is later obtained via back-propagation after the lost phase information has been recovered using phase retrieval algorithms Therefore, ptychography falls into the category of lensless imaging techniques and allows to computationally recover complex-valued images by iteratively solving the phase problem and, in principle, achieve diffraction-limited resolution.

It should be pointed out that the iterative phase retrieval algorithms employed in ptychography hold regardless of the radiation used. In fact, ptychographic reconstruction is successfully achieved within experiments exploiting either one of X-rays, visible light or electrons. The wide reach of ptychography is demonstrated by its continued development with visible light (Sun et al., 2017) as well as its recent success in achieving sub-Ångström (< 0.5 Å$= 0.05$ nm) resolution within electron microscopy experiments (Jiang et al., 2018). However, this work focuses on X-ray ptychography, so its application to fields other than X-ray science falls outside its scope.

The experimental geometry used for X-ray ptychography is the same as that already represented for STXM (cf Fig. 2.4). The main difference with respect to STXM is ptychography's need for overlap between adjacent illuminated areas, as discussed below.

Ptychography's background and its developments are presented in this section. The reader can refer to Rodenburg (2008) for a wide review of the field of ptychography and to Pfeiffer (2018) for a review of the recent advances of X-ray ptychography.

2.4.1 Iterative phase-retrieval algorithms

The first formulation of the concept of phase retrieval algorithm for imaging (Gerchberg and Saxton, 1972) was followed by the development of iterative phase retrieval algorithms (Fienup, 1978; Bruck and Sodin, 1979), later applied to X-ray diffraction imaging. These algorithms can solve the phase problem provided what was known as oversampling is achieved during the experimental data collection. This translates into producing a constrained problem, as detailed further below.

In order to understand the concept of oversampling for phase retrieval, one could start considering a one-dimensional signal that can be decomposed and analysed using a discrete Fourier transform which translates the signal into the frequency domain. Such domain is often labelled as inverse space, Fourier space or reciprocal space as opposed to the domain of the signal prior Fourier transformation which is in turn identified as direct space or real space. The Nyquist frequency q_N then represents the highest frequency from the discrete Fourier transform of such a direct space signal with sampling interval Δx and it reads

$$q_N = N\frac{\Delta q}{2} = \frac{\pi}{\Delta x} \tag{2.38}$$

with Δq as the sampling interval in inverse space.

In signal processing the bandlimit ought to be smaller than the Nyquist frequency in order for aliasing not to occur and thus oversampling to be achieved.

The concept of 1D bandlimit still holds for the 2D case thus allowing for 2D signals such as electromagnetic wavefronts to be sampled finely enough to avoid aliasing. In actual experiments though, only the real part of any complex signal can be detected (cf phase problem from Section 2.1.3) which is equivalent to measuring half of the information carried by a given wavefront thus making its recovery an underdetermined problem. The Nyquist-Shannon sampling theorem (Shannon, 1949; Sayre, 1952) offers a solution to this by stating that it is in principle sufficient to oversample a wavefront by a further factor of two in order to obtain at least as many constraints as unknowns. In direct space this can be achieved through the use of a support – namely an isolated specimen – outside of which no signal is assumed to be produced. The theorem reads

$$\Delta q_x \leq \frac{\pi}{s_x},\ \Delta q_y \leq \frac{\pi}{s_y} \tag{2.39}$$

where s_x and s_y describe the extension of the support respectively along the x and y directions.

From Nyquist-Shannon sampling theorem it follows that by selecting a support small enough in order to satisfy oversampling conditions, phase retrieval can take place. This occurs via iterative phase retrieval algorithms the most widespread of which are projection-based algorithms such as the difference map (DM) algorithm (Elser, 2003). Projection-based algorithms are search algorithms that aim at finding the intercept of constraint sets by applying alternately projections onto such sets. In the case of phase retrieval the constraints are two, one in real space and one in inverse space. They are used to find the complex-valued exit wave which, as mentioned in Section 2.1.3, is the product of probe P and object O, i.e. the wavefront illuminating the sample and the

transmission function of the sample respectively, such that

$$\psi(x,y) = \psi(\mathbf{r}) = P(\mathbf{r})O(\mathbf{r})\,. \tag{2.40}$$

At the n-th iteration, a Fourier magnitude projection is applied to the latest estimate of the exit wave $\psi_n(\mathbf{r})$. In the most general case, such projection onto the constraints in inverse space reads

$$\Pi_F\{\psi_n\} = \mathcal{F}^{-1}\left(\sqrt{I(\mathbf{q})}\frac{\mathcal{F}\psi_n(\mathbf{r})}{|\mathcal{F}\psi_n(\mathbf{r})|}\right)\,. \tag{2.41}$$

This is equivalent to replacing the magnitudes of the current estimate of the exit wave with the experimentally measured ones, i.e. $\sqrt{I(\mathbf{q})}$, which geometrically corresponds to projecting each estimate onto a circle in the complex plane.

On the other hand, the real space constraint is the support constraint that forces the estimated exit wave to zero outside the support S of the isolated sample and it reads

$$\Pi_S\{\psi_n(\mathbf{r})\} = \begin{cases} \psi_n(\mathbf{r}) & \mathbf{r}\in S \\ 0 & \mathbf{r}\notin S \end{cases}\,. \tag{2.42}$$

Different or more elaborate inverse and real space constraints can be applied which depend on the experimental conditions as it is briefly discussed later.

Applying both projections, the update rule for DM phase retrieval algorithms takes the general form

$$\psi_{n+1} = \psi_n + \beta\big[\Pi_F\big\{(1+\gamma_1)\Pi_S\{\psi_n\} - \gamma_1\psi_n\big\} - \Pi_S\big\{(1+\gamma_2)\Pi_F\{\psi_n\} - \gamma_2\psi_n\big\}\big] \tag{2.43}$$

where β, γ_1 and γ_2 are complex parameters.

Many variants of such general form exist. The hybrid input-output (HIO) algorithm (Fienup, 1978, 1982) for example is a widespread error reduction algorithm whose update rule takes the form

$$\psi_{n+1} = \psi_n + \beta\big[\Pi_F\big\{(1+\beta^{-1})\Pi_S\{\psi_n\} - \beta^{-1}\psi_n\big\} - \Pi_S\{\psi_n\}\big] \tag{2.44}$$

which can easily be identified as a special case of the generic DM algorithm.

The application of such iterative phase retrieval algorithms has been successfully tested on isolated samples within coherent diffraction imaging (CDI) experiments (Miao et al., 1999), so named because of the highly coherent radiation needed to produce phasable diffraction patterns. This approach is also rather promising for single particle imaging and flash X-ray imaging studies in which the aim is to retrieve the full 3D structure of an isolated specimen of which several 2D projections have been collected at random

orientations (Chapman et al., 2006b). This is particularly relevant for those submicron particles whose structure could not otherwise easily be resolved for example due to the lack of a stable crystalline form of such particles which prevents the more common crystallographic approach from being applicable. This is the case of several structures of biological interest and has been one of the scientific drivers for the investment into XFEL facilities which are needed to perform such high-brilliance experiments as mentioned earlier (Neutze et al., 2000).

On the other hand, most specimens are typically extended in nature or need to be imaged in specific environments which prevent them from being isolated. Two kinds of approach have been developed which are able to tackle this issue exploiting a confined illumination acting as support: they are keyhole coherent diffractive imaging and ptychography. While keyhole CDI is a further development of previous CDI techniques and has been experimentally demonstrated on extended samples (Abbey et al., 2008), ptychography originated from the field of electron microscopy for which – as for X-rays – phase retrieval is also achievable (Hoppe, 1969). The name and concept of ptychography was first theorised as a non-iterative method by Hegerl and Hoppe (1970) and later developed (Bates and Rodenburg, 1989; Rodenburg and Bates, 1992) and experimentally demonstrated (Rodenburg et al., 1993) for electron microscopy. Similar phase retrieval approaches were also demonstrated for X-rays (Chapman, 1996, 1997) in what can be seen as a combination of CDI and STXM able to retrieve phase images within an extended scanning area exploiting a confined illumination as a support. Projection-based iterative phase retrieval algorithms were then introduced which exploited the idea of alternating projections within real and inverse space (Faulkner and Rodenburg, 2004; Rodenburg and Faulkner, 2004; Rodenburg et al., 2007) in order to retrieve the full extended-object transmission function. In ptychography in general, an X-ray beam is scanned through an extended sample recording intensity distributions at several positions of the probe with respect to the object. The constraints needed to ensure that the phase retrieval problem is not ill-posed rely on the overlap between adjacent illuminated areas of the sample. The data redundancy so-achieved has been proven strong enough not only for iterative algorithms to converge to a solution for the object but also to achieve simultaneous probe and object reconstruction without *a priori* knowledge on either one of them (Thibault et al., 2008, 2009; Maiden and Rodenburg, 2009) thus bypassing the main limitation of the previous algorithms which did not update the initial estimate of the illumination function.

The method from Thibault et al. (2008) is based on a DM algorithm. In this case the exit wave $\psi(\mathbf{r})$ is replaced by the state vector

$$\Psi = \big(\psi_1(\mathbf{r}), \psi_2(\mathbf{r}), \ldots, \psi_N(\mathbf{r})\big) \tag{2.45}$$

which contains all the N views of the probe onto the object. The Fourier magnitude (or modulus) projection is then individually applied to each view $\psi_j(\mathbf{r})$ but remains otherwise unchanged in nature. For ptychography the recorded intensities then read

$$I_j(\mathbf{q}) = \left|\mathcal{F}\psi_j(\mathbf{r})\right|^2 = \left|\mathcal{F}\left[P_j(\mathbf{r})O_j(\mathbf{r}-\mathbf{r}_j)\right]\right|^2 \tag{2.46}$$

where $\mathbf{r}_j = (x_j, y_j)$ represents the relative displacement of the object with respect to the probe for the j-th view. On the other hand the real space constraint is no longer the support of an isolated sample, but rather an overlap constraint among adjacent probe-shaped illuminated areas of the extended object. Therefore the projection Π_S is replaced by $\Pi_O\{\Psi\}$ which is then applied to every view such that

$$\Pi_O\left\{\psi_j(\mathbf{r})\right\} = \hat{P}(\mathbf{r})\hat{O}(\mathbf{r}-\mathbf{r}_j) \tag{2.47}$$

where $\hat{P}$ and $\hat{O}$ are chosen so as to minimise the difference

$$\left|\left|\Psi - \Psi^O\right|\right|^2 = \sum_j \sum_{\mathbf{r}} \left|\psi_j(\mathbf{r}) - \hat{P}(\mathbf{r})\hat{O}(\mathbf{r}-\mathbf{r}_j)\right|^2 . \tag{2.48}$$

Such minimisation can be achieved through differentiation with respect to $\hat{P}$ and $\hat{O}$ thus giving the system of equations

$$\hat{O}(\mathbf{r}) = \frac{\sum_j \hat{P}^*(\mathbf{r}+\mathbf{r}_j)\psi_j(\mathbf{r}+\mathbf{r}_j)}{\sum_j \left|\hat{P}(\mathbf{r}+\mathbf{r}_j)\right|^2} \tag{2.49}$$

$$\hat{P}(\mathbf{r}) = \frac{\sum_j \hat{O}^*(\mathbf{r}-\mathbf{r}_j)\psi_j(\mathbf{r})}{\sum_j \left|\hat{O}(\mathbf{r}-\mathbf{r}_j)\right|^2} . \tag{2.50}$$

Alternately applying these equations leads to the minimisation of Eq. 2.48. The complete formulation of the update rule for the DM algorithm for ptychography then takes a form similar to Eq. 2.44. In fact by choosing $\beta = 1$ one gets

$$\Psi_{n+1} = \Psi_n + \Pi_F\{2\Pi_O\{\Psi_n\} - \Psi_n\} - \Pi_O\{\Psi_n\} . \tag{2.51}$$

Another kind of projection-based iterative phase retrieval algorithm, which does not heavily rely on an in-depth knowledge of the probe and is currently widespread throughout the X-ray imaging community, is the extended ptychographical iterative engine (ePIE) (Maiden and Rodenburg, 2009). This is a more versatile and flexible version of the simpler ptychographical iterative engine (PIE) which marked the beginning of modern ptychography (Rodenburg and Faulkner, 2004).

A conceptually different approach is used by another ptychographic iterative phase retrieval algorithm known as maximum likelihood (ML) algorithm.

Likelihood maximisation has been successfully implemented (Thibault and Guizar-Sicairos, 2012) and is particularly suited for dealing with noise which is an intrinsic aspect of any experiment involving photons and hence at least statistical noise. In fact in an ideal case the only source of noise is the statistical noise witnessed by detectors. Once the recorded frames have been converted into photon counts – a step which is not necessary in the case of photon-counting detectors – it should still be taken into account the fact that such discrete photon distribution is the result of a quantum process which obeys Poisson statistics. The approach developed within maximum likelihood is based on the modelling of the probability p of measuring $n(\mathbf{q})$ photons out of a probe-object interaction which reads

$$p^P\big(n_j(\mathbf{q})\big|P(\mathbf{r})O(\mathbf{r})\big) = \frac{I_j(\mathbf{q})^{n_j(\mathbf{q})}}{n_j(\mathbf{q})!}e^{-I_j(\mathbf{q})} \tag{2.52}$$

where $I_j(\mathbf{q})$ is always given by Eq. 2.46.

Nonetheless, more often other sources of noise such as detector point spread function (PSF) are simultaneously present in the experiment and a Gaussian distribution becomes a more suited representation of the probability distribution. This is in general a valid approximation in the case of high values of the intensity $I_j(\mathbf{q})$ and reads

$$p^G\big(n_j(\mathbf{q})\big|P(\mathbf{r})O(\mathbf{r})\big) = \frac{1}{\sqrt{2\pi\sigma_j^2(\mathbf{q})}}e^{-[I_j(\mathbf{q})-n_j(\mathbf{q})]^2/2\sigma_j^2(\mathbf{q})}\,. \tag{2.53}$$

Following the Gaussian probability distribution p^G the negative log-likelihood is then defined as

$$\mathcal{L} = -\log\prod_j\prod_{\mathbf{q}} p^G\big(n_j(\mathbf{q})\big|P(\mathbf{r})O(\mathbf{r})\big) = \sum_j\sum_{\mathbf{q}} w_j(\mathbf{q})\frac{\big(I_j(\mathbf{q})-n_j(\mathbf{q})\big)^2}{2\sigma_j^2(\mathbf{q})} \tag{2.54}$$

which takes the form of a weighted sum of least squares with the weights $w_j(\mathbf{q})$ introduced to mask out invalid measurements such as dead or bad pixels. The minimisation of $\mathcal{L}$ with respect to $P(\mathbf{r})$ and $O(\mathbf{r})$ then returns the most likely estimates of the probe and the object given the measured photon counts $n_j(\mathbf{q})$. For such minimisation Wirtinger derivatives of $\mathcal{L}$ are used, which read

$$\frac{\partial\mathcal{L}}{\partial O(\mathbf{r})} = \sum_j P(\mathbf{r}+\mathbf{r}_j)\chi_j^*(\mathbf{r}+\mathbf{r}_j) \tag{2.55}$$

$$\frac{\partial\mathcal{L}}{\partial P(\mathbf{r})} = \sum_j O(\mathbf{r}-\mathbf{r}_j)\chi_j^*(\mathbf{r}) \tag{2.56}$$

where $\chi_j(\mathbf{r})$ can be defined in inverse space as

$$\tilde{\chi}_j(\mathbf{q}) = \frac{\partial \mathcal{L}}{\partial I_j(\mathbf{q})}\tilde{\psi}_j(\mathbf{q}) = w_j(\mathbf{q})\frac{I_j(\mathbf{q}) - n_j(\mathbf{q})}{\sigma_j^2(\mathbf{q})}\tilde{\psi}_j(\mathbf{q})\,. \tag{2.57}$$

The so-defined ML algorithm is found to be most useful for the refinement of results estimated by other search algorithms, usually more efficient in sampling wide search spaces. In such applications it often leads to an improvement in the achievable resolution.

2.4.2 Mixed-states ptychography

So far it has implicitly been assumed that the probe interacting with the sample has a well-defined phase or, in other words, it is fully coherent. As seen in Section 2.1.2, a high degree of coherence is required to produce resolvable interference effects. It is on these that X-ray diffraction imaging techniques are based, to the point that some of them are referred to as coherent diffraction imaging (CDI) techniques in order to stress the need for highly coherent radiation. However, it has been shown that partial coherence can be handled effectively by phase retrieval algorithms in both the cases of limited transverse (Whitehead et al., 2009; Clark and Peele, 2011) and longitudinal (Abbey et al., 2011) coherence. Furthermore ptychography can converge to meaningful solutions whilst dealing with a wide variety of sources of decoherence and – as stated earlier – without any modelling or *a priori* knowledge on either one of probe and object (Thibault and Menzel, 2013). This is achieved by interpreting a partially coherent probe as an ensemble of mixed quantum states represented by a low-rank density matrix. The rank r of such a density matrix ρ corresponds to the number of orthogonal states in which ρ can be spectrally decomposed. It comes from this that a density matrix of rank $r = 0$ describes a probe in a pure state, i.e. a fully coherent probe, and is defined as $\rho = |P\rangle\langle P|$, whilst for higher ranks $r > 0$ it becomes

$$\rho = \sum_k^r |P_k\rangle\langle P_k|\,. \tag{2.58}$$

The ptychographic problem from Eq. 2.46 can be rewritten representing the object as an operator onto the probe $\hat{O}_j = O(\mathbf{r} - \mathbf{r}_j)$ which for a pure state probe ($r = 0$) reads

$$I_j(\mathbf{q}) = \left|\mathcal{F}\psi_j\right|^2 = \left|\langle \mathbf{q}|O_j|P\rangle\right|^2. \tag{2.59}$$

The generalisation of Eq. 2.59 for a mixed-state probe then reads

$$I_j(\mathbf{q}) = \sum_k \left|\langle \mathbf{q}|O_j|P_k\rangle\right|^2. \tag{2.60}$$

This representation has been demonstrated to be able to handle not only partially coherent probes, but even other sources of decoherence such as the point spread function of detectors as well as sample vibrations. Furthermore, this approach can be extended to mixed-state objects too which in turn enables studies on sample dynamics to be conducted under conditions which can range from stochastic equilibrium fluctuations to steady flows, periodic variations and continuous sample movement. The latter is particularly interesting in the context of on-the-fly scans aimed at increasing the experimental acquisition rate. For a mixed-state object Eq. 2.60 then is parametrised as

$$I_j(\mathbf{q}) = \sum_{k,l} \left| \langle \mathbf{q} | O_{j,l} | P_k \rangle \right|^2 . \tag{2.61}$$

This formalism can be implemented in the difference map (DM) algorithm mentioned earlier. In this case the Fourier magnitude constraint (Eq 2.41) becomes

$$\Pi_F\{\psi_{j,k,l}\} = \mathcal{F}^{-1}\left[\sqrt{I_j(\mathbf{q})}\frac{\mathcal{F}\psi_{j,k,l}(\mathbf{r})}{\sqrt{\sum_{k,l}\left|\mathcal{F}\psi_{j,k,l}(\mathbf{r})\right|^2}}\right] \tag{2.62}$$

which is equivalent to projecting each point into the complex space onto a multidimensional quadric form of a circle. This leads to the reformulation of Eq.s 2.49-2.50 into

$$\hat{O}_l(\mathbf{r}) = \frac{\sum_k \sum_j \hat{P}_k^*(\mathbf{r}+\mathbf{r}_j)\psi_{j,k,l}(\mathbf{r}+\mathbf{r}_j)}{\sum_k \sum_j \left|\hat{P}_k(\mathbf{r}+\mathbf{r}_j)\right|^2} \tag{2.63}$$

$$\hat{P}_k(\mathbf{r}) = \frac{\sum_l \sum_j \hat{O}_l^*(\mathbf{r}-\mathbf{r}_j)\psi_{j,k,l}(\mathbf{r})}{\sum_l \sum_j \left|\hat{O}_l(\mathbf{r}-\mathbf{r}_j)\right|^2} . \tag{2.64}$$

Furthermore, one can reformulate the maximum likelihood (ML) algorithm for the mixed-state conditions too, obtaining the derivatives of the negative log-likelihood in a form similar to Eq.s 2.55-2.56:

$$\frac{\partial \mathcal{L}}{\partial O_l(\mathbf{r})} = \sum_{j,k} P_k(\mathbf{r}+\mathbf{r}_j)\frac{\partial \mathcal{L}}{\partial \psi^*_{j,k,l}(\mathbf{r}+\mathbf{r}_j)} \tag{2.65}$$

$$\frac{\partial \mathcal{L}}{\partial P_k(\mathbf{r})} = \sum_{j,l} O_l(\mathbf{r}-\mathbf{r}_j)\frac{\partial \mathcal{L}}{\partial \psi^*_{j,k,l}(\mathbf{r})} . \tag{2.66}$$

This system of equations is exploited by the minimisation algorithm which usually applies several line minimisations in order to find a solution.

Both DM and ML algorithms are routinely employed in ptychographic reconstructions with multimodal decomposition which offer the great advantage of relaxing the requirements on the experimental setup, mainly in terms of stability and coherence.

2.4.3 Near-field ptychography

So far the application of ptychography has been presented only within the far-field propagation regime, i.e. exploiting Fraunhofer diffraction. However soon after its first development, ptychography has been successfully implemented also for near-field (NF) experiments, i.e. exploiting Fresnel diffraction (Stockmar et al., 2013). The same iterative phase-retrieval algorithms as for far-field still hold with the fundamental difference of the operator applied in between iterations which for near-field ptychography (NFP) becomes the Fresnel propagator introduced in Section 2.1.1. In fact measuring diffraction in the near-field regime leads to recording holograms, namely real-space images featuring Fresnel fringes and magnified by the use of a divergent-beam geometry.

NFP stemmed from the concept of X-ray inline holography proposed long ago by Gabor (1948) and belongs to the wider field of propagation-based imaging exploiting Fresnel diffraction. Like other near-field imaging techniques it benefits from a small detector pixel size which is a key factor affecting the achievable resolution of reconstructed images. On the other hand there are less stringent requirements for the detector dynamic range as compared to the far-field case and it can also be exploited in the presence of low beam coherence.

Although this varies from experiment to experiment mainly depending on their geometry, NFP is generally found to be faster and able to return larger images with respect to far-field ptychography (FFP) mainly on account of the former making use of a larger illumination positively affecting the scanned area per unit time. On the other hand NFP usually achieves lower resolutions than FFP leaving – at least at the time of writing – the latter as the preferred technique for experiments aiming at the highest resolution. However NFP proved able to reconstruct complex-valued transmission functions even of thick specimens (Stockmar et al., 2015b) and remains the ptychographic variant of choice at some high-resolution imaging beamlines (da Silva et al., 2017a).

Some experimental applications of near-field ptychography are discussed in Chapters 3,5.

2.4.4 Post-processing

Both near-field and far-field ptychography return projections of the complex-valued transmission function of an area scanned by the beam. These are usually represented separately as absorption and phase images. Despite their lower contrast, absorption images are rather straight-forward to interpret as they stem from the transmission properties of specimens as dictated by the imaginary part β of their index of refraction (cf Section 2.1.3). On the other hand the phase images reconstructed by ptychographic algorithms need to undergo some further post-processing procedure before being used

to visualise the phase-shifting properties of specimens described by the real part δ of the index of refraction. Being based on a multiplicative relation between probe and object, reconstruction algorithms return objects $O_{\mathrm{r}}(x, y)$ multiplied by unknown phase terms. This reads

$$O_{\mathrm{r}}(x, y) = O(x, y)e^{i(a+bx+cy)} \tag{2.67}$$

where $O(x, y)$ is the same as Eq. 2.28 and a, b and c are constants. Linear phase terms b and c generate a linear phase ramp equivalent to an object translation in Fourier space. In most situations this can be easily corrected by subtracting from the phase a linear phase ramp obtained exploiting regions of the imaged area of known phase-shifting properties. Whenever possible, this is achieved exploiting regions outside the sample which can be assumed to produce negligible phase shifts, typically air or empty space in the case of experiments with hard or soft X-rays respectively. At the same time this allows to correct for the constant offset making the result quantitative in nature.

Another post-processing operation necessary for the meaningful representation of the phase part of most reconstructions is phase unwrapping. Whenever the range of phase shift exceeds 2π in fact this leads to discontinuities resulting of wrapping of the phase values within the range $(0,\ 2\pi)$ which then needs to be unwrapped in order to obtain physically meaningful values.

Some phase ramp removal and phase unwrapping procedures are briefly treated in Guizar-Sicairos et al. (2011) and are now standard steps of any ptychographic image reconstruction.

2.4.5 Further advances

X-ray ptychography quickly developed within the last decade, i.e. as soon as robust iterative reconstruction algorithms became available. Since then its reach kept expanding both in terms of quality of the images it produces and its range of applicability. It has been demonstrated X-ray ptychography is able to reliably resolve structures with a size of 10 nm or smaller both in the hard (Schropp et al., 2012) and in the soft X-ray regime (Shapiro et al., 2014).

As for STXM, also ptychography has been successfully combined with other X-ray investigation techniques such as X-ray fluorescence (XRF) (Vine et al., 2012; Deng et al., 2015b) and different forms of X-ray absorption spectroscopy (XAS) (Beckers et al., 2011; Maiden et al., 2013; Shapiro et al., 2014) producing phase-contrast morphological images complemented with chemical information.

Also reconstruction algorithms saw steady development enabling ptychography to be applied in a variety of experimental situations. As mentioned already, algorithms exist

which are able to deal with partial coherence (Thibault and Menzel, 2013). Others can correct for inaccuracies or uncertainties in motor positions associated to each frame of a ptychographic scan through different position refinement approaches (Guizar-Sicairos and Fienup, 2008; Maiden et al., 2012b; Beckers et al., 2013; Zhang et al., 2013; Tripathi et al., 2014). Continuous on-the-fly scanning mode is another desirable feature of many imaging experiments positively affecting time-efficiency and also in the case of ptychography reconstruction algorithms able to handle it have been implemented (Pelz et al., 2014; Clark et al., 2014; Deng et al., 2015a).

Finally the case of specimens perturbing the illumination enough to significantly break the projection approximation has also been considered, i.e. that of probe-object interactions for which the transverse Laplacian

$$\nabla_{\perp}^{2} = \frac{\partial^2}{\partial x^2} + \frac{\partial^2}{\partial y^2} \tag{2.68}$$

from Helmholtz equation (Eq. 2.8) is no longer negligible. To tackle this issue reconstruction algorithms have been designed which model the sample as a stack of multiple layers or slices and hence are commonly identified as 'multi-slice' approaches (Maiden et al., 2012a; Suzuki et al., 2014; Tsai et al., 2016).

2.5 Tomography

Another fundamental application of X-rays is X-ray tomography, a technique commonly used to retrieve volumetric information starting from 2D projections thanks to the relatively large penetration depth of X-rays for most materials. In the context of medical imaging in particular, this technique is also widely known as computed axial tomography (CAT or CT) due to its use of computerised algorithms for the retrieval of volumes. One of the most widespread approaches for volume retrieval is based on the filtered back-projection (FBP) of a collection of projection images recorded at different sample orientations. It relies on inverse Radon transforms and returns bulk 3D reconstructions of the imaged samples. The achievable 3D resolution depends both on the resolution obtained in the 2D projections and on the total number of projections. Measuring over an angular range of sample orientations of π requires at least $N_{\mathrm{proj}} \approx \frac{\pi}{2} N_{\mathrm{pix}}$ projections in order for the Fourier space to be sampled enough for the tomographic reconstruction not to produce major artefacts, with N_{pix} as the detector size in pixel units, i.e. the total number of pixels in one dimension. This is also known as the Crowther criterion (Crowther et al., 1970).

Tomography was first used for absorption imaging, but it only requires several 2D projections in order to reconstruct a 3D image, leaving more freedom on how these 2D

projections are produced. Therefore, the tomographic approach is accessible for the whole range of 2D imaging techniques and is routinely and successfully applied with X-ray phase-contrast and diffraction microscopy techniques, further highlighting the great benefits of X-rays in the investigation of bulk materials.

In fact, both electron microscopy (EM) and visible light microscopy are less suited to efficiently image through 3D specimens as both electrons and visible light photons typically show low penetration depth for most condensed matter and therefore are only able to sample the surface of materials, or the bulk of relatively thin specimens.

As for other phase-contrast microscopy techniques, also ptychography has been successfully combined with tomography ensuring bulk 3D reconstructions of specimens both in the far-field (Dierolf et al., 2010; Guizar-Sicairos et al., 2011; Diaz et al., 2012) and in the near-field (Stockmar et al., 2015a). This approach is also known as ptychographic X-ray computed tomography (PXCT). It can be used to achieve local quantitative tomographic reconstructions of volumes (Guizar-Sicairos et al., 2015a) and can be combined with other imaging techniques compatible with tomographic experiments. It has also been demonstrated it can retrieve high-resolution volume reconstructions with voxel sizes as small as 16 nm (Holler et al., 2014).

Chapter 3

Multiple-technique experimental protocol for X-ray imaging end stations

In Chapter 2 several techniques have been presented which are able to produce images of a specimen exploiting X-rays in different geometries. They all have different requirements and typically offer trade-offs between acquisition rate and field-of-view (FOV) on the one hand and achievable resolution on the other.

In this chapter, an imaging protocol is presented where some of these techniques have been implemented and combined during X-ray imaging experiments performed at the Diamond Light Source (DLS)'s hard X-rays Coherence Branchline I13-1 (Rau et al., 2011) with the aim of obtaining an adaptive coherent multiscale imaging setup, suited for exploring a wide range of length scales. Both the imaging protocol and some results obtained exploiting it are discussed. The imaging techniques used within the protocol are a form of full-field microscopy, scanning transmission X-ray microscopy and both near-field and far-field ptychography, which all fall into the category of propagation-based scanning X-ray microscopy techniques. For all of them, the X-ray beam is scanned onto the sample by translating the latter onto a plane perpendicular to the optical axis and, in the case of ptychographic scans, ensuring sufficient illumination overlap among adjacent scanning positions. At each position the free-space propagated exit wave produced by the probe-object interaction is recorded by a detector located downstream to the sample along the optical axis, thus bypassing the need for an image-forming lens.

The material presented in this chapter is largely drawn from Sala et al. (2018).

3.1 Geometries and techniques

Both near-field and far-field ptychography have become established high-resolution imaging techniques able to produce phase-contrast images. They are routinely and increasingly applied at many high-brilliance X-ray sources worldwide (Takahashi et al., 2011; Beckers et al., 2011; Schropp et al., 2012; Maiden et al., 2013; Shapiro et al., 2014; da Silva et al., 2017c; Vogt et al., 2017). However, being scanning techniques, they both impose an obvious trade-off between the size of the imaged area and the time necessary to scan the X-ray beam over it. This makes it a key asset to be able to rapidly identify specific areas of interest on which to apply lengthy high-resolution scans. A common approach to tackle this issue is the use of an X-ray camera or X-ray eye, i.e. a video camera coupled with a scintillator which provides live feedback on sample position and orientation. Similarly, an online visible-light microscope is sometimes used for the same task. Scanning transmission X-ray microscopy (STXM) too makes a well-known and strong candidate able to retrieve coarse wide images (cf Section 2.3). This latter technique has been developed at full-field X-ray microscopy beamlines (Chapman et al., 1995; Gianoncelli et al., 2006; Stampanoni et al., 2010; Kaulich et al., 2011) providing an efficient way of probing even wide areas with little processing requirements and with an achievable resolution determined by the used beam size. When exploiting tightly focused beams, STXM can produce high-quality images resolving nanometric features (Mohacsi et al., 2017). However it has been shown that STXM scans can also support far-field ptychography experiments by exploiting the same geometry and requiring significantly less processing to provide wide overviews of whole specimens (Thibault et al., 2008; Shapiro et al., 2014; da Silva et al., 2015; Guizar-Sicairos et al., 2015a).

Stemming from this application, a flexible multiscale imaging protocol has been implemented and established for both near-field and far-field ptychography experiments to be performed at any high-brilliance X-ray source in combination with other imaging methods to obtain both wide FOV images of whole specimens and submicrometre-resolution images of specific regions of interest. For the far-field propagation regime this is achieved by combining ptychography with STXM while in the near-field an approach which exploits full-field transmission images produced by a wide parallel beam is used instead. For simplicity, this latter approach will be referred to as parallel-beam holography.

The protocol includes three different geometries accessible at the I13-1 Coherence Branchline at Diamond Light Source which can be remotely and reversibly swapped via simple motor translations. This approach allows for the four complementary propagation-based scanning X-ray microscopy techniques to be used interchangeably thus providing a flexible means to investigate extended samples at multiple scales. These techniques are parallel-beam holography (PBH), scanning transmission X-ray microscopy (STXM),

near-field ptychography (NFP) and far-field ptychography (FFP). While PBH returns plain unprocessed transmission images, STXM is able to produce differential phase-contrast and dark field images too when a suitable detector is used, i.e. a position-sensitive detector such as a segmented or pixelated one. Both NFP and FFP lead to the reconstruction of the complex-valued transmission function of the projection of the imaged area thus providing both absorption- and phase-contrast images.

The used geometries are represented in Fig. 3.1. They involve focusing optics based on a Fresnel focusing zone plate (FZP) system as that is the focusing system routinely available at the beamline where the protocol has been first implemented and tested. Equivalent geometries exploiting other forms of focusing optics can also be applied within the same imaging protocol. Three different geometries are used: one based on a parallel beam and the other two on a divergent beam. The use of a monochromatic beam is

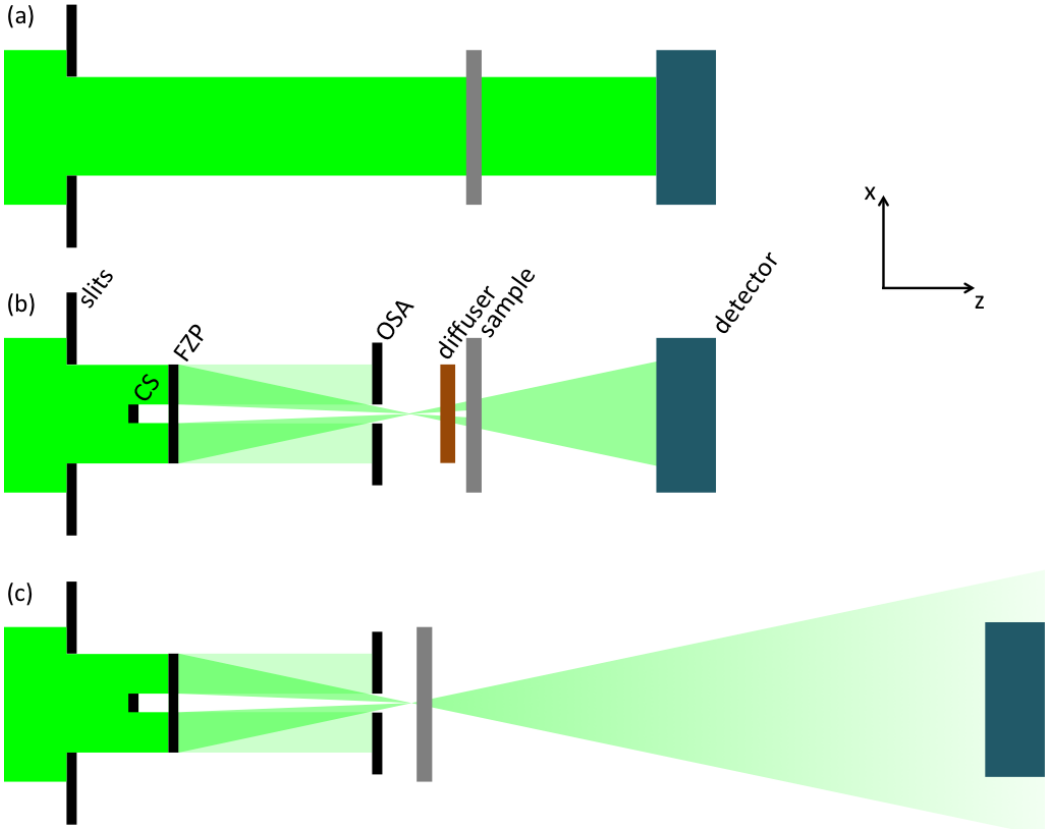

FIGURE 3.1: Schematic representation of the three geometries used within the proposed protocol. The elements annotated on the figure are beam-shaping slits, a central beam stop (CS), a Fresnel focusing zone plate (FZP), an order-sorting aperture (OSA), a cardboard diffuser, the sample and a detector. (a) Geometry suited for parallel-beam holography, generating wide field-of-view (FOV) and low-resolution images. (b) Geometry suited for near-field ptychography, producing intermediate to small FOV and submicrometre-resolution images. (c) Geometry suited for scanning transmission X-ray microscopy producing images within a wide range of FOVs and resolutions, and suited for far-field ptychography for small FOV and high-resolution images. This figure has been adapted from Sala et al. (2018) and permission to reproduce it has been granted by Diamond Light Source (DLS).

highly preferable for the success of the imaging techniques involved in the protocol. Furthermore a monochromatic beam is also necessary for a FZP system to successfully focus it. For these reasons the use of a monochromator is assumed upstream from all geometries. Then moving downstream along the optical axis (z) some beam-shaping adjustable slits are found which determine the secondary source size. In both divergent beam geometries further optical elements used are a central beam stop (CS), a FZP and an order-sorting aperture (OSA) which together form the FZP-based focusing system and are each individually mounted on 3-axis translation stages. Also a diffuser mounted on another 3-axis translation stage figures in the second geometry as that has been found to be sometimes beneficial for near-field ptychography measurements which rely on a structured illumination. In all geometries, further downstream the specimen is mounted on top of a high-precision translation and rotation stage followed by a detector with no other optical element needed between them as only propagation-based microscopy techniques are involved.

As requirements are typically different for the imaging techniques involved, two different detectors have been envisioned for the proposed protocol: one to be used in the near-field propagation regime and another one for far-field. They are both mounted on translation stages in order to be easily swapped within an experiment when switching between different imaging techniques. For far-field measurements a high dynamic range is required which makes a photon-counting detector the ideal choice. Photon-counting detectors are diode-based systems in which every pixel converts X-ray photons directly into an electronic current ensuring the absence of dark current and read-out noise. On the other hand, the main requirement of near-field measurements is a small pixel size which makes photon-counting detectors less preferable due to their pixels being several tens of micrometres wide. Scintillator-based systems are typically used instead which involve a scintillator converting X-rays into visible light then detected by a visible light detector such as a CCD or CMOS camera. These cameras have pixels only a few micrometres wide but suffer from the presence of dark current and read-out noise which both contribute to the overall detector point spread function (PSF). In order to further reduce the effective detector pixel size, magnifying optics is often added to such detecting system which also negatively affects the PSF. Furthermore the quantum efficiency of a scintillator – i.e. the probability of an X-ray photon to be converted into visible light – increases with its thickness although together with the probability of multiple scattering events for both X-ray and visible light photons which is in turn a further source of noise. This results in near-field detectors achieving an effective pixel size 2 orders of magnitude smaller than far-field detectors at the expense of a larger PSF and presence of noise.

All the elements of the experimental setup mentioned so far need careful alignment. The monochromator has to be oriented in such a way that the exiting monochromatic

beam reaches both sample and detector. Adjustable slits are centred in x and y around the monochromatic beam in order to let a portion of it through, such that its cross section around the focusing optics position is at its brightest and flattest. Focusing optics also has to be carefully adjusted to generate a tight well-characterised focus. In the case of a FZP-based system, all three elements involved are aligned in x and y and positioned in z with respect to one another with the aim of having mostly the first order beam diffracted by the FZP reaching its focal distance, whereas most of the lower and higher orders are shadowed out by CS and OSA. At their different positions in z, sample stages are aligned in x and y with respect to the beam, with particular care at having the axis of rotation at its centre, mostly relevant only for 3D experiments. Positions in x and y often differ at different z positions due to slight misalignment between the optical axis and the motor translation direction. Finally, both near-field and far-field detectors are aligned in x and y to the centre of the beam, therefore also having the projection of the sample's axis of rotation at the centre of their FOV.

In principle. this whole alignment procedure only needs to be carried out or tested once at the beginning of each experiment: in fact, unless large changes in beam energy are foreseen, the properties of the beam remain untouched throughout. Most imaging beamlines are able to provide users with an experimental setup whose optics has already been aligned. In general, all motor positions can be saved, so that alignment reduces to fine-tuning their relative position in order to correct for long-term drifts of any of the stages involved, which is typically a rather quick and straightforward procedure. Some beamlines implemented interferometers to continuously monitor geometry and actively correct for small drifts.

In the first geometry (Fig. 3.1a), the parallel beam shaped by the adjustable slits illuminates the specimen directly with no further optical element involved and interacts further downstream with the near-field detector. This way holograms of areas up to a few mm across can be measured by scanning the specimen on a x-y grid using a wide beam and a step size which could be as wide as the beam itself. Collected holograms are then stitched together to form larger absorption-contrast images typically containing the whole sample. Such a stitched hologram can take a few minutes of measuring time and produce an image of several tens of megapixels.

The second geometry (Fig. 3.1b) is used to run NFP scans and is achieved by inserting the focusing optics (CS, FZP, OSA) and the diffuser into the beam path. The sample is then positioned downstream to the focus such that it is illuminated by a perturbed divergent beam some tens of micrometres wide which then propagates till the near-field detector. Such a geometry allows to produce complex-valued images with submicrometre resolution from ptychographic scans run on relatively wide areas, typically up to a few times the beam size and taking several tens of seconds to be collected.

The third geometry (Fig. 3.1c), suited for both STXM and FFP measurements, is produced from the second by swapping the near-field detector with the far-field one, removing the diffuser, and translating the sample closer to the focal position. Like the wide holograms obtained from the first geometry, STXM images of whole samples of several tens of micrometres can easily be generated from frames collected in a few minutes in this geometry. Using this technique, the acquisition time increases with the inverse square of the beam size in the sample plane while the resolving power increases linearly: this leads to a trade-off that needs to be carefully balanced depending on the experimental requirements and which is further commented upon below. On the other hand, ptychographic reconstruction of diffraction patterns collected in this geometry leads to the achievement of the highest half-period resolution, often around a few tens of nanometres, with scanning times usually ranging in the order of a few minutes for imaged areas a few tens of micrometres wide.

All these geometries are compatible with 3D imaging experiments as the presence of a rotation stage beneath the sample stage allows to carry out conventional tomography in any of the configurations. This approach has in fact been already established for both FFP (Dierolf et al., 2010) and NFP (Stockmar et al., 2015a) where 2D projections are reconstructed at several sample orientations thus forming a tomographic dataset suited for the retrieval of quantitative phase-contrast volumetric information. Furthermore these geometries also allow for on-the-fly scans to be performed which can be handled by ptychographic reconstruction algorithms as mentioned in Section 2.4.5. These are expected to greatly decrease the acquisition time for each scan – even by more than one order of magnitude – which is a critical factor for most 3D measurements (Pelz et al., 2014; Clark et al., 2014; Deng et al., 2015a).

Beyond the experimental setup, the availability of powerful data analysis tools is essential to fully benefit from the flexibility of multiscale experiments. There already exist some established packages for ptychography (Maiden and Rodenburg, 2009; Marchesini et al., 2016). and *PtyPy* (Enders and Thibault, 2016) has been used to test the proposed protocol. *PtyPy* is an open-source Python package which offers ptychographic reconstruction algorithms for both near-field and far-field datasets. Customised parameters should be selected on a case-by-case basis, but ptychographic reconstructions are usually based on the same principles: a few hundred iterations of the difference map algorithm (DM) followed by several hundred iterations of maximum likelihood (ML) refinement, using a few mixed states to account for various sources of loss of coherence. This yields the sample's complex-valued transmission function from which absorption and phase-contrast images can be generated.

PtyPy also provides a convenient library to handle and process scanning datasets in general. For PBH, each hologram is fed into a data management container and a wide

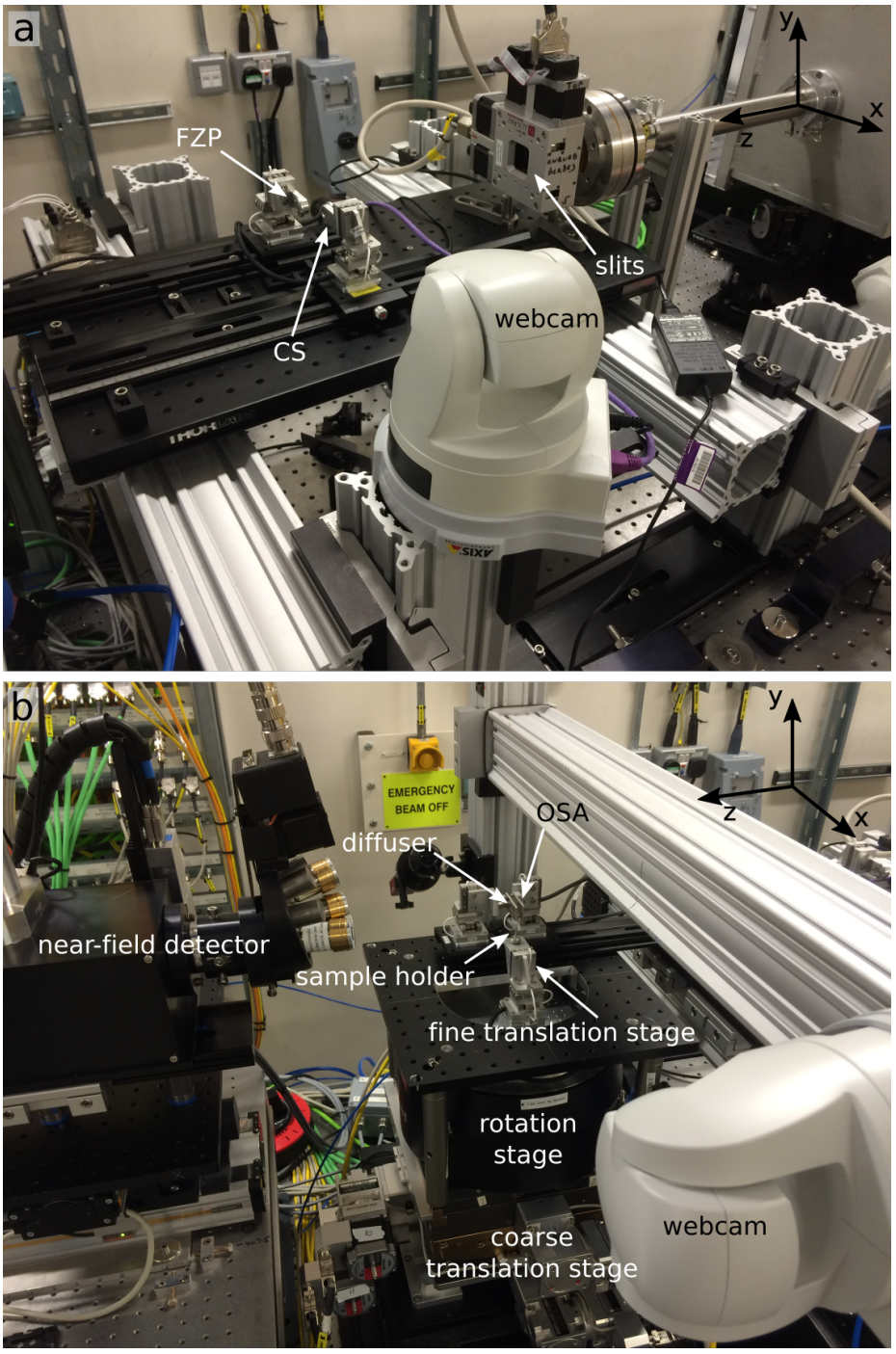

FIGURE 3.2: Photographs of experimental setup used for multiscale protocol. (a) Most upstream part of the experimental hutch. The X-ray beam is coming in from the photon guide through beam-shaping slits and propagates along the optical axis z. The central beam stop (CS) and the Fresnel focusing zone plate (FZP) are visible. (b) The X-ray beam keeps propagating along the optical axis z and reaches the sample region or interaction region. The order-sorting aperture (OSA), the diffuser and the sample holder are visible. The X-ray beam propagates farther to the near-field detector. All of the focusing optics (CS, FZP, OSA), the diffuser, the sample holder and the near-field detector are mounted on individual translation stages to move them in and out of the beam and allow for fine alignment. The sample holder is also mounted on a rotation stage on top of a coarse translation stage to allow for fine changes in orientation and wide changes in xyz positions, respectively. Webcams are available for remote monitoring.

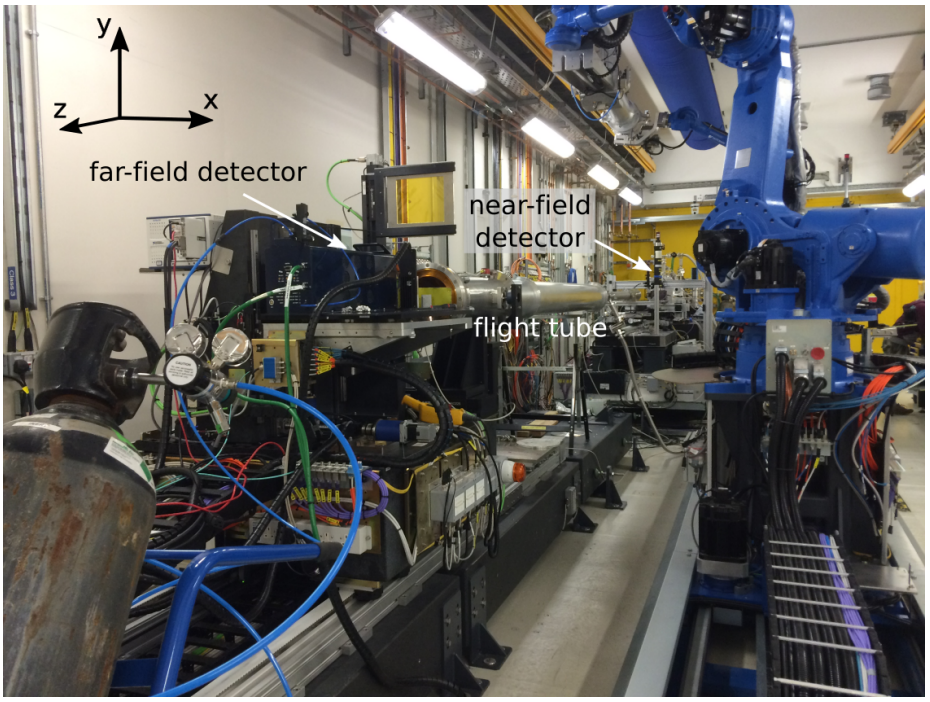

FIGURE 3.3: Photograph of experimental setup used for multiscale protocol. Most downstream part of the experimental hutch. The X-ray beam propagates from the direction of the near-field detector through a flight tube parallel to the optical axis z. The far-field detector is positioned at its end and is mounted on a translation stage to adjust its position along the optical axis z and to allow for fine alignment.

FOV image is stitched together through a procedure consisting of a weighted sum of each flat-normalised frame, taking into account the motor positions associated with each one of them. *PtyPy* also produces STXM images through a library which was complemented with a simple frame-by-frame analysis of the collected diffraction patterns: integration leads to transmission images, while computation of each diffraction pattern's centre of mass leads to refraction images, corresponding to differential phase contrast images.

3.2 Theoretical comparison

A wide range of length scales can be investigated exploiting the experimental protocol described in Section 3.1. This can be represented as in Fig. 3.4 where comparisons between scanning areas, acquisition times and resolving powers best accessible with each technique within the proposed protocol are schematically summarised highlighting their complementarity. Fig. 3.4a shows the domain of each colour-coded technique in the logarithmic space of acquisition time and scanning area where the former represents the time required to complete a whole scan and the latter the size of the image retrieved through such scan. For simplicity a one-dimensional value has been chosen to represent the scanning area which is assumed to be square. On the other hand Fig. 3.4b shows a comparison of the different length scale regimes accessible with each technique.

The transparent colour-coded domain represents the whole range of achievable resolving powers from the smallest resolvable feature found in the literature to the largest still relevant to the proposed protocol. The opaque bar is used to annotate the pixel size of images obtained through each technique.

Opaque domains in both plots refer to geometries and setup elements selected to be representative of typical experimental conditions. A 10 keV beam energy is selected to be representative of hard X-rays experiments. A 400 µm Fresnel focusing zone plate with 150 nm outermost zone width is chosen as focusing optics. Also a mirror-based focusing system which produced a beam with the same divergence could be employed without altering the outcome. Mirror-based focusing systems are an alternative solution often found at imaging beamlines and they offer the advantage of achromaticity and high-efficiency. A 2000x2000 pixel detector with a pixel size of 0.4 µm after optical magnification is assumed for near-field and a 500x500 pixel detector with 50 µm pixel size for far-field. A minimum detector exposure time of 0.8 s is assumed for all techniques keeping in mind this value would be significantly smaller for faster experiments such as those involving high-flux and on-the-fly scans. Chosen beam size varies among techniques such that for PBH it is 300 µm, for NFP it is 80 µm and for STXM and FFP it is 12 µm. The minimum degree of overlap between the areas illuminated at adjacent scanning points is set to 0% for PBH and STXM, 71% for NFP and 50% for FFP, implying that for each technique each point was illuminated once, 12 times and 4 times respectively; this is an approximation which ignores boundary effects, i.e. the scanning points framing the scanned area. Finally the sample-to-detector distances are determined such that the divergent beam illuminates about 50% of the near-field detector area and takes up at most 21% of the area sampled in Fourier space by the far-field detector thus ensuring a high degree of oversampling.

Image pixel sizes from Fig. 3.4b can be used for comparison purposes as reliable figures of merit as they only depend on the chosen experimental geometries whereas the actual resolution achieved within any experiment varies significantly with the imaged specimen and only stems from the image pixel size rather than equating to it. Nonetheless it could be useful to keep in mind the qualitative relationship between image pixel size and achieved resolution within geometries closely related to the ones considered to generate Fig. 3.4. Using PBH, it should be expected that only features significantly larger than the image pixel size – typically by one order of magnitude – would be resolvable. This is due to the fact that propagation effects cause blurring in the unprocessed near-field images and give rise to fringes. At the same time edge-enhancement effects make PBH even more effective as low resolution technique suited for investigating the general morphology of an uncharacterised specimen. On the other hand the actual resolution of STXM images corresponds to the beam size used to produce them which could be slightly larger than

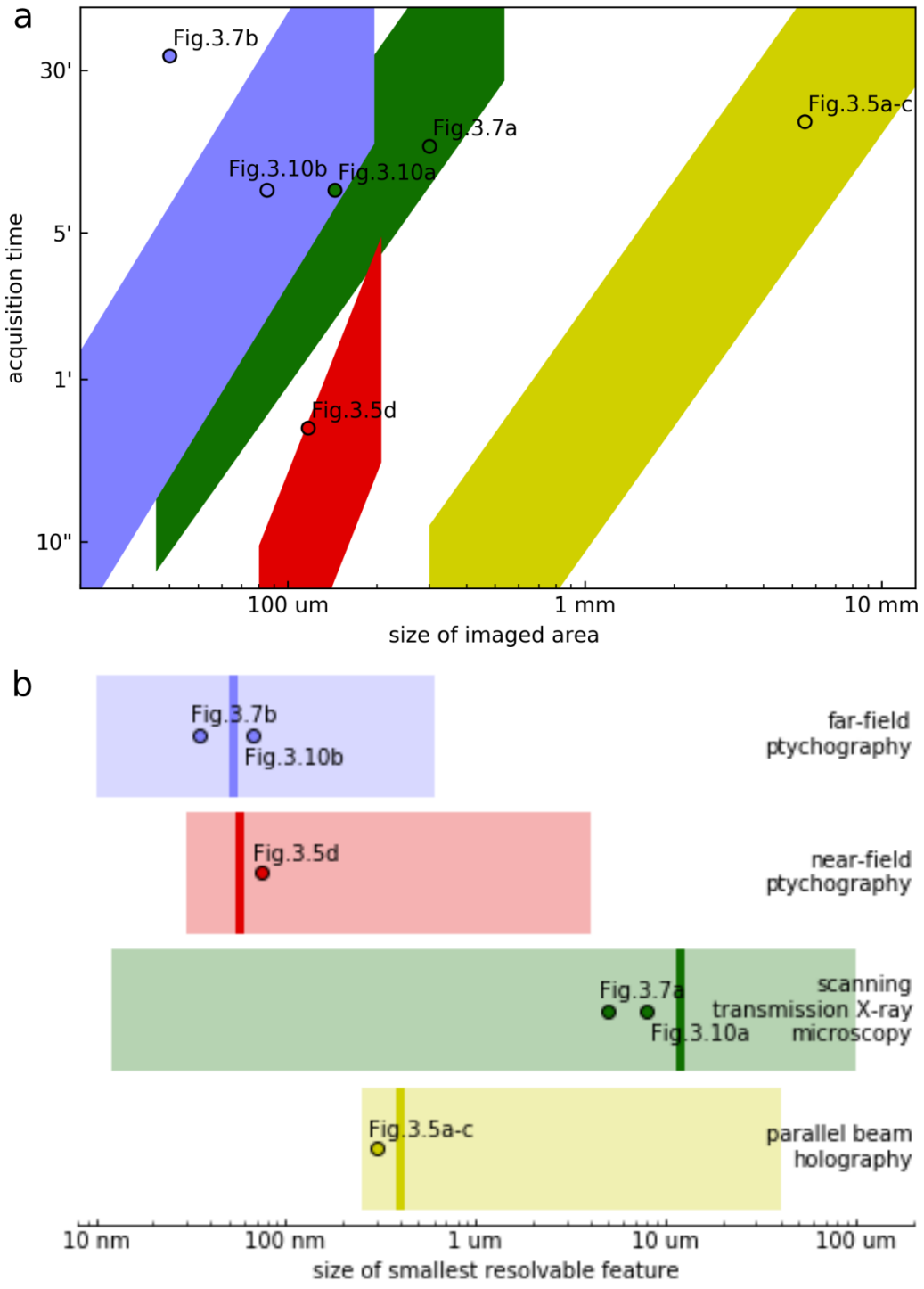

FIGURE 3.4: Comparison between imaging techniques available within the proposed protocol. Colour-coded techniques domains in logarithmic space of (a) acquisition time and scanning area and (b) size of smallest resolvable feature, based on typical experimental parameters. In (b) transparent domains indicate the regimes accessible in general through each technique and opaque lines indicate the image pixel size obtained with the experimental parameters considered for (a). Values relative to experimental results presented in other figures in this chapter are annotated as circles, colour-coded to technique. Colour-coding is labelled in (b). This figure has been adapted from Sala et al. (2018) and permission to reproduce it has been granted by Diamond Light Source (DLS).

their pixel size as the latter is given by the scanning step size. Finally both NFP and FFP often achieve resolutions of only a few pixels but especially for these techniques resolutions largely depend on the imaged specimens and their properties.

It should be noted that Fig. 3.4 is not aimed at giving a rigorous picture of the extent of each domain but rather it acts as guideline in showing what typical ranges are for the available techniques providing a tool to compare them and assess which to select for each need. These ranges depend in fact on a combination of variables which cannot all be rigorously represented in the same plot and have been chosen to be representative of those that would be optimally used within the proposed protocol. The variables considered for the realisation of Fig. 3.4 which have already been listed can be varied within imaging experiments and some of them can significantly affect each technique's domain. In general they can be divided into two categories. On the one hand near-field and far-field detectors as well as focusing optics often only depend on what is already available at the facility where the imaging experiment takes place: these could therefore be considered hardware constraints. On the other hand there are experimental parameters than can more easily be varied within existing imaging setups: this is the case for overhead, detector exposure time, scanning step size and beam size at sample position.

Overhead t_{oh} is caused by hardware limitations and has no effect other than uniformly slowing down the scanning procedure. It is typically the sum of sample motor overhead and communication overhead. The former occurs whenever the sample is translated by discrete steps in between collection of frames at each point of extended scans as both motor translation and settling take a finite amount of time during which no measurement takes place. The latter includes all non-measuring time necessary for the communication to occur among the various hardware components of the setup, typically between motors, controllers and detector. The increase of acquisition time caused by overhead is sometimes overcome by replacing move-settle-measure scans with continuous or on-the-fly scans which require however a more sophisticated analysis.

Exposure time (or dwell time) t_{exp} is more freely adjustable and is usually chosen on the principle of as short as possible and as long as necessary in that the goal is ultimately to collect raw frames with signal-to-noise ratio high enough to retrieve images of the specimen. For STXM and PBH low or noisy signal can compromise the quality of the reconstruction, mainly in terms of contrast, while for NFP and FFP it could even prevent reconstruction algorithms from converging altogether, e.g. when speckle visibility is compromised.

Scanning step size should be selected to be as large as possible in order to reduce overall acquisition time. In the case of STXM and PBH this could be as large as the beam size as all frames are processed individually and can be stitched together based

solely on the recorded motors positions. This 0% overlap has been taken as the lower boundary for generating Fig. 3.4. However the stitching procedure would benefit from some degree of overlap between adjacent frames which in the case of holograms could even be used to correct for errors in the recorded motors positions and distortions in the acquired frames. In the case of NFP and FFP, the scanning step size is a fraction of the beam size as enough overlap between adjacent illuminated areas is necessary for the reconstruction algorithms to tackle the phase problem and hence converge. This parameter can also be represented as the degree of overlap (or redundancy) r necessary among illuminated areas, i.e. the number of times each area is illuminated throughout a scan.

The beam size b too should be selected to be as large as possible to accelerate the scanning procedure, always keeping in mind an increase in beam size entails an increase in the image pixel size for all techniques but PBH for which the pixel size corresponds to the available near-field detector pixel size. So for PBH beam size is only limited by the size of the beam available upstream the optics and the beam-shaping slits can be opened wide as long as a reasonably small secondary source size is preserved.

Combining all the variables introduced, one can seek the general dependency of the total acquisition time t_{aq} per scan. Assuming a square beam $b_x = b_y = b$, one obtains

$$t_{\mathrm{aq}} = (t_{\mathrm{exp}} + t_{\mathrm{oh}}) N_{\mathrm{frames}} = (t_{\mathrm{exp}} + t_{\mathrm{oh}}) \frac{X\,Y}{r\,b^2} \tag{3.1}$$

where N_{frames} represents the number of frames collected and X and Y the one-dimensional sizes of the area imaged within the scan. As t_{exp} and t_{oh} are experiment-dependent and r is limited by the technique used, the general relation $t_{\mathrm{aq}} \propto XY/b^2$ is found.

Similarly, the technique-specific dependencies of the achievable image pixel size p can be formalised. As already mentioned, for PBH this is

$$\text{PBH:}\ \ p = p_{\mathrm{det}}^{\mathrm{NF}} \tag{3.2}$$

with $p_{\mathrm{det}}^{\mathrm{NF}}$ representing the near-field detector pixel size.

For STXM every frame corresponds to a pixel so that when the smallest degree of overlap is used ($r = 1$) one finds

$$\text{STXM:}\ \ p = b \tag{3.3}$$

once more highlighting the trade-off mentioned in the Section 3.1.

For NFP

$$p = \frac{p_{\mathrm{det}}^{\mathrm{NF}}}{M} = \frac{p_{\mathrm{det}}^{\mathrm{NF}}\, z_1}{z_1 + z_2} \tag{3.4}$$

with $p_{\mathrm{det}}^{\mathrm{NF}}$ as the near-field detector pixel size, M as the magnification caused by the divergent beam, z_1 as the focus-to-sample distance and z_2 as the sample-to-detector distance. The geometry is typically fixed such that a specific area of the near-field detector is illuminated, so focus-to-detector distance $z_1 + z_2$ is constant. As $p_{\mathrm{det}}^{\mathrm{NF}}$ is a hardware parameter, this leaves $p \propto z_1$, but z_1 is chosen to obtain a specific beam size onto the sample and, in the case of a Fresnel zone plate of diameter D_{FZP} and focal length f, $z_1 = b\,f/D_{\mathrm{FZP}}$. Once again treating hardware parameters as constant leads to the general relation

$$\text{NFP:}\ \ p \propto b \tag{3.5}$$

similar to the STXM case.

Finally for FFP

$$p = \frac{\lambda\, z_2}{D_{\mathrm{det}}^{\mathrm{FF}}} = \frac{\lambda\, z_2}{N_p^{\mathrm{FF}}\, p_{\mathrm{det}}^{\mathrm{FF}}} \tag{3.6}$$

with λ as X-ray beam wavelength, z_2 as sample-to-detector distance and $D_{\mathrm{det}}^{\mathrm{FF}}$, N_p^{FF} and $p_{\mathrm{det}}^{\mathrm{FF}}$ as the far-field detector size, number of pixel and pixel size respectively. Keeping λ and the detector parameters as constant, one gets $p \propto z_2$ which for speckle-resolution constraints needs to satisfy $z_2 > b\,2p_{\mathrm{det}}^{\mathrm{FF}}/\lambda$ which once more reduces to

$$\text{FFP:}\ \ p \propto b \tag{3.7}$$

similarly to the STXM and NFP cases.

The general dependencies $p \propto b$ and $t_{\mathrm{aq}} \propto XY/b^2$ have been found, describing the relations between selected beam size and image pixel size and between beam size, size of imaged area and total acquisition time respectively. Both relations further highlight the trade-offs which need to be taken into account when selecting the most efficient imaging technique for a specific goal.

Finally, a further element to be weighed in is the processing time associated with each technique. For well-characterised and optimised systems this typically lies in the order of minutes for STXM and PBH which only require limited computational resources. On the other hand both NFP and FFP involve reconstruction algorithms which run for several iterations before approaching convergence thus pushing processing time in the hours. This is often reduced by employing larger computational resources – namely multiple cores or GPUs – but still needs to be considered in the context of time-limited experiments.

3.3 Implementation and experimental results

Taking into consideration the complementarities discussed so far, a few experiments have been performed at the I13-1 Coherence Branchline at Diamond Light Source exploiting the most efficient combination of techniques suited for each situation. The measurements involved a series of specimens of different sizes and compositions covering the full scale range, the largest sample spanning several millimetres in size and the smallest features lying in the sub-100 nm regime. Images from three biogenic specimens are shown which are representative of extreme cases, i.e. located at either end of the length scale range accessible within the multiscale imaging protocol. It is worth noting that for these experiments all specimens satisfied the projection approximation. It is expected that extending these methods to samples significantly thicker than the depth of field would require to take into account the probe changes as it travels within the sample. This is relevant in particular for the high-resolution techniques, namely both near-field and far-field ptychography, and some algorithmic approaches have been successfully proposed to tackle this issue (Maiden et al., 2012a; Suzuki et al., 2014; Tsai et al., 2016).

All experiments have been carried out exploiting hardware already available at the beamline. A pseudo- channel-cut crystals Si monochromator was used to produce a monochromatic hard X-ray beam. For the divergent beam geometries a FZP-based focusing system was in place which exploited a 40 µm central beam stop, a 400 µm Fresnel focusing zone plate with 150 nm outermost zone width and a 25 µm order-sorting aperture. For near-field measurements a diffuser was produced from a piece of cardboard and measurements in this regime were collected with a scintillator-coupled pco.edge 5.5 cSMOS camera. This detector had 2560x2160 pixels 6.5 µm each, giving a magnified pixel size of 0.29 µm after a scintillator was coupled through a 20X objective lens. Finally far-field measurements were carried out with EXCALIBUR, a photon counting detector based on the Medipix3 chip with 2069x1796 pixels, 55 µm each (Marchal et al., 2013).

3.3.1 Imaging of a fossil fish bone

The first experiment in which the proposed protocol has been tested was run on a fossil (sample 1), the widest among the biogenic samples involved. This took the form of a silica slab a few millimetres wide, embedded in resin and polished down to a thickness of about 20 µm, resulting in a thin tile-like sample. This was clipped standing upright on top of a sample holder using a screw. The holder was oriented in such a way as to minimise the path X-ray photons had to travel through it, i.e. the main plane of the flat sample was perpendicular to the optical axis.

The fossil was extracted from a fragment of the bone of an extinct fish (genus *Psammolepis*) whose bone repair mechanism involved dentine and is of current interest for the

paleontological community (Johanson et al., 2013). It can be considered as an example representative of the high end of the accessible length scale range.

The experiment was performed at an X-ray energy of 9.7 keV. According to Fig. 3.4a the fastest way to get an overview of an area large enough to cover the whole sample was through a PBH scan. So the parallel-beam geometry was used and the monochromatic beam was shaped down to a rectangular size of 458x438 µm^2 using the adjustable slits. The sample was scanned transverse to the beam along a 31x15 rectangular grid using a 250 µm step size, which ensured a significant amount of overlap among frames was available for post-acquisition corrections. PBH data collection took 17 minutes, for a total of 372 megapixels. The simple stitching procedure described at the end of Section 3.1 returned the low resolution transmission image shown in Fig. 3.5a. Its pixel size is the same as the detector pixel size, namely 0.29 µm. After having identified a relatively sharp isolated feature within the sample, a gaussian curve was fitted through a line plot perpendicular to its edge. The result obtained is shown in Fig. 3.6a and gave a half width at half maximum (HWHM) of 6 µm. This could be used as coarse estimate of the achieved resolution which then results some 20 times larger than the pixel size, in agreement with what qualitatively outlined in Section 3.2 for PBH.

As the stitched hologram made for a rather large image to handle, smaller sections have been produced from it: an example is shown in Fig. 3.5b as a zoomed in version of the inset from Fig. 3.5a. This made possible the identification of smaller regions of interest which were some 80 µm in size and did not require to resolve features smaller than 100 nm. NFP was identified as the most suitable candidate to swiftly image those smaller regions. Focusing optics and diffuser were moved in to get to the geometry shown in Fig. 3.1b. Having positioned the sample some 90 mm downstream to the focus produced by the FZP gave a beam size of 77 µm which propagated to the scintillator camera some 65 mm further downstream, in the near-field regime. This geometry combined with the magnification effect of the divergent beam and led to an effective pixel size of 74.3 nm for the recorded near-field images.

A customised sample scanning pattern was prepared consisting of two series of 5 and 10 points equally spaced along concentric circles of 10 µm and 20 µm radii, respectively, for a total of 15 scanning positions, spanning a 40x40 µm^2 area. Such scanning pattern was used to run NFP measurements on the regions of interest identified from the wide PBH image. Detector exposure time was set to 2 s in order to achieve a useful signal-to-noise ratio, for a total scan duration of around 35 s, including overhead. The collected data was then rebinned by a factor of 2, to get a more manageable file size, and processed using 500 iterations of DM reconstruction algorithm in *PtyPy*.

An example of the images obtained from such scans is shown in Fig. 3.5d, as the phase part of the reconstructed complex-valued transmission function of the area from

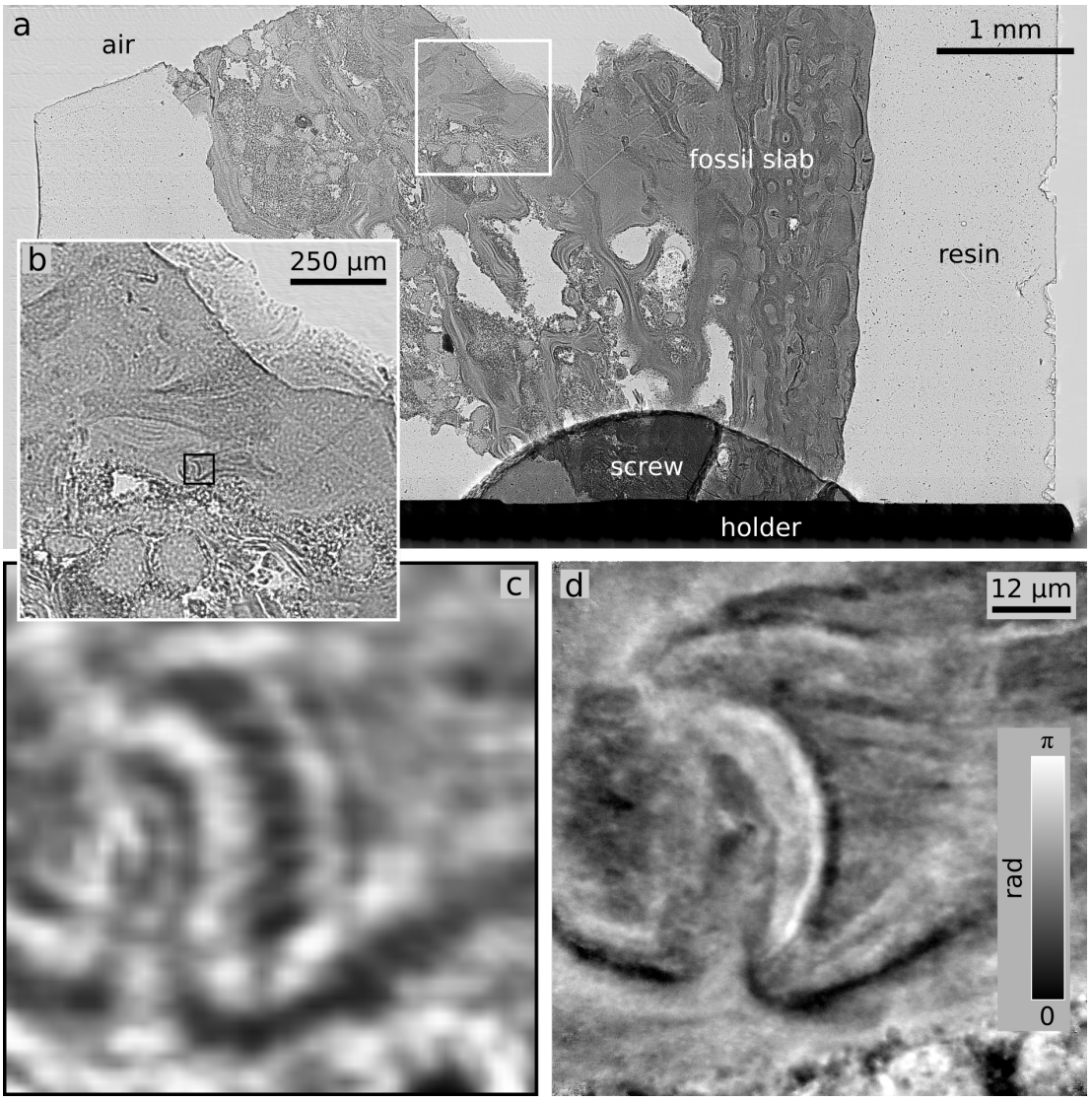

FIGURE 3.5: Reconstructions of the fragment of a fossil fish bone (sample 1). (a) Transmission image of the whole sample obtained from parallel-beam holography data; arbitrary units. The projection of the slab of fossil fish bone embedded in resin is fully visible. Some air surrounds the thin slab and both sample holder and its screw – used to hold the slab in place – are visible at the bottom. (b) Magnified inset from (a). (c) Magnified inset from (b). (d) Relative phase shift from the near-field ptychographic reconstruction of a scan performed on the area of the inset in (b), i.e. the same area as (c). (c-d) focus on a feature which is part of a small bone fracture, possibly forming an interface between the original bone and an area repaired with dentine. The gain in resolving power between the image obtained via parallel-beam holography (c) and the one from near-field ptychography (d) is apparent. Colour scaling differs in (a-c) and (d) as contrast relies on absorption for the former and on phase-shifting for the latter. This figure has been adapted from Sala et al. (2018) and permission to reproduce it has been granted by Diamond Light Source (DLS).

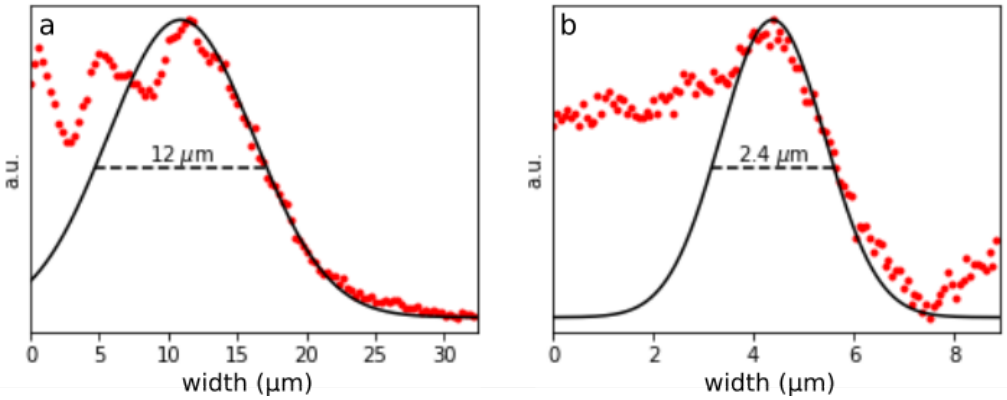

FIGURE 3.6: Gaussian fits were used to determine the half-period resolution of the images obtained from the fossil fish bone (sample 1). (a) Gaussian fit (black line) through data (red dots) from parallel-beam holography image (cf Fig. 3.5a-c). (b) Gaussian fit (black line) through data (red dots) from near-field ptychography image (cf Fig. 3.5d). Full widths at half maximum of both fits are annotated on each plot.

the inset in Fig. 3.5b. Fig. 3.5d can directly be compared with Fig. 3.5c which is an enlarged version of Fig. 3.5b cropped from the region of its inset, so that Fig.s 3.5c-d show the same region of sample. Fig. 3.5c was generated via PBH and relies on absorption contrast whereas Fig. 3.5d was generated via NFP and relies on phase contrast. The gain in resolving power of the NFP image with respect to the PBH one is apparent.

Using the same reasonably sharp feature already used for PBH, the achieved resolution for NFP has been estimated with another gaussian fit, as shown in Fig. 3.6b. The resulting HWHM had a value of around 1.2 µm, equivalent to 16 pixels. This should not be used as a general figure of merit for the method, but rather as a tool to compare NFP and PBH in terms of resolving power, as both estimates originated from the same feature whose actual sharpness cannot be conclusively assessed.

3.3.2 Imaging of a limpet tricuspid tooth

Another experiment involving the proposed imaging protocol was run on a tricuspid tooth (sample 2) extracted from a common limpet (*Patella vulgata*) which lies at the lower end of the accessible length scale range. Limpets are sea snails – common name for marine gastropods – provided with a tongue-like anatomical structure known as radula hosting thousands of teeth. They inhabit the neritic zone and in particular intertidal areas where they use their radula for feeding by scraping on the rocky substrates on which they are attached. Their teeth have recently been found to feature the highest tensile strength among biological materials (Barber et al., 2015). Made of 20 nm thin mineral fibres (goethite, α-FeOOH) in an organic matrix (chitin, $(C_8H_{13}O_5N)_n$) this sample required access to the highest resolution.

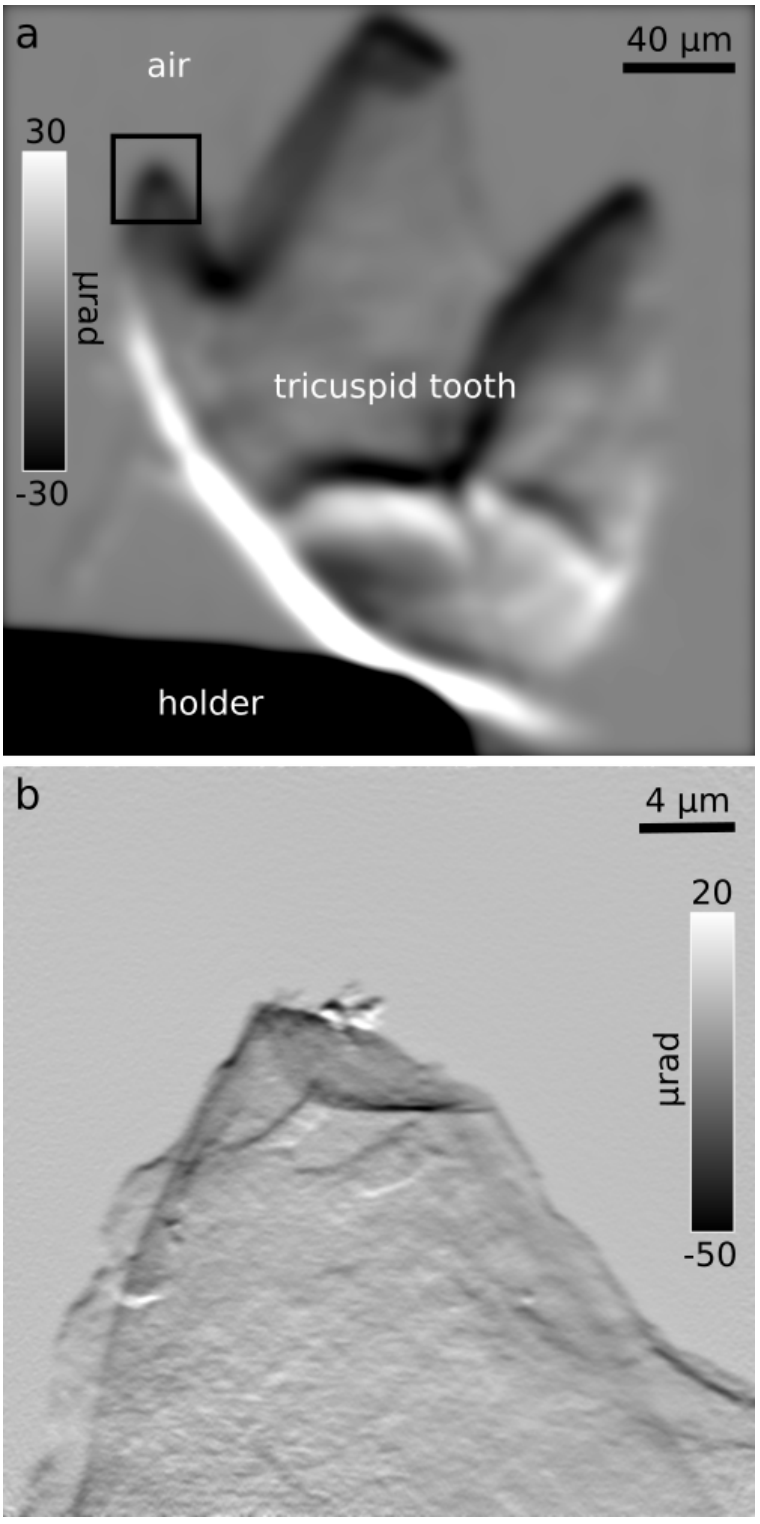

FIGURE 3.7: Reconstructions of a limpet tricuspid tooth (sample 2). (a) Vertical refraction image of the whole sample obtained from scanning transmission X-ray microscopy data. The three cuspids forming the tooth are clearly visible along with part of the sample holder at the bottom left corner. Background is air. (b) Vertical refraction image of single cuspid from inset in (a) obtained from a far-field ptychographic reconstruction: the gain in resolving power with respect to (a) is apparent. Nanofibres could not be resolved, partly on account of the thickness of the sample. This figure has been adapted from Sala et al. (2018) and permission to reproduce it has been granted by Diamond Light Source (DLS).

The isolated tricuspid tooth was only a few hundred micrometres across and could therefore be imaged whole starting from the far-field geometry directly. A 9.1 keV X-ray beam was used throughout. The sample was positioned some 11 mm downstream from the focus in order to have a beam size of around 10 µm which then propagated till the photon-counting detector positioned 7.19 m further downstream in the far-field regime.

In order to get a first overview of the whole sample, STXM data were collected by running a 61x61-point raster scan with a step size of 5 µm, thus covering an area of 300x300 µm^2. With a relatively short exposure time of 0.1 s, the scan took 13 minutes to complete. STXM data were easily processed within *PtyPy* following the procedure briefly summarised at the end of Section 3.1 thus generating transmission and both horizontal and vertical differential phase-contrast images. Fig. 3.7a shows a smoothed version of the refraction image obtained from vertical differential phase-contrast STXM data. In the context of this imaging protocol, STXM data are only used to quickly produce overview images which result coarsely pixelated. This case is no exception and relies on 3721 pixels in total, so using traditional methods to estimate the achieved resolution would not produce reliable figures. Applying the gaussian fit approach on the smoothed image would not be reliable either as that would only return values dependent on the filter used. In the case of STXM, the most robust estimate one can provide for the achieved resolution then stems from the beam size used to run the scan, which in the case of Fig. 3.7a corresponds to a value of 10 µm.

Despite such poor resolution, the general morphology of the sample is apparent and carried enough information to determine on which regions of interest (ROIs) to perform higher resolution scans: one of these was the tip of one of the cuspids (inset from Fig. 3.7a). As the highest achievable resolving power was necessary to aim at resolving the nanofibres hosted within this sample, a tight FFP scan was performed. This consisted of a 902-frame scan in which every frame was collected at a position located on a spiral path, efficiently covering a 30x30 µm^2 area. The distance among neighbouring positions was set to 1 µm in order to ensure a high degree of overlap and provide many constraints for the phase-retrieval algorithm to work on. Detector exposure time was set to 1.8 s to maximise signal-to-noise ratio which led to a collection time of 35 minutes. After masking and centring, the FFP frames gathered from the spiral scan have been cropped to a size of 512x512 pixels and processed within *PtyPy*, using a mixed state model involving 5 modes to represent the probe. After 500 DM and 1500 ML iterations, an object was retrieved whose phase part has been differentiated as in Fig. 3.7b to obtain a refraction image comparable to Fig. 3.7a. Fig. 3.8a shows the retrieved probe and its multimodal decomposition is represented in Fig.s 3.8b-f, along with the relative power of each mode. The main mode (Fig. 3.8b) accounts for the most power and secondary modes (Fig.s

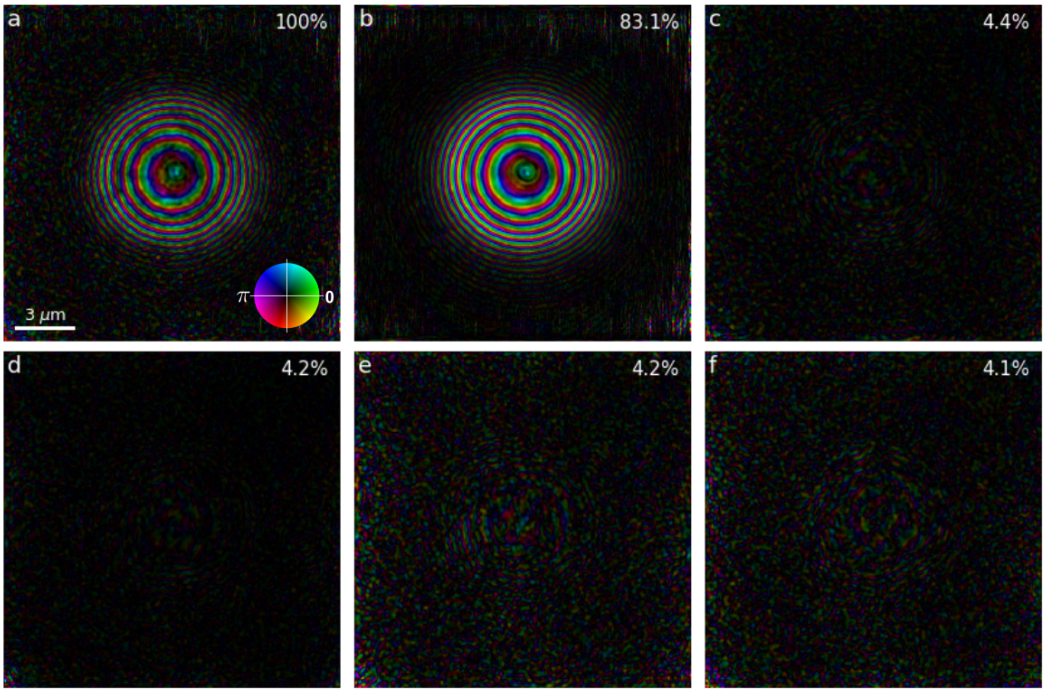

FIGURE 3.8: (a) Probe retrieved from ptychographic reconstruction on limpet tricuspid tooth (sample 2), resulting from 5 independent modes. (b-f) 5 orthogonalised modes making up the retrieved probe: secondary modes (c-f) mainly pick up on sources of decoherence. Relative intensity is annotated on top of each figure. Amplitude is mapped to brightness and phase to hue according to the colourwheel in (a).

3.8c-f) appear noisy, as if the ptychographic algorithm used them to account for various sources of decoherence.

Given the used geometry, the reconstruction pixel size is 34.8 nm. Even though no sharp edge was present in this reconstruction, the usual gaussian fit was still applied to the sharpest identifiable feature in order to produce a rough estimate of the achieved resolution. This fit is shown in Fig. 3.9a and the ballpark figure obtained through this process was a HWHM of just above 280 nm, corresponding to little over 8 pixels of the reconstructed image.

Some nanostructure can be observed directly from the reconstruction but goethite fibres are not resolved, most likely due to the thickness of the specimen which causes contribution from fibres at different depths to sum up in the reconstructed 2D projection. Such a situation is a clear example of a case in which the collection of 3D data is expected to be beneficial in detangling different contributions and hence possibly resolve individual fibres.

3.3.3 Imaging of a butterfly wing scale

Finally the proposed protocol was used for an imaging experiment run on a weakly scattering specimen (sample 3). This consisted of a cover scale extracted from the

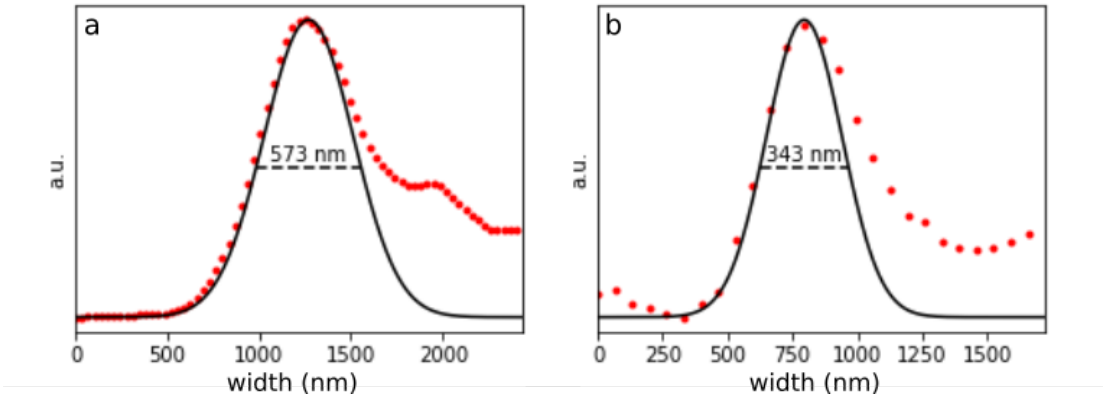

FIGURE 3.9: Gaussian fits were used to determine the half-period resolution of the images obtained via far-field ptychography. (a) Gaussian fit (black line) through data (red dots) from the limpet tricuspid tooth (sample 2) image (cf Fig. 3.7b). (b) Gaussian fit (black line) through data (red dots) from butterfly wing scale (sample 3) image (cf Fig. 3.10b below). Full widths at half maximum of both fits are annotated on each plot.

wing of a female pansy butterfly (*Junonia orithya*) which is known to contain chitin ($(C_8H_{13}O_5N)_n$) nanostructures responsible for the wing colouration thanks to interference effects. These nanostructures are present in different forms in most butterflies belonging to the same genus and constitute a marker of interest for evolutionary developmental biology (Wasik et al., 2014). Unlike the previous case of the limpet tooth (sample 2), the challenge this sample posed did not lie in the small size of its features but rather in the high degree of accuracy with which these needed to be repeatably measured as it is the size of these structures that varies among individuals rather than their general morphology. As this sample together with other butterfly scales was also the object of a more extensive study reported on in Chapter 5 it is described in more depth there.

The experiment was run using a 9.7 keV X-ray beam. The scale stretched just under 200 µm along its longest axis and therefore it could fit whole within the FOV of a STXM scan, as it was already the case for sample 2. So the experiment started from the far-field geometry directly. The sample was positioned some 15 mm downstream from the focus thus leading to a probe size of 13 µm. A He-filled flight tube connected the sample region to the photon-counting detector some 14.6 m further downstream in the far-field regime. An overview STXM scan was run exploiting an 18x18 raster grid with a step size of 8 µm thus covering an area of 144x144 μm^2 for a total of 324 frames. A detector exposure time of 0.9 s was used which led to a data acquisition time of about 8 minutes. STXM data have been processed producing the smoothed refraction image shown in Fig. 3.10a with a resolution estimated at 13 µm based on the retrieved beam size.

Higher resolution FFP scans were then run on different regions of the specimen to

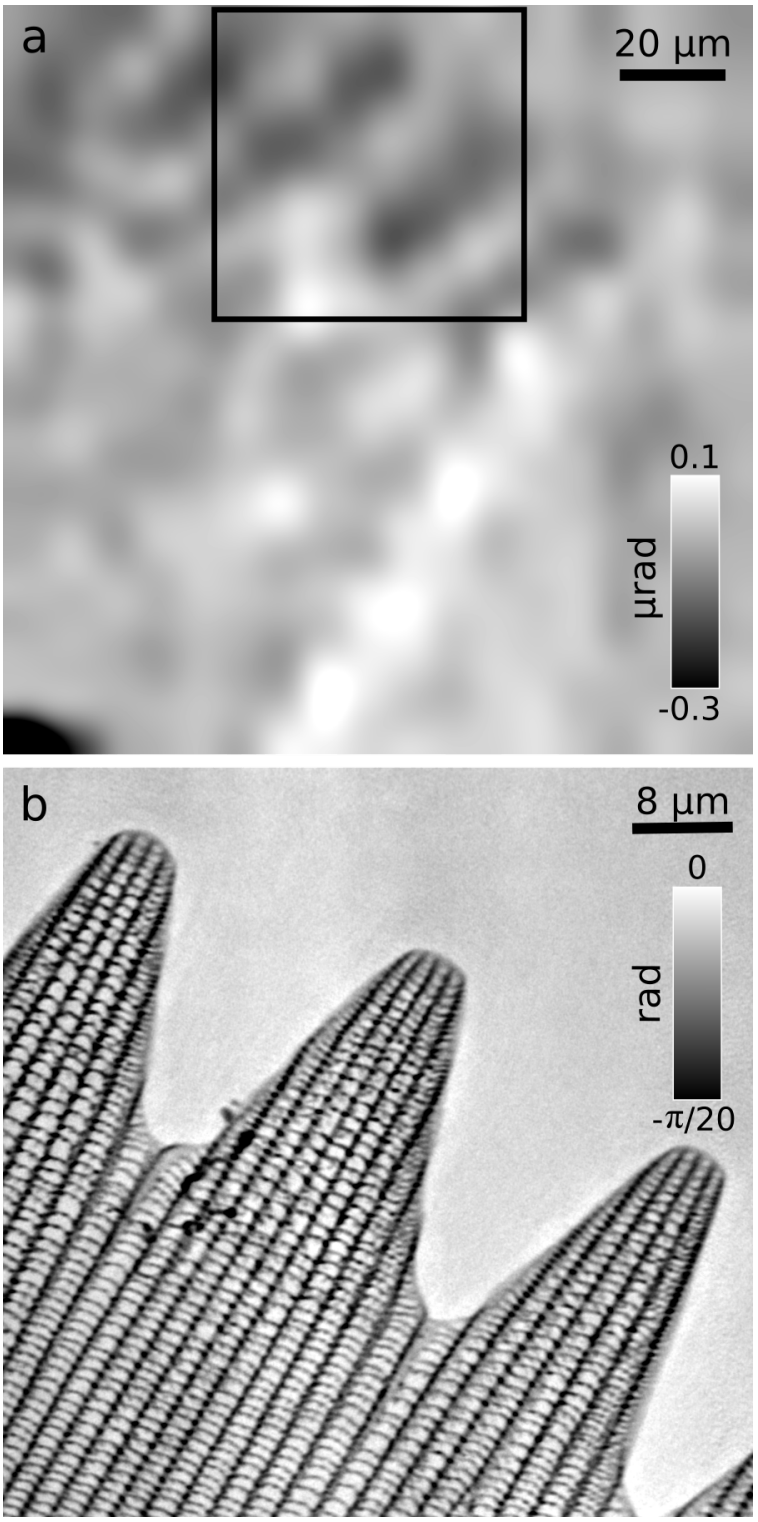

FIGURE 3.10: Reconstructions of a butterfly wing scale (sample 3). (a) Vertical refraction image of the whole sample obtained from scanning transmission X-ray microscopy data. The whole scale with its jagged top is clearly visible as well as part of the sample holder at the bottom left corner. Background is air. (b) Phase part of the far-field ptychographic reconstruction of a scan performed on the apical region from inset in (a). Nanostructures (axial ridges and crossribs) are clearly resolved. This sample and the results drawn from it are discussed in more detail in Chapter 5. This figure has been adapted from Sala et al. (2018) and permission to reproduce it has been granted by Diamond Light Source (DLS).

reveal nanometric features. One such scan was performed on a wide apical region exploiting a 17x19 perturbed raster scan with an average step size of 4 µm. Points falling outside an area of 68x76 μm^2 were discarded thus reaching a total of 318 collected frames, later all cropped down to 512x512 pixels. With a 0.9 s detector exposure time the scan took around 8 minutes to complete. Still within *PtyPy*, 2 modes have been used to model the illumination function and a reconstruction of the object has been obtained after 500 iterations of DM followed by 1500 of ML refinement. The phase part of the reconstructed object is shown in Fig. 3.10b which clearly highlights the axial ridges and cross-ribs covering the dorsal side of the scale. A gaussian fit estimate for the achieved resolution was carried out as shown in Fig. 3.9b and returned a value of 172 nm. Given a reconstruction pixel size of 66.3 nm, this is equivalent to roughly 2.5 pixels.

3.4 Conclusions

All the experimental results presented in this chapter can be compared with the general domains in Fig. 3.4 where they are annotated as circles coloured according to the technique they exploited. In particular the values for scanning area and acquisition time for each of the scans used to produce Fig.s 3.5,3.7,3.10 are represented in Fig. 3.4a while their pixel size is represented in Fig. 3.4b. In the case of Fig. 3.4a, some of these annotations lie within the middle-to-upper area of their technique's domain which is mainly due to the presence of overhead slowing down their acquisition. Also, the FFP scan performed on the limpet tooth (sample 2, Fig. 3.7b) appears as an outlier because of the high degree of overlap and longer exposure times chosen to perform it together with the smaller pixel size aimed at, all factors reducing the accessible FOV per unit time. On the other hand the image pixel sizes annotated in Fig. 3.4b mostly fall around the expected values generated with the experimental parameters chosen to be representative for each technique. The small discrepancies are simply due to the difference between the geometries and parameters used to perform each of the experiments presented and the general ones considered to produce Fig. 3.4.

It can be noted that for all samples a first technique – PBH or STXM – was used as a means to rapidly produce a wide FOV and low resolution image to be used throughout the experiment to identify specific regions of interest, while a second technique – NFP or FFP – was exploited to get higher quality information on such regions with submicrometric resolution. This time-efficient approach is made possible by the flexibility of the experimental protocol implemented and demonstrated in this chapter. This can be applied to most setups used for coherent X-ray imaging experiments offering increased flexibility in the selection of several parameters, chiefly the size of the imaged area and

the sought resolving power. Any experiment involving wide specimens featuring structures at different scales or designed to retrieve a variety of low and high resolution images can benefit from it. The extension of its applicability was discussed and some examples of its implementation were shown within experiments for which low resolution images of whole samples have been produced in order to rapidly identify smaller regions of interest on which to run more time-consuming scans revealing high resolution features. Given the fact that ptychographic scans are often run at hundreds or even thousands of different sample orientations to produce datasets suited for tomographic analysis, the collection of initial wide field 2D images is even more crucial to pin down the location and extent of a region of interest (ROI) making its imaging in 3D more time-efficient. Selecting the most suited technique for each situation together with fine-tuning the available parameters also helps in making an optimal use of beam time as well as decreasing dose on the sample, thus preventing potential radiation damage.

The proposed experimental protocol is routinely applicable at both soft and hard X-rays beamlines involved in propagation-based imaging experiments both in 2D and 3D.

Chapter 4

Ptychography for the characterisation of wavefronts at FELs

In Chapter 3, results from experiments aimed at the characterisation of unknown specimens are shown. This is the most widespread application of ptychography in any of its forms, i.e. the use of a relatively defined beam to retrieve the transmission function of an extended specimen. Nonetheless, as it is discussed in Chapter 2, the most advanced amongst ptychographic phase retrieval algorithms are able to effectively retrieve a specimen's transmission function together with the partially coherent illumination function making up the probe. This allows to reconstruct objects even when there is only relatively limited information on the probe or when its quality is far from ideal, e.g. in the case of partial coherence of the X-ray beam or whenever variations of illumination occur during a ptychographic scan. But this feature even makes possible some experiments with a completely different goal, namely the retrieval of the illumination function in the presence of a relatively well-known specimen or test pattern. Ptychography is in fact also used to characterise X-ray beams (Kewish et al., 2010; Schropp et al., 2010; Takahashi et al., 2011; Hönig et al., 2011; Vila-Comamala et al., 2011), especially for those applications which require or benefit from a high-resolution knowledge of the wavefront, which more often occurs at high-brilliance X-ray sources such as storage rings and XFELs.

The characterisation of the wavefront of an X-ray beam using ptychography allows to characterise the focusing optics while in operation conditions. In particular, optics-induced aberrations can be identified which could adversely affect several experiments. Then the responsible optical elements can be corrected or replaced or, more easily the case, the recovered wavefront can be propagated both upstream and downstream in order to find a plane in which the observed aberrations are minimised and hence at

which to perform experiments. The reduction of the aberrations by selecting such a plane is particularly relevant in the case of experiments carried out at high power density or with small focal spot size, both conditions under which even small aberrations can have strongly detrimental effects. Furthermore, the recovery of the wavefront is useful whenever an accurate initial estimate of the illumination is needed: in the case of single particle imaging (SPI) or flash X-ray imaging (FXI) experiments, for example, starting the iterative phase retrieval algorithms from a credible illumination function may positively affect their computational cost and efficiency. Similarly, characterising shot-to-shot fluctuations at pulsed sources further contributes to decouple the effects of varying illuminations from those of the change in orientation or even morphology of the illuminated particles.

It is in particular with the latter goal in mind that the experiments introduced in this chapter have been carried out at different XFEL sources. These in fact do not only contribute to the development of quick and reliable beam diagnostics techniques but also provide insightful knowledge on X-ray beams as one of the parameters affecting flash X-ray experiments aimed at the retrieval of the 3D structure of isolated particles, ultimately with atomic diffraction-limited resolution.

The characterisation of the X-ray beam generated at XFELs can be achieved to a different degree through several techniques, some of which are briefly listed here.

Shack-Hartmann wavefront sensors (WFS) are CCD cameras combined with pinhole arrays and are often used to characterise local out-of-focus wavefront tilts (Keitel et al., 2016). This is an indirect method for beam diagnostics and is ineffective close to focus.

Another method routinely applied at hard X-ray FELs is that of ablative imprints (Chalupsky et al., 2011). In this approach the high-brilliance X-ray beam is shone onto a target material and the crater produced by ablation is then examined through atomic-force microscopy (AFM) returning information about the general spatial properties of the beam, such as size and shape. Though widespread, this offline technique is rather time-consuming as several craters need to be produced and analysed in order to gather enough statistical significance making it less preferable for real-time feedback while an experiment is being carried out.

Young's double-slit experiments have been used to quantify the spatial and temporal coherence of the beam (Vartanyants et al., 2011). In this approach the beam is let through two small pinholes and the visibility of the interference fringes is measured downstream giving an estimate of the spatial coherence length. On the other hand the contrast of the fringes as a function of their distance from the centre of the diffraction pattern returns an estimate of the temporal coherence length.

One can also use a grating interferometer to determine the radius of curvature of the wavefront and its pulse-to-pulse variations (Rutishauser et al., 2012). This approach has also been successful at locating the point source position of individual pulses both transversely to and along the beam direction under varying conditions ranging from normal operation to the more unstable process of driving the XFEL into saturation.

Another approach comes from the development of single particle imaging experiments for which spatially and temporally precise injection of each single particle into the beam is required. In this context, enough statistics have been collected from the diffraction patterns produced by test objects to notice that these effectively sample different areas of the beam and can therefore be used as a means of characterising it. For example the diffraction patterns from aerosol-dispersed polystyrene spheres normally collected during the calibration of an injector while setting up a single particle imaging experiment can be used to determine the average shape of the wavefront as well as its average intensity profile (Loh et al., 2013).

It has also been shown that coherent scattering experiments run on well-known samples can be exploited to easily locate the focus via speckles analysis (Sikorski et al., 2015). This analysis is performed on single pulses and also returns a first estimate of the focal spot size as well as pulse-to-pulse fluctuations of the focus position, size and shape.

Recently, another set of grating-based approaches have been proposed and successfully implemented at different FELs. These are able to return spatial fluence distributions (Schneider et al., 2018) as well as the local electric field (Liu et al., 2018) at the grating position. The main advantage of these methods is that they allow for in situ wavefront sensing and hence to directly characterise single FEL pulses. They are mainly limited by manufacturing issues as the resolution of the images they produce depends on the available grating.

Finally, ptychography too is used to characterise the full wavefield of XFEL beams (Schropp et al., 2013). The current approach involves first applying a ptychographic reconstruction exploiting an average illumination on a test specimen, i.e. running the phase retrieval algorithm under the assumption that the probe remains the same for all scanned positions, which is equivalent to neglecting the shot-to-shot fluctuations of the beam. Then, once a credible reconstruction of the test pattern has been obtained, the algorithm is run again searching for the individual illuminations at each scanning position, using the average wavefield obtained from the previous reconstruction as the initial estimate for all probes and without updating the estimate of the object.

An alternative novel ptychographic beam characterisation approach is presented in this chapter which stems from the multimodal decomposition outlined in Section 2.4.2. This approach aims first at obtaining the average probe directly as a combination of

several coherent modes accounting for the contribution of different pulses and then at retrieving as much information as possible from single pulses.

Three different sets of measurements took place at different beamlines in order to investigate and validate this method: one at the Atomic, Molecular and Optical (AMO) and one at the Coherent X-ray Imaging (CXI) end stations at LCLS, SLAC's hard X-ray SASE FEL, and one at the Diffraction and Projection Imaging (DiProI) beamline at FERMI, Elettra's soft X-ray and extreme ultraviolet (EUV) seeded FEL (cf Section 2.2.2). These experiments are individually discussed in Sections 4.2, 4.3 and 4.4 respectively

The sample used for all three experiments was a 200 nm thick Au test pattern (X30-30-2) deposited onto a 110 nm Si_3N_4 membrane. Fig. 4.1 shows a scanning electron microscopy (SEM) image of such test pattern, revealing the 30x30 µm^2 Siemens star on which ptychographic scans were run. Previous ptychography experiments of this kind exploited a periodic test pattern along with a scanning path illuminating homologous overlapping areas belonging to different periodic cells so as to overcome radiation damage issues caused by the high power density X-ray beam. Given the non-periodicity of the sample available for the experiments described here, this approach was not viable. Scans

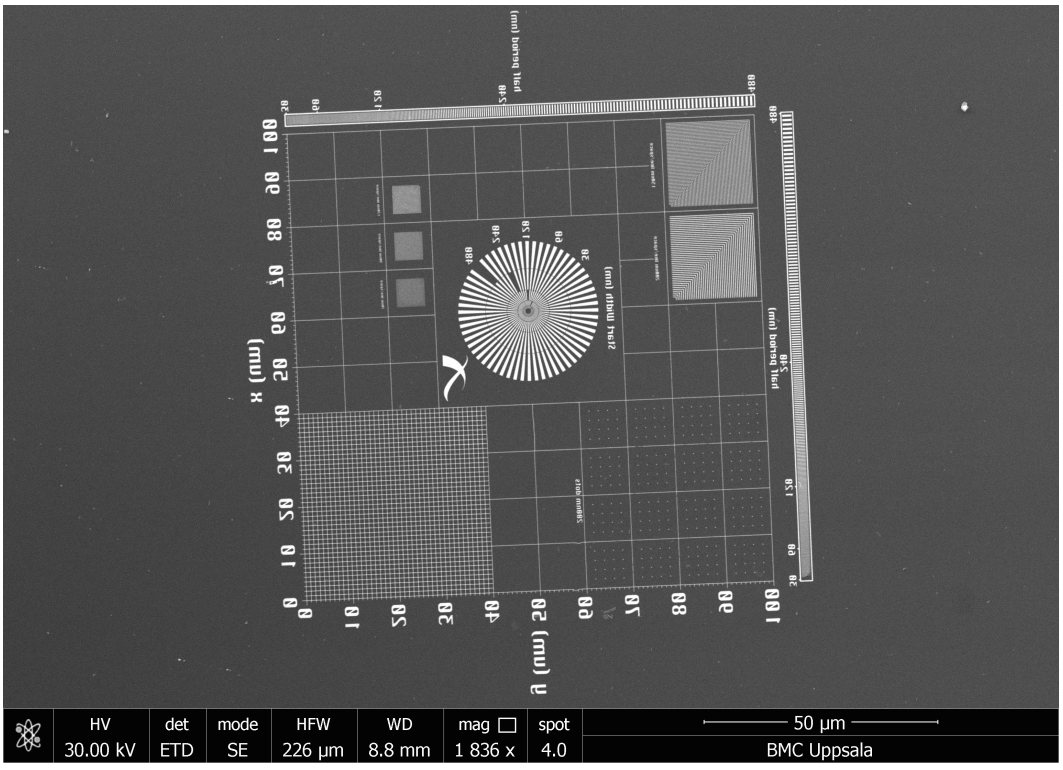

FIGURE 4.1: SEM image of gold test pattern used for the wavefront characterisation experiments performed at XFELs: the 30x30 µm^2 Siemens star used for most ptychographic scans appears at the centre of the image. This image has been produced and provided by the Molecular Biophysics group of the Department of Cell and Molecular Biology of Uppsala University.

had to be run non-destructively instead which required attenuation of the XFEL beam. In fact for wavefront characterisation experiments the beam would usually be attenuated only if necessary to prevent any detector pixel from being saturated by the direct beam which would otherwise be shadowed out by a central stop in other kinds of experiments performed at XFELs. Instead, in this case a bigger limitation has rather been the sample melting dose, typically orders of magnitude lower than detector saturation levels. Due to this large attenuation, several diffraction patterns have been collected at each scanning positions in order to compensate for the signal-to-noise ratio of a generally weakened scattering signal.

The setup used in all experiments was based on the diagram from Fig. 2.4. This geometry has been chosen to be the same as that of FXI experiments as the ultimate goal was to make the beam characterisation by ptychographic scans a routine part of such experiments, as it already is the case for the calibration and optimisation of other experimental parameters. In such a configuration only a set of two KB mirrors was used to focus the XFEL beam which would otherwise damage other diffractive optics sometimes used for imaging experiments with other sources. The experiments were carried out in the same way as that of standard ptychography experiments as described in Chapter 2, i.e. the sample was scanned onto the x-y plane ensuring the illumination at each position partly overlapped with the adjacent ones. The far-field propagated diffraction patterns were then recorded by a 2D detector located downstream along the optical axis z. Each setup operated under vacuum conditions as it would normally be necessary for full-intensity XFEL beams, especially in the case of soft X-rays and EUV for which the interaction of radiation with air is particularly strong.

Finally, for the ptychographic analysis of all datasets collected within the experiments presented in this chapter the Python package *PtyPy* was used (Enders and Thibault, 2016). In particular its mixed-state modelling algorithm has been complemented with a novel implementation of a single-shot analysis method discussed in the next section (Section 4.1).

4.1 A method based on singular-value decomposition for the analysis of single-shots datasets

In order to tackle the issue of retrieving single-shot information from ptychography measurements a novel method has been implemented within *PtyPy* directly inspired by orthogonal probe relaxation ptychography (OPRP) as proposed by Odstrcil et al. (2016). This method extends the ptychographic model to allow for every probe P_j associated to each of the N diffraction patterns I_j to vary. This is achieved by adding a singular-value

decomposition (SVD) step at the end of every iteration reducing all probes to a combination of the same modes. The remainder of the algorithm is virtually unchanged which allows for this step to be implemented in any ptychography reconstruction algorithm. For the applications presented in this chapter, such SVD step was implemented for both difference map (DM) and maximum likelihood (ML) algorithms.

Applying SVD to the complex matrix P containing all single probes P_j leads to $P = U\Sigma V^*$ where V^* denotes the Hermitian transposition of V and both U and V are unitary matrices such that $UU^* = U^*U = I$ and $V^*V = VV^* = I$ with I as the identity matrix. By multiplying P with its Hermitian transpose P^*, one gets

$$P^*P = V\Sigma^*U^*U\Sigma V^* = V(\Sigma^*\Sigma)V^* \tag{4.1}$$

with P^*P as a Hermitian matrix and $(\Sigma^*\Sigma)$ as a diagonal matrix. This is equivalent to the eigenvalue problem

$$(P^*P)V = V(\Sigma^*\Sigma) \tag{4.2}$$

so that the non-zero elements on the diagonal of Σ correspond to the square roots of the eigenvalues of P^*P. Through a truncated diagonalisation, the N eigenvalues and main k eigenvectors $\hat{V}$ can be retrieved, with $k < N$ and $\hat{V}$ denoting truncation of V. Applying this in the SVD step implementation, a set of k orthogonal modes M is generated via $M = P_n\hat{V} = U\hat{\Sigma}\hat{V}^*\hat{V} = U\hat{\Sigma}$ where P_n denotes the probe matrix P at the n-th iteration. The obtained mode matrix M is then used to generate the updated probes $P_{n+1} = M\hat{V}^* = U\hat{\Sigma}\hat{V}^*$.

It is worth pointing out that the k modes obtained with this approach are not enforced but are rather generated directly from the reconstructed probe matrix P by dimensionality reduction at every iteration.

Results from applications of this novel algorithm are discussed in the next sections.

4.2 Experiment at AMO end station

The first wavefront characterisation experiment was run at the AMO end station (Ferguson et al., 2015) at LCLS (Emma et al., 2010) with 1.25 keV soft X-rays. An attenuation to 3.42×10^{-7} of the original intensity of the 2.7 mJ pulses has been used to safely remain two orders of magnitude below the melting dose of the gold test pattern. This value also corresponds to the limit to prevent detector saturation as the full beam has been measured without any beam stop, otherwise present in other experiments in order to prevent the bright direct beam from hitting and potentially damaging the detector. Such an attenuation was achieved by using a 4.5 m long gas chamber filled with a 14.225 Torr N_2 atmosphere. The beam was then clipped by a pair of adjustable slits and focused by

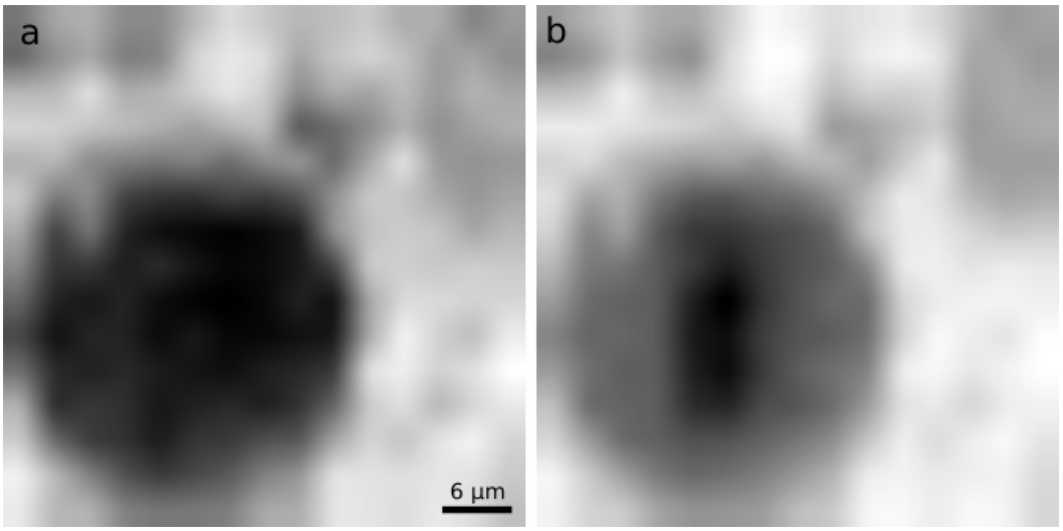

FIGURE 4.2: STXM images of the Siemens star obtained from data collected during the experiment performed at AMO, LCLS. The raster scan covered an area of 45x45 µm^2 with a step size of 3 µm. The absorption (a) and horizontal differential phase-contrast (b) images both confirm the location of the Siemens star onto the test pattern.

a pair of perpendicular KB mirrors with focal distances of 1.1 m and 1.6 m respectively. The sample was mounted in vacuum within the LAMP chamber (Ferguson et al., 2015) and at the focal position. A pn junction CCD detector with 75 µm pixels (Strüder et al., 2010) was used to record diffraction patterns 0.73 m downstream from the focal position with a 30 µm thick polyimide filter with 0.94 transmission placed just in front of it. The use of the detector was limited to an off-centred area of 192x192 pixels in order to avoid gaps in the recorded diffraction patterns which combined with the chosen geometry led to a reconstruction pixel size of 50 nm.

Real-time monitoring throughout the experiment as well as preprocessing was carried out using the open-source Python-based software tool *Hummingbird* developed and maintained by the Molecular Biophysics group of the Department of Cell and Molecular Biology of Uppsala University (Daurer et al., 2016).

STXM scans were performed at different stages of the experiment in order to accurately determine the sample position both in the x-y plane and along z and to check its integrity. An example of a 45x45 µm^2 STXM scan with a 3 µm step size is shown in Fig. 4.2 where the analysis has been conducted following the procedure described in Section 2.3: the absorption and the differential phase-contrast images both confirm the location of the Siemens star.

The ptychographic scans have all been run on a raster grid with some small known random noise added to each position in order to avoid periodicity which is known to be a potential cause of artefacts in the reconstruction, referred to as raster grid pathology

(Thibault et al., 2009). Several such scans have been run varying some of the experimental parameters: datasets have been collected with alternately high and low detector gain mode, with the sample in focus and out-of-focus and with the detector cooling heads on and off. This latter are required for the detector not to get damaged because of overheating during measurements but have been found to adversely affect the setup because of induced vibrations. A reasonable compromise found suited to address such issue during the data acquisition with the active cooling turned off has been to periodically pause the experiment to allow for the detector to cool down.

The results presented here originate from one such dataset collected in high gain mode (28 analogue-to-digital units) and with the active cooling turned off. A 5x5 μm^2 perturbed raster scan with an average step size of 0.5 µm was performed on the central region of the Siemens star while at the focal position for a total of 100 scanning points. With a 3 s dwell time, at every position about 300 single-shot diffraction patterns were collected operating the XFEL at 100 Hz whilst recording dark frames at 0.5 Hz (BYKIK mode). Dark frames, frames associated to erroneous motor positions and weak events – i.e. diffraction patterns generated by X-ray pulses with energies below 1 mJ – were discarded. To remaining frames dark correction was applied by exploiting the temporally-closest available dark frame. They were then converted to units of photons by rounding ADU-converted values to the closest integer, except for one-photon pixels counted only above the 0.75 threshold and set to zero otherwise: this constituted the single-shot dataset later used for single-shot analysis.

For the first step of the ptychographic reconstruction process an averaged dataset has been used instead. This was obtained by averaging all frames recorded at the same motor positions which – discarding the last erroneous motor position – led to a collection of 99 diffraction patterns depicted in Fig. 4.3. These frames already confirm the scan was performed on the Siemens star, as the collected diffraction patterns coincide with the Fourier transforms of areas close to its centre. The change in orientation of the diffracted signal recorded in each frame is in agreement with the raster geometry used to perform the ptychographic scan: namely the main axis of such signal lies perpendicularly to the main axis of the spokes on the sample visible at each illuminated area.

This dataset was fed into *PtyPy*'s mixed-state ptychographic reconstruction algorithm running 1000 difference map (DM) iterations and decomposing the probe P in $k = 10$ modes in order to obtain an estimate of the imaged object O within an averaged analysis. A relatively high number of modes k was chosen to take into account possible shot-to-shot fluctuations of the probe which in the averaged dataset would act as a source of decoherence, blurring out each averaged diffraction pattern. Keeping in mind Eq. 2.60

from Section 2.4.2, the mixed-state problem can be more explicitly rewritten as

$$I_j = \sum \left|\tilde{\psi}_{j,k}\right|^2 = \sum_k \left|\mathcal{F}\left[P_{j,k}(\mathbf{r})O_j(\mathbf{r} - r_j)\right]\right|^2 \tag{4.3}$$

with k incoherent modes summed up to produce each diffraction pattern I_j. Exploiting this formalism a reconstruction of the object and a first estimate of the averaged beam are generated. The absorption image of the Siemens star obtained after 1000 iterations

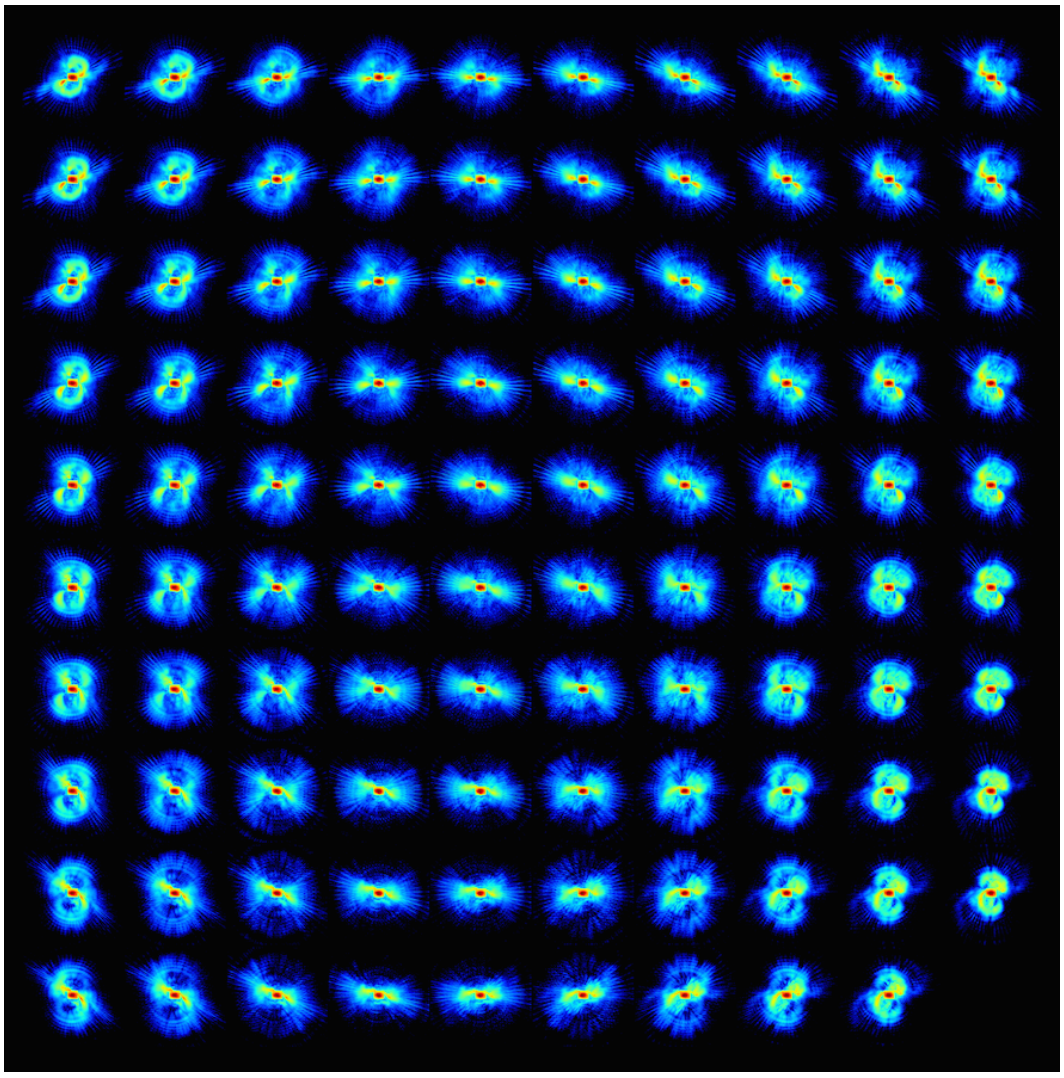

FIGURE 4.3: Averaged background-subtracted diffraction patterns collected at each position of a ptychographic 5x5 µm^2 raster scan with a step size of 0.5 µm on the Siemens star on the test pattern during the experiment performed at AMO, LCLS. Each frame has been obtained by averaging the contribution of about 300 diffraction patterns and is represented in a logarithmic scale. This dataset already confirms the scan was performed on the Siemens star, as the collected diffraction patterns coincide with the Fourier transforms of areas close to its centre. Also, the change in orientation of the diffracted signal recorded in each frame is in agreement with the raster geometry used to perform the ptychographic scan: namely the main axis of such signal lies perpendicularly to the main axis of the spokes on the sample visible at each illuminated area.

of DM algorithm is shown in Fig. 4.4b together with its SEM counterpart (Fig. 4.4a) for comparison purposes. The agreement between the two images of the object supports the reliability of the probe obtained from this averaged dataset. The $k = 10$ orthogonal modes composing such probe are shown in Fig.s 4.5a-j and are directly related to the average wavefront at the focal position produced by the XFEL. They are represented in a relative scale in order to highlight their local morphology but their contribution to the total power of the probe is also annotated for comparison purposes. Fig.s 4.5k-t show each mode after it has been propagated back to the virtual secondary source plane, i.e. the mid-point between the pair of focusing KB mirrors some 1.35 m upstream from the sample position.

While more than half of the beam power lies within a relatively well-defined elongated focus (Fig. 4.5a), it can be noted that a non-negligible fraction seems to be concentrated in confined regions towards the edges of the field-of-view (FOV) of the probe (Fig.s 4.5b,f) which currently has no straight-forward physical implication and might be the result of applying mixed-state analysis to an averaged dataset. Lower intensity modes (Fig.s 4.5i,j) pick up on diffused noise as it is revealed by a significant fraction of their power falling outside the main pupil when back-propagated (Fig.s 4.5s,t). Finally the corners of all modes accumulated no power due to the fact that one corner of the detector was mostly masked out due to unreliable readout.

Once established the reliability of the averaged dataset and having retrieved both object and probe reconstructions from it, the single-shot dataset has been analysed. Due to

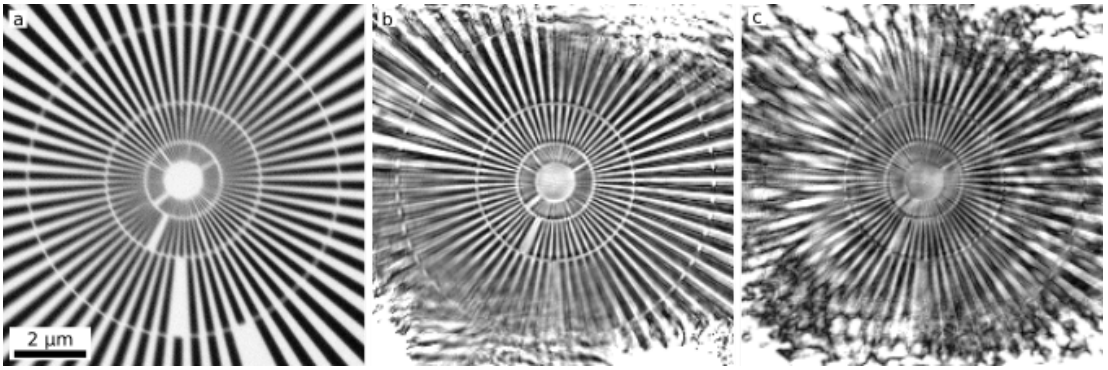

FIGURE 4.4: SEM image (a) and amplitude of ptychographic reconstructions (b,c) of same Siemens star test pattern. (a) is extracted from Fig. 4.1, (b) is obtained from the averaged dataset and (c) is obtained from the single-shots dataset. The ptychographic reconstructions (b-c) are in good agreement with the expected morphology of the Siemens star and confirm the iterative algorithms reached an adequate degree of convergence. In the reconstruction from the single-shot dataset (c) features appear less resolved than from the averaged one (b): this is mainly due to the lower statistics present in the former with respect to the latter, i.e. fewer counts. Also, in (c) brighter areas can be observed which are most likely caused by the algorithm not properly uncoupling variations in sample density from fluctuations of the beam intensity. This leads to such patchy object reconstruction rather than to probes varying more in overall photon counts.

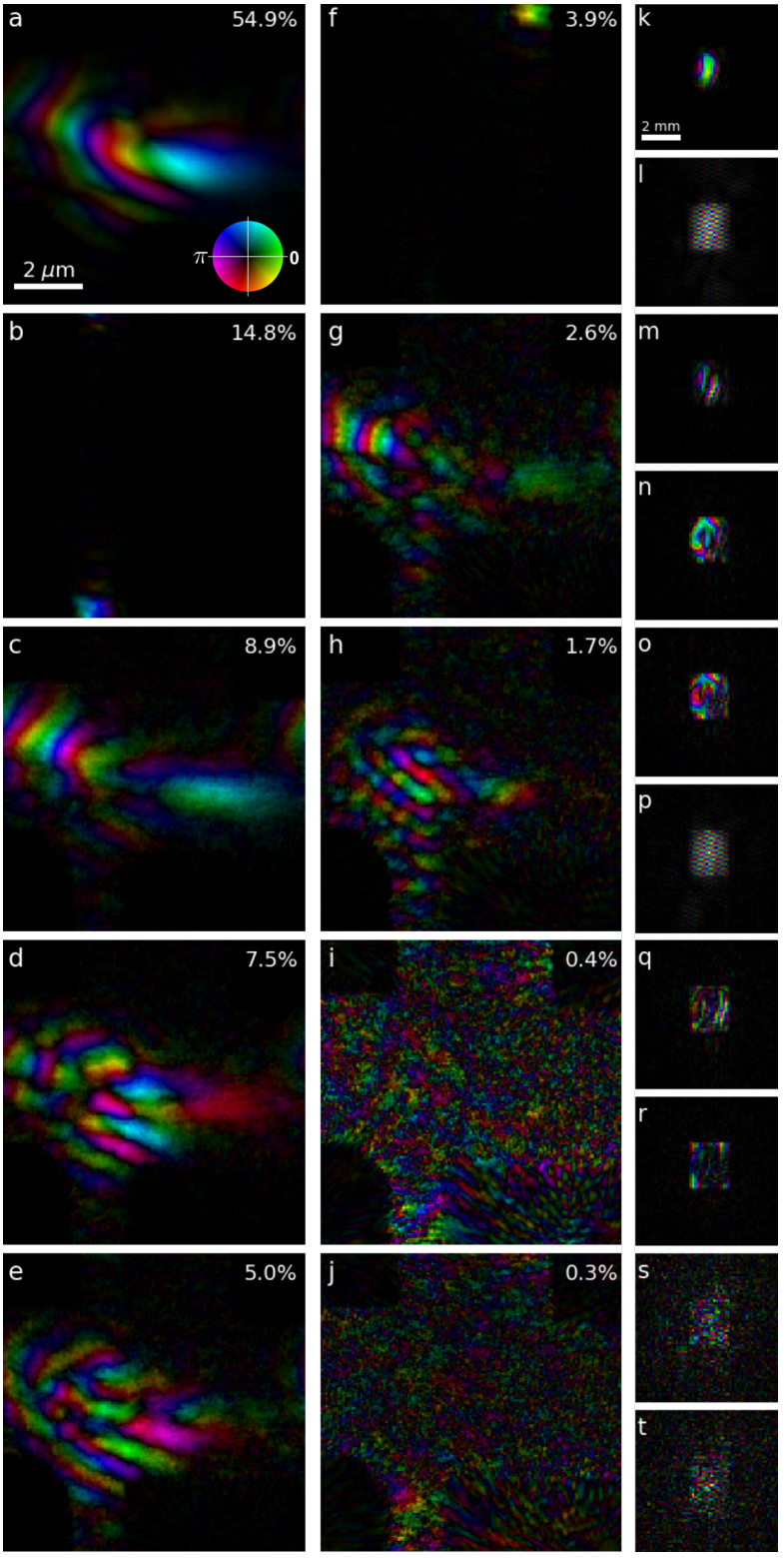

FIGURE 4.5: (a-j) Orthogonalised modes of reconstructed probe from averaged dataset. Relative intensity is annotated on top of each mode. (b) and (f) are thought to originate from incoherent contribution due to diffuse scattering from beamline components upstream the sample. (k-t) Back-propagation of such modes to the pupil plane. Amplitude is mapped to brightness and phase to hue according to the colourwheel in (a).

computational limitations a subset of diffraction frames has been produced by sampling the full range of valid frames at regular intervals in order to obtain about 10 frames per position for a total of $N = 1002$ frames. Such single-shot dataset was processed using a ML algorithm modified so to include the SVD step (cf Section 4.1) and using the probe found from the averaged dataset as an initial guess for the illumination function. For the object, a flat array was chosen as an initial guess instead, to allow to exploit the reconstructed object as a means to assess overall convergence. Choosing to decompose the probe into $k = 10$ modes and after running the SVD algorithm for 600 iterations, an object was obtained whose absorption image is shown in Fig. 4.4c. The quality of the object reconstructed from the single-shot dataset is clearly lower than that of the one obtained from the averaged dataset (Fig. 4.4b). Although more slightly-varying diffraction frames were available at every position, their signal-to-noise ratio was significantly lower than that of the averaged frames obtained by averaging the contribution of about 300 frames per position, on account of the large attenuation employed. Low signal then negatively affected the outcome of the reconstruction. Nonetheless the main features of the object are still resolved, especially within the central 5x5 μm^2 area directly covered by the perturbed raster scan.

Fig.s 4.6a-j show the $k = 10$ modes in which SVD analysis decomposed the $N = 1002$ individually retrieved probes and Fig.s 4.6k-t show the respective modes propagated back to the virtual secondary source plane. All secondary modes (Fig.s 4.6b-j) discontinuously concentrate their power towards the top and bottom edges of the FOV of the probe – areas which accumulate little to no power in the main mode (Fig. 4.6a) – and in the central high-power region of the focus. This suggests the main mode is responsible for most of the power of the retrieved single-shot probes while the secondary modes concentrate on noise and small shot-to-shot variations. This statement is further backed up by the fact that the back-propagated secondary modes extend outside the area of the main pupil.

Four of the retrieved probes are shown in Fig.s 4.7a-d as a representative sample of the whole stack of probes P, along with their back-propagated versions (Fig.s 4.7e-h). Only small variations can be observed ($< 1\%$) which suggests a large beam stability. However fluence is known to vary more than what the reconstructed probes indicate. This can be explained by a poor uncoupling between probe and object contributions within the reconstruction algorithm which translates into the object picking up on beam intensity fluctuations rather than the probes. This also accounts for the spotted appearance of the object reconstructed from the single-shots dataset as from Fig. 4.4c. At the same time this lacking does not undermine the credibility of the morphology found for each probe which can still be considered reliable except for an intensity rescaling factor.

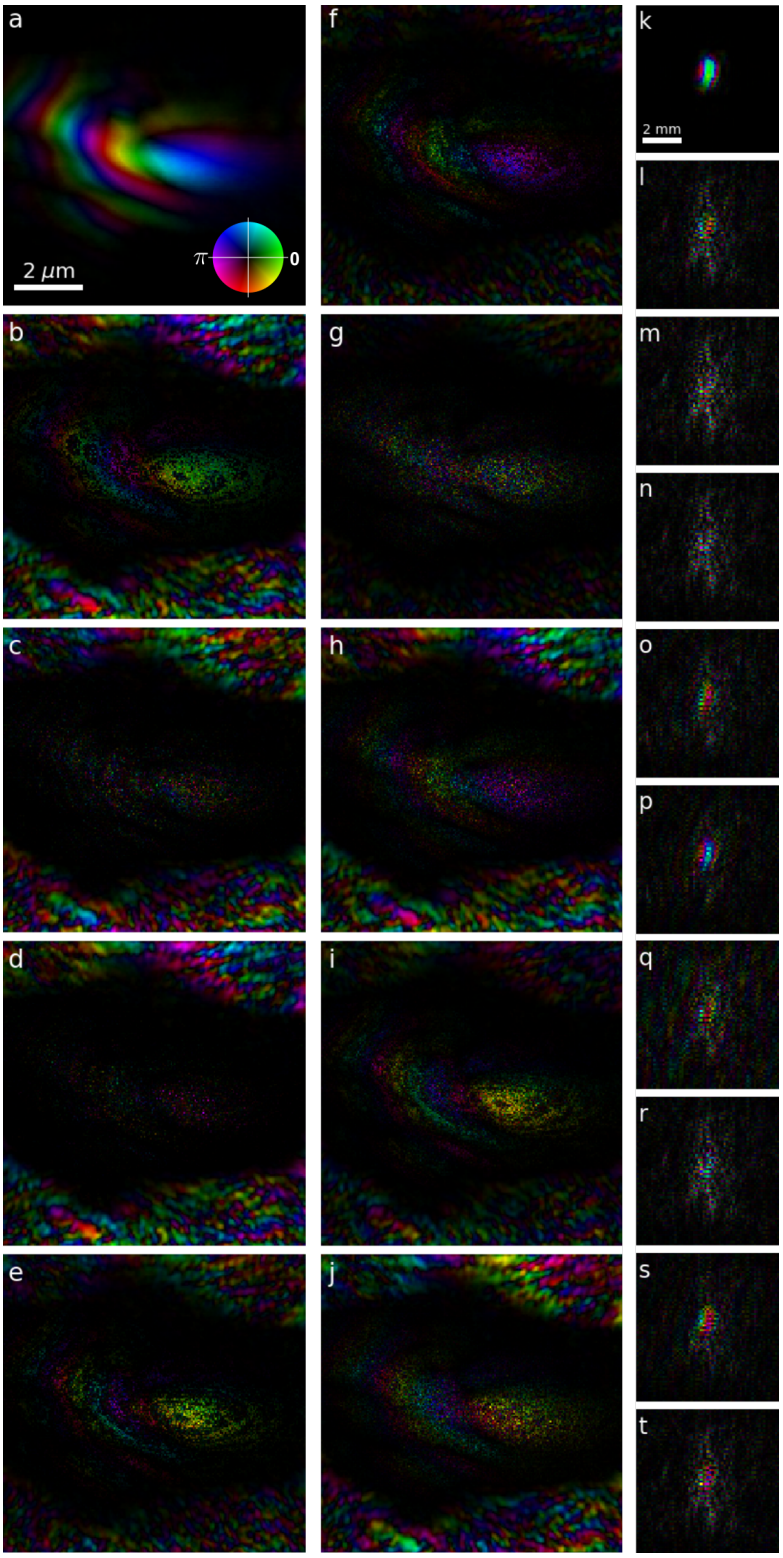

FIGURE 4.6: (a-j) $k = 10$ modes of reconstructed probes obtained via SVD from single-shots dataset. These modes were found through truncated diagonalisation aimed at solving the SVD problems (cf Section 4.1) and were not otherwise enforced as constraints onto the reconstruction algorithm: in that sense, they form the basis of the set of $N = 1002$ reconstructed probes. Beside (a), higher modes seem to address only small noise variations of the main mode. (k-t) Back-propagation of such modes to the pupil plane. Amplitude is mapped to brightness and phase to hue according to the colourwheel in (a).

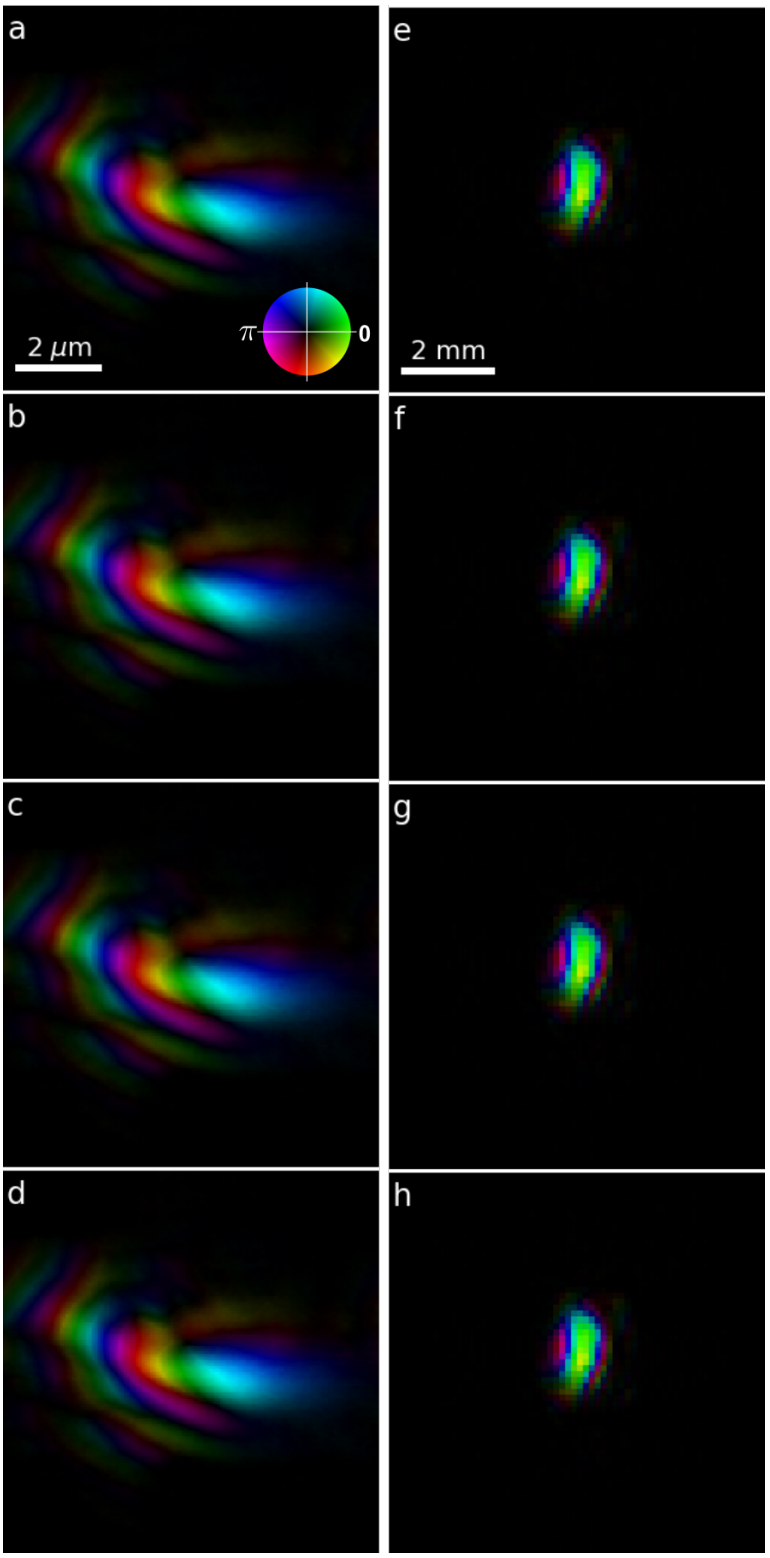

FIGURE 4.7: (a-d) 4 of the $N = 1002$ reconstructed probes from the single-shots dataset. These were chosen to be representative of the most significant variation among all probes. (e-h) Back-propagation of such probes to the pupil plane. These probes show no significant variation, neither at the sample plane nor at the pupil plane. This suggests that if any pulse-to-pulse variation occurred at all, the low statistics offered by the recorded single-pulse diffraction patterns was not sufficient for the SVD algorithm to pick up on it. Amplitude is mapped to brightness and phase to hue according to the colourwheel in (a).

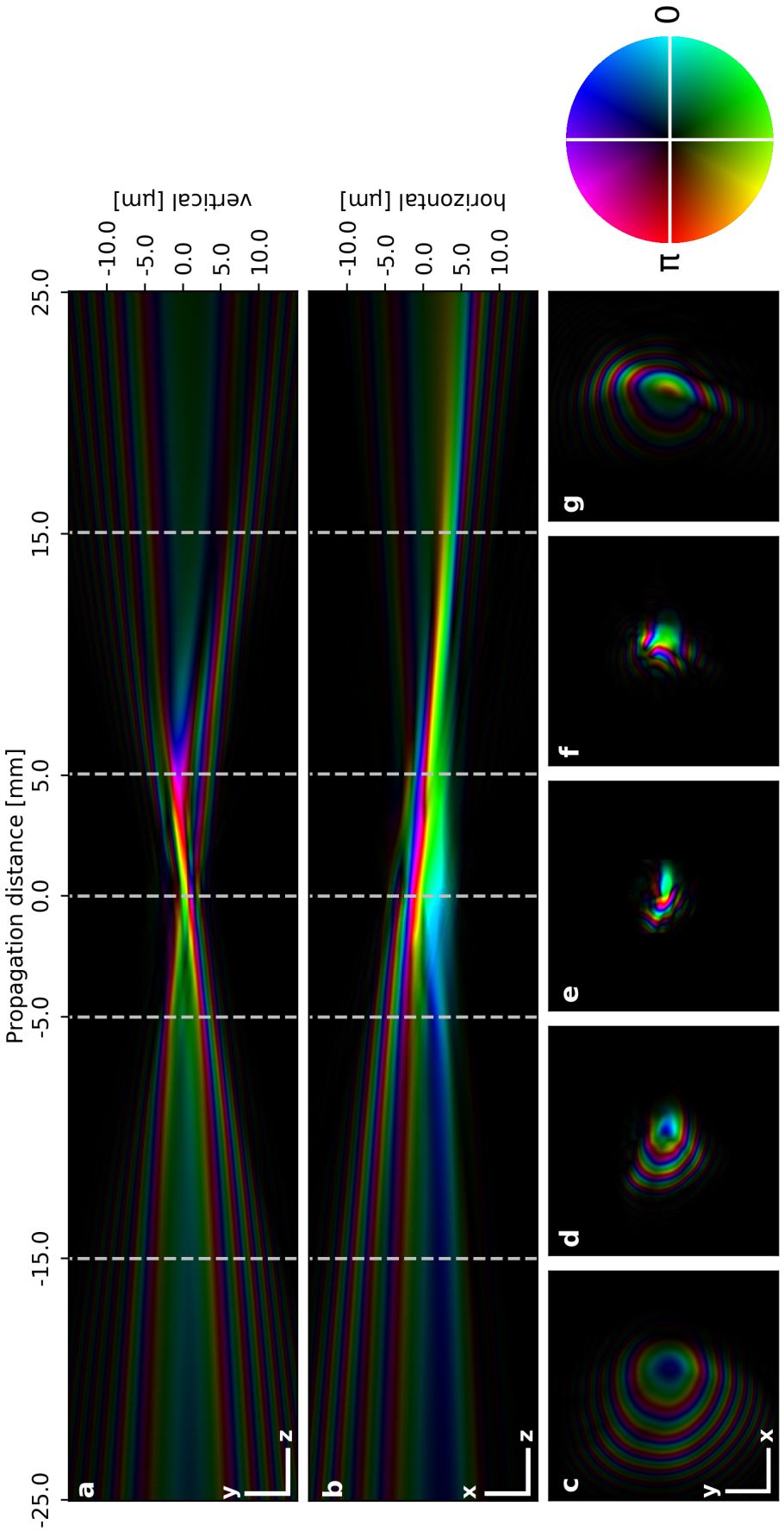

FIGURE 4.8: Figure rotated for better viewing. (a) vertical and (b) horizontal cross sections of the retrieved focused X-ray beam propagated around the focal position. Horizontal axis in units of millimetres and vertical axis in units of micrometres. A slight astigmatism can be noticed as the tightest and brightest spot is located at different positions for (a) and (b). This is often found to be the case for beams focused with KB mirrors. (c-g) beam profiles at different propagation distances as annotated in (a,b): namely (c) 15 mm and (d) 5 mm upstream from the focus, (e) at the focus and (f) 5 mm and (g) 15 mm downstream from the focus. Amplitude is mapped to brightness and phase to hue according to the colourwheel.

The probes obtained from the analysis of the single-shots dataset also strongly agree with the main probe mode from the averaged dataset which is then confirmed as a suitable representation of the wavefront of the average beam as well as of that of individual pulses. This leads to a measured focus whose size lies within the expected values of a few micrometres but is also revealed to be asymmetric, with a FWHM of around 2 µm and 1 µm in the horizontal and vertical directions respectively. Such wavefront has also been numerically propagated around the focal position as shown in Fig. 4.8, revealing how the beam propagates asymmetrically upstream and downstream due to the intrinsic astigmatism of KB mirrors. However it should be noted that the wavefront does not undergo any significant change or distortion within a 10 µm range in either direction of the focus which corresponds to the interaction region of FXI experiments hence confirming a large degree of beam stability for such experiments both temporally (shot-to-shot) and spatially (around the focal position).

4.3 Experiment at CXI end station

Another wavefront characterisation experiment has been performed at the hard X-rays CXI end station (Liang et al., 2015) at LCLS on the same test pattern and with a geometry based on the same concept as the one outlined in Section 4.2 (cf Fig. 2.4). The most advanced FXI setup has been used aiming at a focal spot size of 100 nm which made the whole experimental procedure particularly challenging.

At first an energy of around 7 keV was aimed at which would have required an attenuation of the 1 mJ pulse intensity to about 10^{-10} of the original value to prevent radiation damage on the sample, i.e. about 5 orders of magnitude lower than the detector saturation limit for this energy. Four solid Ge attenuators with a thickness of 290 µm each were available at the beamline for that purpose. However they were found unsuited to withstand the radiation damage induced by the beam at such energy and therefore the experimental plan had to be changed on site by switching to an energy of 9.5 keV.

A pair of KB mirrors with focal lengths of 0.9 m and 0.5 m respectively have been used as focusing optics throughout the experiment. The X-ray camera detecting system was a Cornell-SLAC pixel array detector (CSPAD) with a non-square tiling made up of 64 185x194-pixel application-specific integrated circuits (ASIC) covering an area of around 17x17 cm^2 for a total of 2.3 megapixels, 110 µm each (Hart et al., 2012). The detector was positioned 2.4 m downstream from the focal position.

Perturbed raster scans were performed at different sample positions both on the x-y plane and along z, mainly aimed at precisely locating the beam onto the sample and assessing its size. Data from a ptychographic scan some 5 µm off the centre of the

Siemens star were collected within a 20x20-point perturbed raster scan with 100 nm step size. Such scan was carried out with a beam energy of 9.5 keV and as close as possible to the focal position along z. At every scanning position 480 diffraction patterns were recorded, each generated from a single X-ray pulse. Fig. 4.9 shows a 10x10 downsampled set of the 20x20 frames of the averaged dataset obtained by averaging all valid frames collected at each position, according to the same principle as that used for the averaged analysis of the data collected at AMO (cf Fig. 4.3). Unlike the averaged dataset from AMO, the averaged dataset from CXI did not allow to easily assess on which area of the test pattern the ptychographic scan was performed and no strikingly recognisable feature could be identified.

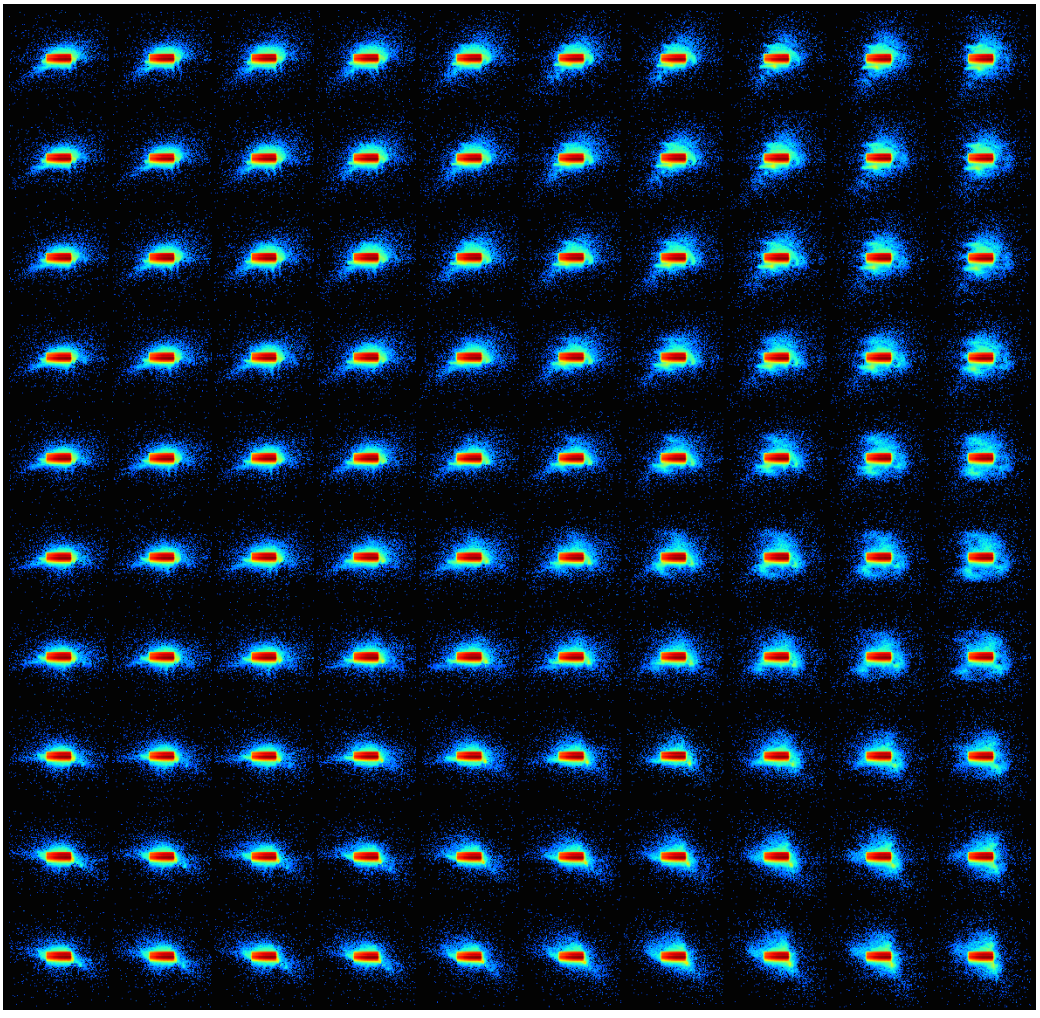

FIGURE 4.9: Averaged background-subtracted diffraction patterns collected at one every four positions of a ptychographic 2x2 μm^2 raster scan with a step size of 100 nm on the test pattern during the experiment performed at CXI, LCLS. Each frame has been obtained by averaging the contribution of 480 diffraction patterns and is represented in a logarithmic scale. Unlike Fig. 4.3, in the case of this dataset it is not trivial to estimate on which area of the test pattern the ptychographic scan was performed and no strikingly recognisable feature could be identified.

Given the used geometry a reconstruction pixel size of 15.5 nm was expected out of ptychographic analysis of this dataset, with raw frames cropped down to 184x184 pixels. Similarly to AMO, STXM analysis was carried out first in order to assess sample position, here exploiting a dataset from a ptychographic scan. This produced absorption- and phase-contrast images which are both represented in Fig. 4.10 and hinted at the fact that possibly an area of the Siemens star including only the outer part of two spokes was illuminated. This and following scans did not produce any more convincing results in terms of object convergence, let alone probe's, both from STXM and ptychographic analysis. This is most likely due to the use of a very tight focus which prevented a significantly large and well-characterised area of the sample from being unambiguously imaged. The small step sizes required to ensure large enough an overlap between scanning positions are in fact close to the precision of the translation stages which are unavoidably affected by vibrations effects and thermal drifts. Finally several attenuation-related issues have been encountered during the experiment which negatively affected the beam delivered to the sample and made measurements particularly challenging.

Via SEM analysis, no radiation damage has been observed on the sample after the experiment at CXI, suggesting that any issue encountered had to do with the positioning system and the X-ray beam rather than the dose delivered onto the sample by the highly collimated beam – though attenuated.

4.4 Experiment at DiProI end station

Another set of measurements have been collected at the DiProI beamline (Pedersoli et al., 2011; Capotondi et al., 2015) at FERMI (Allaria et al., 2015). The experiment has been performed on the usual gold test pattern at an energy of 83 eV equivalent to

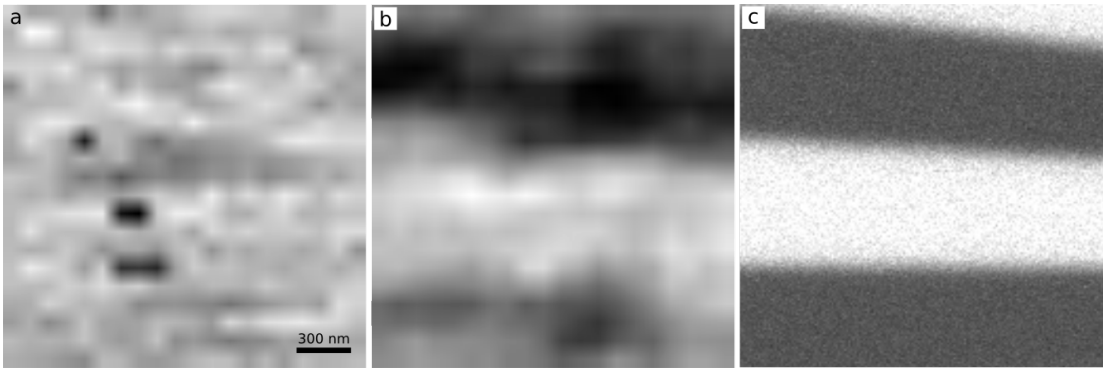

FIGURE 4.10: STXM images obtained from data partly shown in Fig. 4.9. The absorption image (a) is rather unhelpful in determining the beam location onto the test pattern, whilst the vertical differential phase-contrast image (b) suggests the scan was performed towards the outer spokes of the Siemens star. This is apparent by comparing it with the SEM image of such an outer region, as in (c), though no further conclusion could be drawn.

a wavelength of 15 nm and hence lying in the EUV regime. At this energy the sample behaves as a binary object and most of the information is carried by the transmitted signal.

An attenuation to at least 10^{-4} the original intensity of the 0.1 mJ pulses generated at FERMI was needed to prevent radiation damage on the sample and was achieved using one gas and two solid attenuators: a 300 nm thick Zr attenuator and a 200 nm thick Al attenuator have been combined with a 6 m long gas chamber filled with $2.8 \cdot 10^{-2}$ mbar of N_2.

A set of two bendable KB mirrors was used with a focal length of 1.75 m for the vertical mirror and 1.2 m for the horizontal one. These focused the beam to a focal spot size of around 4x5 µm^2 at the sample position. A PI-MTE:2048B in-vacuum CCD camera with 2048x2048 pixels 13.5 µm each has been positioned 150 mm downstream from the sample. Only the information collected by the central 1000x1000 pixels has been recorded to decrease readout time to 2 s. Unlike previous experiments, where readout frequency at least matched the pulse frequency of the FEL ensuring diffraction patterns generated by individual pulses could be recorded separately, in this case the fast shutter had to be used for only one pulse to contribute to each detector reading. Due to further overhead, FERMI's usual 10 Hz repetition rate was effectively translated into a 0.2 Hz acquisition rate, to be compared with the 100 Hz acquisition rate achieved during the experiments at LCLS. This drastic increase in the acquisition time allowed to collect only a few diffraction patterns at each scanning position – between 5 and 20. This figure can be compared to the few hundred diffraction patterns collected at each scanning position within experiments at LCLS therefore providing a larger statistical sample to be analysed.

Several ptychographic measurements have been performed scanning the sample stage over an area roughly the size of the Siemens star on the test pattern (30x30 µm^2) using spiral scans. The smallest achievable probe size of around 4x5 µm^2 has been used for most of them by keeping the sample as close to the focal plane as possible. One of such scans and its analysis are presented here. This was a 25x25 µm^2 spiral scan with 2.5 µm step size for a total of 101 points. Single-shot diffraction patterns were collected in 3 series, each recording 5 frames per scan position, for a total of 1515 frames. Each frame was corrected by removing from every pixel its respective mean dark count obtained by averaging 100 previously collected dark frames, i.e. frames recorded with the fast shutter close. Then detector counts were thresholded to a value of 0 in order to remove unphysical negative counts and finally they were converted into units of photon counts by exploiting detector specification.

The fact that FERMI is a seeded FEL implies that its pulse-to-pulse stability is significantly higher than that of SASE FELs such as LCLS. For this reason the data analysis

was supposed to be comparatively more straightforward and likely require relatively few coherent modes to model the average probe used throughout a ptychographic scan. However a wide jitter of the photon beam occurred throughout data acquisition which was later found to be caused by vibrations in the optics upstream from the experimental setup, most likely due to a pump from a nearby experiment. This made the scanning positions recorded by the sample motors unusable. Even though most of the diffraction patterns were produced by a probe-object interaction occurring within the FOV of the original scanning pattern, the beam was sometimes found to fluctuate farther away. Fig. 4.11 illustrates this issue where each set of three diffraction patterns (Fig. 4.11a-c and Fig. 4.11d-f) has been collected at the same sample stage motor positions. In particular, in the second set of diffraction patterns produced at a motor position corresponding to a region on the Siemens star (Fig. 4.11d-f) it is apparent that the beam moved enough off it to hit one of the nearby gratings (cf Fig. 4.1).

As mentioned in Section 2.4.5, different approaches exist which are able to tackle issues of position refinement within ptychographic algorithms (Guizar-Sicairos and Fienup, 2008; Maiden et al., 2012b; Beckers et al., 2013; Zhang et al., 2013; Tripathi et al., 2014).

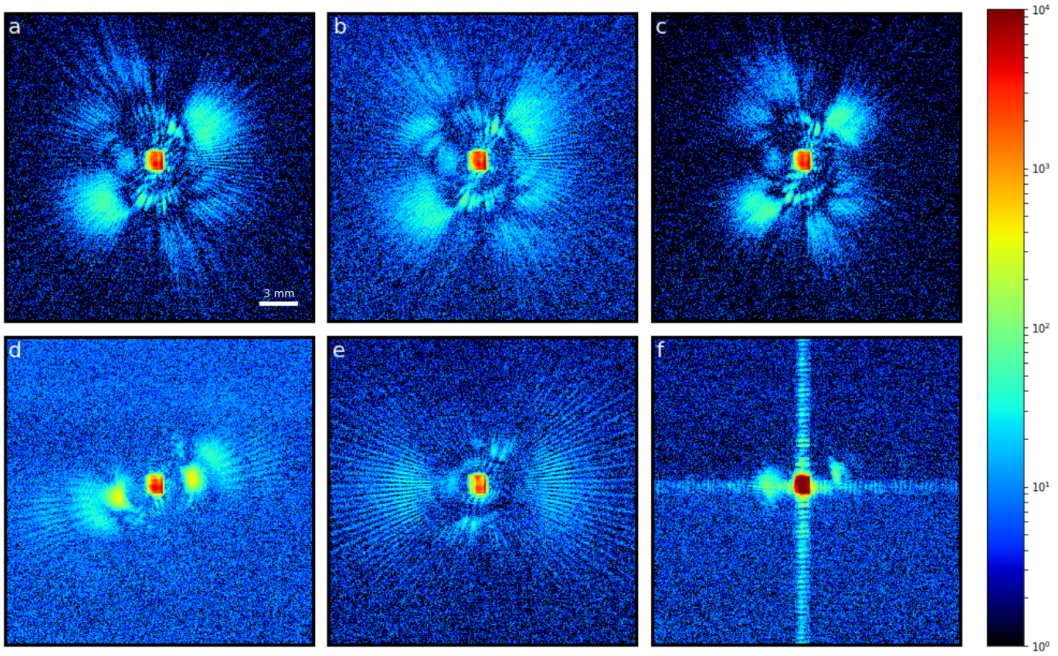

FIGURE 4.11: Individual dark-subtracted diffraction patterns collected at two motor positions (a-c and d-f respectively) of a ptychographic 25x25 µm^2 spiral scan with a step size of 2.5 µm on the Siemens star on the test pattern during the experiment performed at DiProI, FERMI. The three diffraction patterns in every row have been collected at the same sample stage motor positions and yet show discrepancies due to the pulse-to-pulse displacement of the illuminating beam onto the sample. Each frame is represented in a logarithmic scale.

However they have mostly been designed to account for minor deviations from the expected positions, typically smaller than the scanning step size. A collaborator from the Optoelectronics Research Centre (ORC) of the University of Southampton readily implemented an approach to retrieve usable sample positions in the case of the wide position errors faced within this experiment. It consisted of cross-correlating the recorded diffraction patterns with simulated ones obtained from the interaction of a simulated probe and an object modelled from the available high-resolution SEM image. This first coarse position estimate was refined iteratively via a purposely-designed ptychographic algorithm described more extensively elsewhere (Odstrčil et al., 2018). This operation was applied to the recorded motor positions as shown in Fig. 4.12a-c and produced the corrected motor positions represented in Fig. 4.12d-f. Of these, only the ones estimated with a high degree of certainty were then used for ptychographic reconstruction while the diffraction frames from the other positions were simply discarded. This led to a dataset of 937 frames, i.e. little over a third of the recorded data (578/1515) was not used.

It should be noted that this position-correction approach was only possible thanks to the in-depth characterisation of the test pattern available prior the experiment and is not expected to become the tool of choice for this kind of experiments. In fact it was only made necessary by the unforeseen circumstances in which these scans were

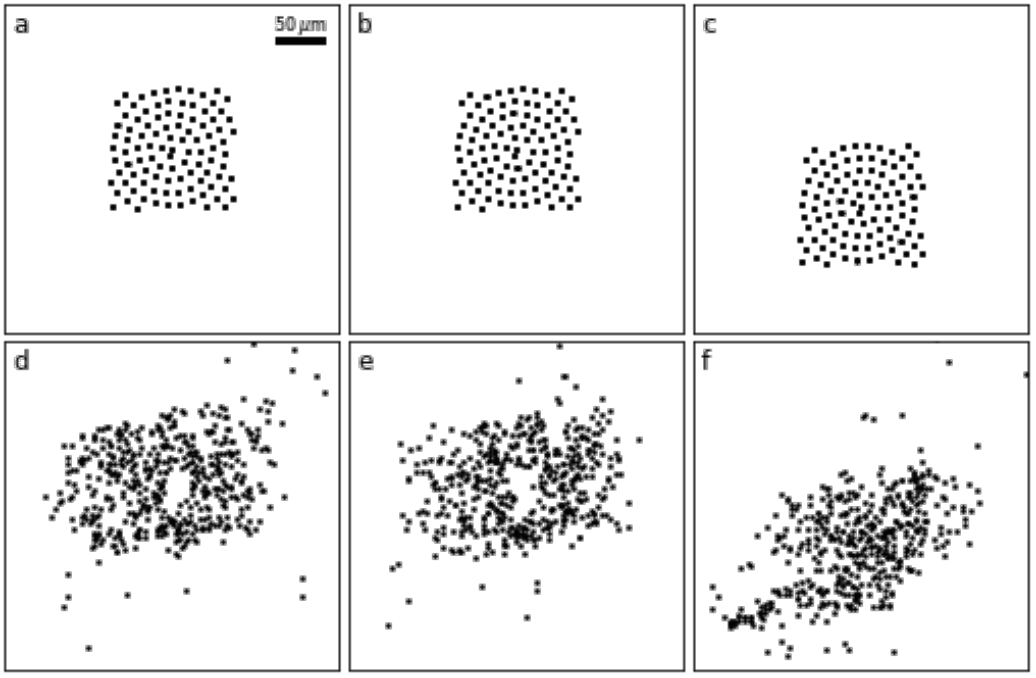

FIGURE 4.12: (a-c) Recorded x,y motor positions for three 25x25 µm^2 spiral scans with a step size of 2.5 µm performed during the experiment at DiProI, FERMI. (d-f) Actual retrieved x,y positions for scans from (a-c) respectively. Position correction was carried out exploiting simulated data as well as a purposely-designed algorithm described in details by Odstrčil et al. (2018).

carried out which do not fall into the standard operation conditions of FERMI nor other FELs. Furthermore the application of this approach also hindered any beam-pointing information that could be retrieved from the position-corrected dataset as electron bunch effects, optics effects and position corrections could hardly be uncoupled as causes of any further movement of the probe which could be found by single-shot analysis. Beside this, there is no reason to question the credibility of any other information retrieved on the probes, such as morphology and relative power distribution.

After finding the corrected positions for the collected frames, ptychographic analysis could be carried out. All of the 937 valid frames were binned by a factor of 2, down to a size of 512x512 pixels in order to decrease computational cost. The same single-shot ptychographic algorithms used for the data collected at LCLS were applied on this dataset, including the SVD step detailed in Section 4.1. Given the used geometry and detector specifications the achieved reconstruction pixel size was 162 nm. Starting from a robust initial guess for the illumination function and an empty object, 200 iterations of DM were run, followed by 800 of ML refinement, both exploiting $k = 10$ modes to decompose the full retrieved probe matrix P. This led to the retrieval of the object transmission function whose absolute value is represented in Fig. 4.13b to be compared with the SEM image of the same region in Fig. 4.13a. The agreement between the SEM image and the ptychographically retrieved one is apparent, even well outside the FOV of the original scanning area, still because of the wide beam jitter. This result validates the retrieved probes whose modes are represented in Fig.s 4.14a-j. These modes have also been propagated back to the virtual secondary source size plane located at the mid-point

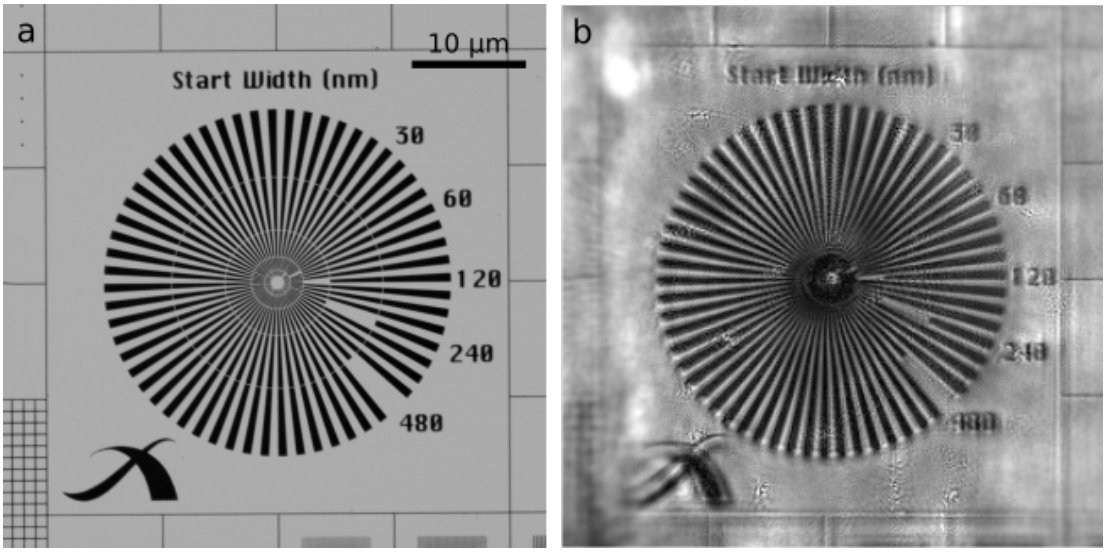

FIGURE 4.13: SEM image (a) and amplitude of ptychographic reconstruction (b) of same Siemens star test pattern. (a) is extracted from Fig. 4.1. The good agreement between the two images validates the ptychographic reconstruction and confirms the iterative algorithm reached an adequate degree of convergence.

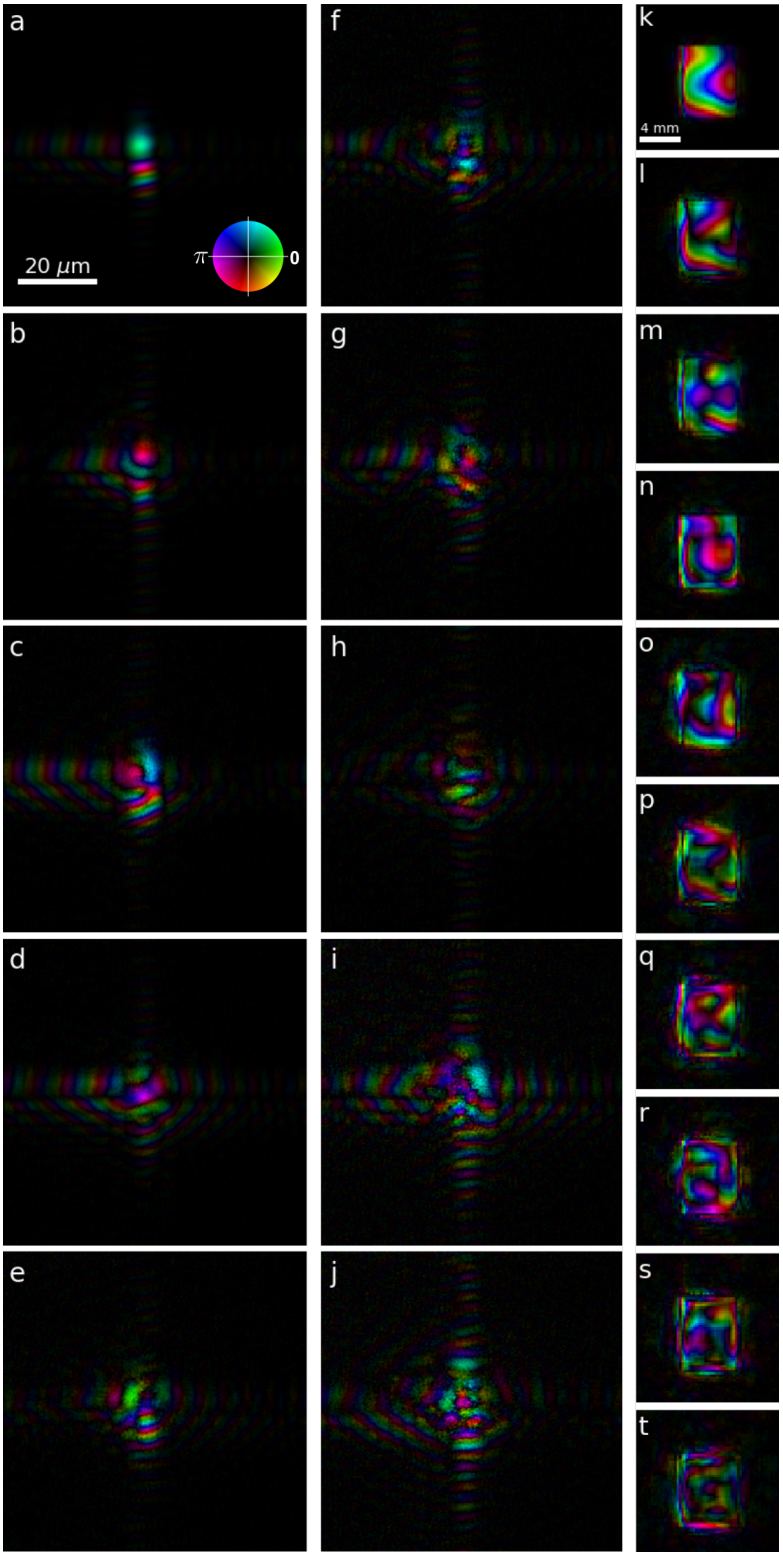

FIGURE 4.14: (a-j) $k = 10$ modes of reconstructed probes obtained via SVD. These modes were found through truncated diagonalisation aimed at solving the SVD problems (cf Section 4.1) and were not otherwise enforced as constraints onto the reconstruction algorithm: in that sense, they form the basis of the set of $N = 937$ reconstructed probes. Their diversity suggests a significant variation among the retrieved probes. (k-t) Back-propagation of such modes to the pupil plane. Amplitude is mapped to brightness and phase to hue according to the colourwheel in (a).

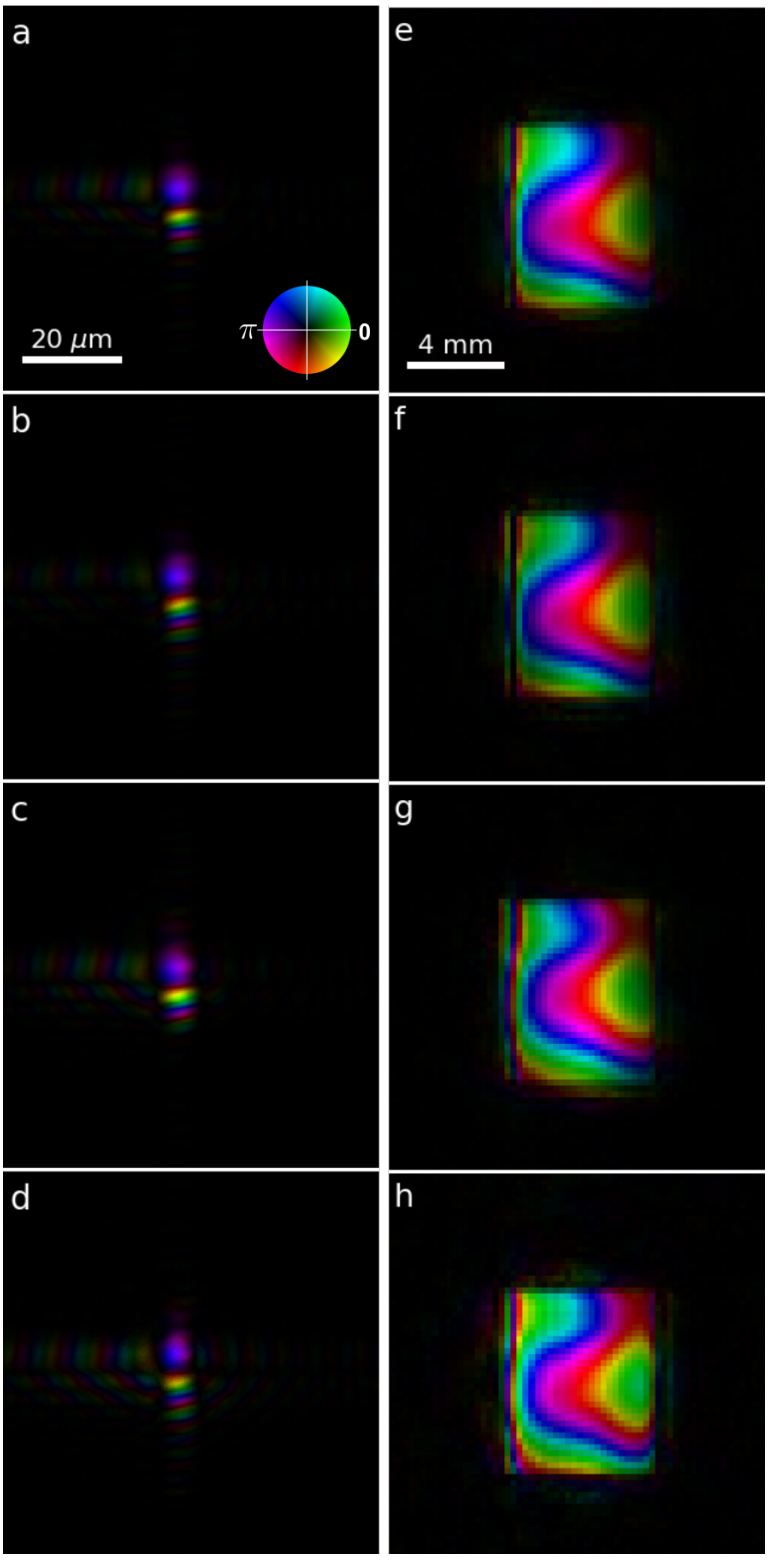

FIGURE 4.15: (a-d) 4 of the $N = 937$ reconstructed probes obtained via SVD. These were chosen to be representative of the most significant variation among all probes. (e-h) Back-propagation of such probes to the pupil plane. Significant variation can be appreciated among the retrieve probes at both the sample and the pupil planes, suggesting pulses differed not exclusively due to beam pointing instability. Amplitude is mapped to brightness and phase to hue according to the colourwheel in (a).

between the pair of KB mirrors 1.48 m upstream from the interaction plane as shown in Fig.s 4.14k-t in which only the last few modes present a significant amount of power falling outside the area of the main pupil. Four probes are shown in Fig.s 4.15a-j as a representative sample of the full stack of $N = 937$ retrieved probes. Fig.s 4.15k-t show their respective wavefronts propagated back to the virtual secondary source plane.

The retrieved probes are in good agreement with the expected elongated shape of the focus and some small shot-to-shot variation can be observed providing direct insight into FERMI's performance.

4.5 Conclusions

A novel ptychographic reconstruction method based on SVD was presented in this chapter. The method is aimed at the characterisation of single X-ray pulses and has been tested within 3 different experiments at FELs.

The one carried out at CXI did not produce any usable result due to poor and unforeseen experimental conditions, which in turn led to the poor quality of the collected data. On the other hand, both of the other experiments – carried out at AMO and FERMI – generated significant results.

In particular, the experiment at AMO proved the SVD-based ptychographic algorithm to be a viable and valid method to obtain probe and object reconstructions from a low-signal single-shot dataset. It is expected that the availability of larger computational power will allow for a larger fraction of the collected data to be analysed at the same time, increasing its redundancy and hence compensating for the low signal. In fact, low signal hinders the quality and credibility of reconstructions when only a small fraction of the collected data is fed into the algorithm, so that only a few diffraction patterns are available at each scanning position. The conclusion of the experiment at AMO is that beam stability is relatively high: if any pulse-to-pulse wavefront fluctuations occurred, they did at a length scale lower than the one to which the reconstruction algorithm is sensitive. It is expected that such sensitivity will be improved by processing a larger number of diffraction patterns for the same scanned area.

The experiment at FERMI also validated the SVD-based method for single-shot analysis based on the quality of the probe and object reconstructions obtained therein. Larger shot-to-shot variations of the wavefront have been found with respect to those retrieved for AMO, although these might be due to the unexpected jitter of the focusing optics rather than some more fundamental properties of the FEL. It should be noted that this method is robust against several sources of uncertainties over the recorded motor positions and hence suited for wavefront characterisation experiments elsewhere, as they are

often affected by vibrations and drifts – though smaller than the ones encountered here. Results obtained from the FERMI experiment have been gathered into a manuscript ready for submission to a peer-reviewed journal.

The novel SVD-based ptychographic method is primarily expected to benefit wavefront characterisation experiments at FELs. However, its application can be envisioned within other more object-oriented ptychography experiments which could also benefit from a small relaxation of the probe constraints, mainly allowing for probe variations at every position.

Chapter 5

Ptychography for the volumetric investigation of photonic nanostructures in butterfly scales

In Chapter 4 ptychography experiments have been discussed which were run on a well-known test sample, with the goal of characterising the X-ray beam interacting with it and therefore indirectly a whole X-ray imaging setup. In this chapter, experiments run on well-known X-ray imaging setups are presented which exploited ptychography to characterise samples of relatively unknown structure. This highlights the flexibility and wide range of applicability of such scanning diffractive X-ray imaging technique.

In particular, this chapter focuses on ptychographic measurements compatible with computed tomography (CT, cf Section 2.5) and performed on biological samples. These are scales, extracted from the wings of two pansy butterflies (*Junonia orithya*) of the same kind as the one shown in Section 3.3.3.

When caterpillars undergo metamorphosis into butterflies, they grow wings which are finely covered by paddle-like scales, each generated by a single cell (Ghiradella, 1994). In many butterfly species, these scales host photonic nanostructures mostly made of chitin ($(C_8H_{13}O_5N)_n$) which are responsible for the overall wing colouration through visible light interference effects. This is a common colouring mechanism which falls into the category of structural colouration, which does not require pigments and is often found in insects – mostly butterflies and beetles – and birds. Through inter- and intra-cellular processes, thousands of cells synchronise producing coloured patterns consistent within butterflies belonging to the same species. How these processes have evolved and how they are regulated by genes are both questions of interest in the field of evolutionary developmental biology and bioengineering, and wing colouration patterns make for a suitable marker to study them (Wasik et al., 2014; Prakash and Monteiro, 2018). Scales

can be divided into ground and cover scales and pave wings in an alternating fashion: the former form the bottom layer of the wing while the latter cover the topmost layer and are the ones responsible for the overall colouration. Sexual dimorphism is also present within pansy butterflies and, in this context, takes the form of a different general colouration of the wing: namely female individuals mostly grow brown ground and cover scales whereas males grow black ground scales and blue cover scales. Fig. 5.1a shows a reflected light optical microscope image of a portion of a male wing from which several blue cover scales have been removed in order to reveal the black ground scales underneath. The difference in colouration among scales is caused by differences in their 3D self-assembled nanostructures: these are all morphologically similar but show slight variations in sizes, which in turn alter their visible light interference effect. Several structures feature on each scale, such as differently spaced crossribs and ridges which grow on top of a flat substrate known as lower lamina (Ghiradella, 2010). The lower lamina is in turn connected to the rest of the wing through a stem at its narrowest end and parallel to its main plane. Variations of thickness of the lower lamina are known to be among the factors responsible for the overall scale colouration and occur within the range 100-200 nm. Fig. 5.1b shows a 20X magnification transmitted light optical micrograph of a single brown cover scale extracted from the wing of a female pansy butterfly and glued on top of a 70 µm kapton MicroLoop E^{TM}. Axial ridges are visible. Fig. 5.2 shows SEM images of the dorsal side of an isolated blue cover scale extracted from the wing of a male pansy butterfly. In Fig. 5.2, even the smaller crossribs are visible as the smaller structures connecting the axial ridges perpendicularly. On the right-hand side of both images the stem connecting the scale to the wing substrate is visible. Furthermore an area of the scale has been scratched in order to reveal the underlying lower lamina (cf Fig. 5.2b).

Neither visible light microscopy nor scanning electron microscopy allow to fully characterise all nanostructures including the lower lamina. In fact, visible light microscopy does not have high enough resolving power to return accurate measurements of the size of these structures, while SEM returns high resolution images of only the surface of a specimen on account of its relatively shallow penetration depth. SEMs rely on interaction volumes at most a few micrometres deep which prevents from running tomographic scans and limits them to produce at most 2D projections. X-rays become then suitable candidates for the volumetric investigation of butterfly scales, as they offer the necessary penetration depth combined with the potential to reach a high resolving power. Both Bragg and coherent X-ray diffraction experiments have been run on butterfly scales with the purpose of characterising the photonic nanostructures they contain (Singer et al., 2016). That concept is here explored further by running ptychographic X-ray computed tomography (PXCT) experiments aimed at the volumetric characterisation

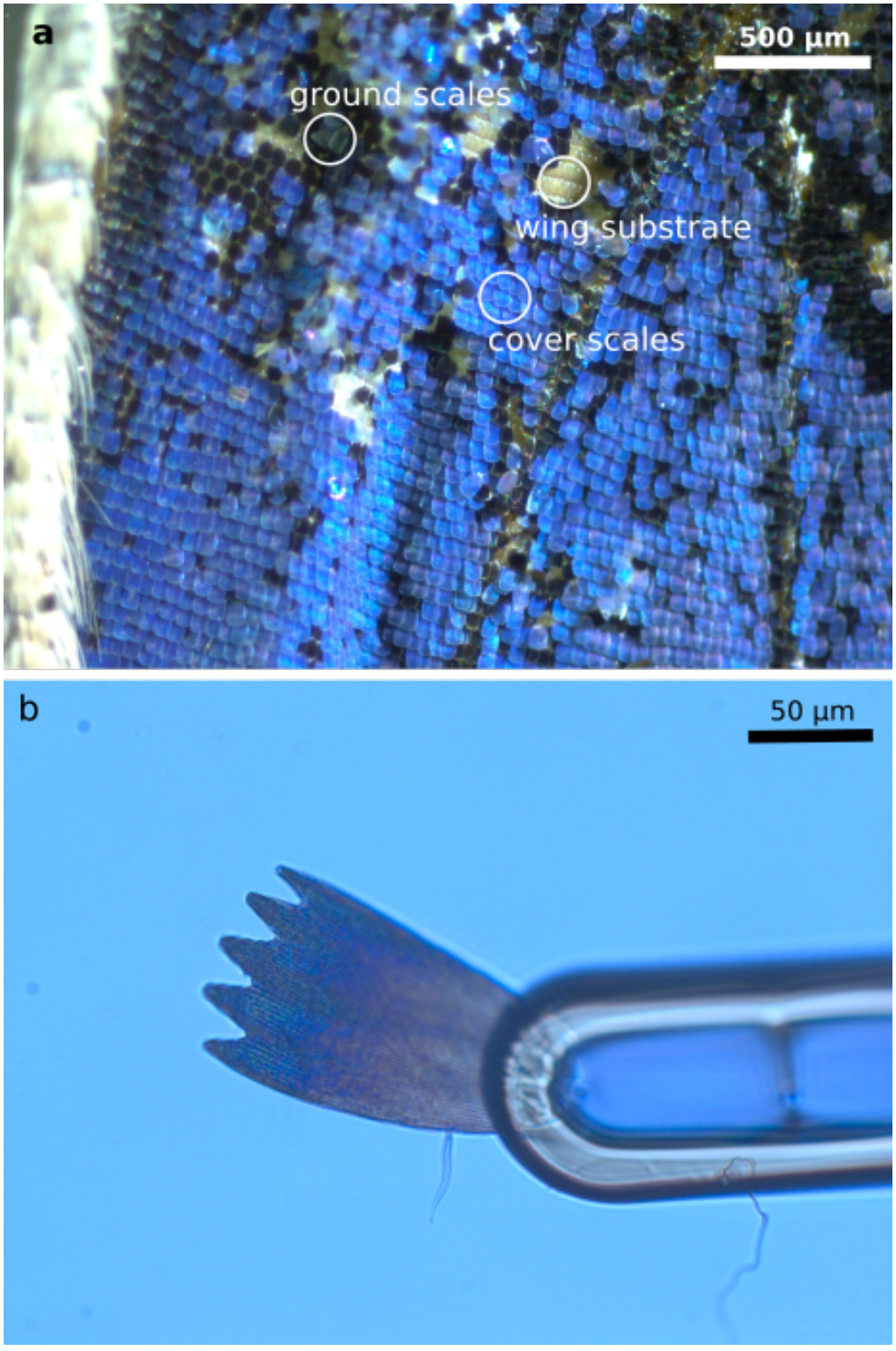

FIGURE 5.1: (a) Reflected light micrograph of a portion of the dorsal side of a wing from a male pansy butterfly. The uppermost layer is made up of blue cover scales. Areas of the wing have been scratched to reveal the underlying black ground scales and the wing substrate (appearing gold). Areas featuring each of these elements are circled and labelled in (a). (b) Transmitted light micrograph of a single brown cover scale extracted from the wing of a female pansy butterfly and mounted on a kapton MicroLoop E^{TM} holder.

of both brown cover scales from a female pansy butterfly and blue cover scales from a male.

PXCT was first demonstrated under a decade ago by Dierolf et al. (2010) at the cSAXS beamline at the Swiss Light Source (SLS) which kept leading its development for the following years (Guizar-Sicairos et al., 2011; Diaz et al., 2012; Holler et al., 2014; Guizar-Sicairos et al., 2015b; Holler et al., 2017). Due to the many technical challenges it poses, the implementation of PXCT outside cSAXS took some years to be achieved, but recently more beamlines are starting to offer it to external users (Stockmar et al., 2015a; da Silva et al., 2017a; Yu et al., 2018; Kahnt et al., 2018). In this context, one of the goals of the experiments presented in this chapter is to further contribute to the establishment and spreading of PXCT, especially to the benefit of the synchrotron light user community.

Two separate experiments are presented which have been carried out at different beamlines. Both experiments were based on a standard ptychography experimental setup, qualitatively comparable to the one presented in Chapter 3. The technique of choice was determined based on the experimental parameters available at each beamline, mainly in terms of detector specifications and range of propagation distance downstream the sample position. With these constraints in mind, a near-field ptychography experiment was run at the ID16A Nano-Imaging beamline at the European Synchrotron Radiation Facility (ESRF) and a far-field ptychography experiment was run at the I13-1 Coherence Branchline at Diamond Light Source (DLS). In particular, the near-field experiment exploited the geometry represented in Fig. 3.1b, while the far-field experiment the one represented in Fig. 3.1c.

Both ID16A and I13-1 are long beamlines and have their experimental hutches in satellite buildings located outside the main building hosting the storage ring and hence their undulator source. They were designed this way in order to increase the transverse coherence of the X-ray beams they exploit. Recalling its definition from Eq. 2.23, it can be noted that there exist two ways to increase it. One way is to reduce the source size and is achieved by reducing the gap of beam-shaping adjustable slits located at the front-end, i.e. as close as possible to the already naturally small undulator source. The slits effectively produce a secondary source of tunable size and this approach is in place at long coherent beamlines along with several other sources. The second way is to increase the distance from the source and brought to the design of such long beamlines, able to provide a high flux of highly coherent X-rays suitable for coherence imaging experiments preserving phase information.

Each experiment and its ptychographic analysis is presented in individual sections (Sections 5.1-5.2) and the tomographic analysis of the retrieved 2D projections is then presented separately in Section 5.3.

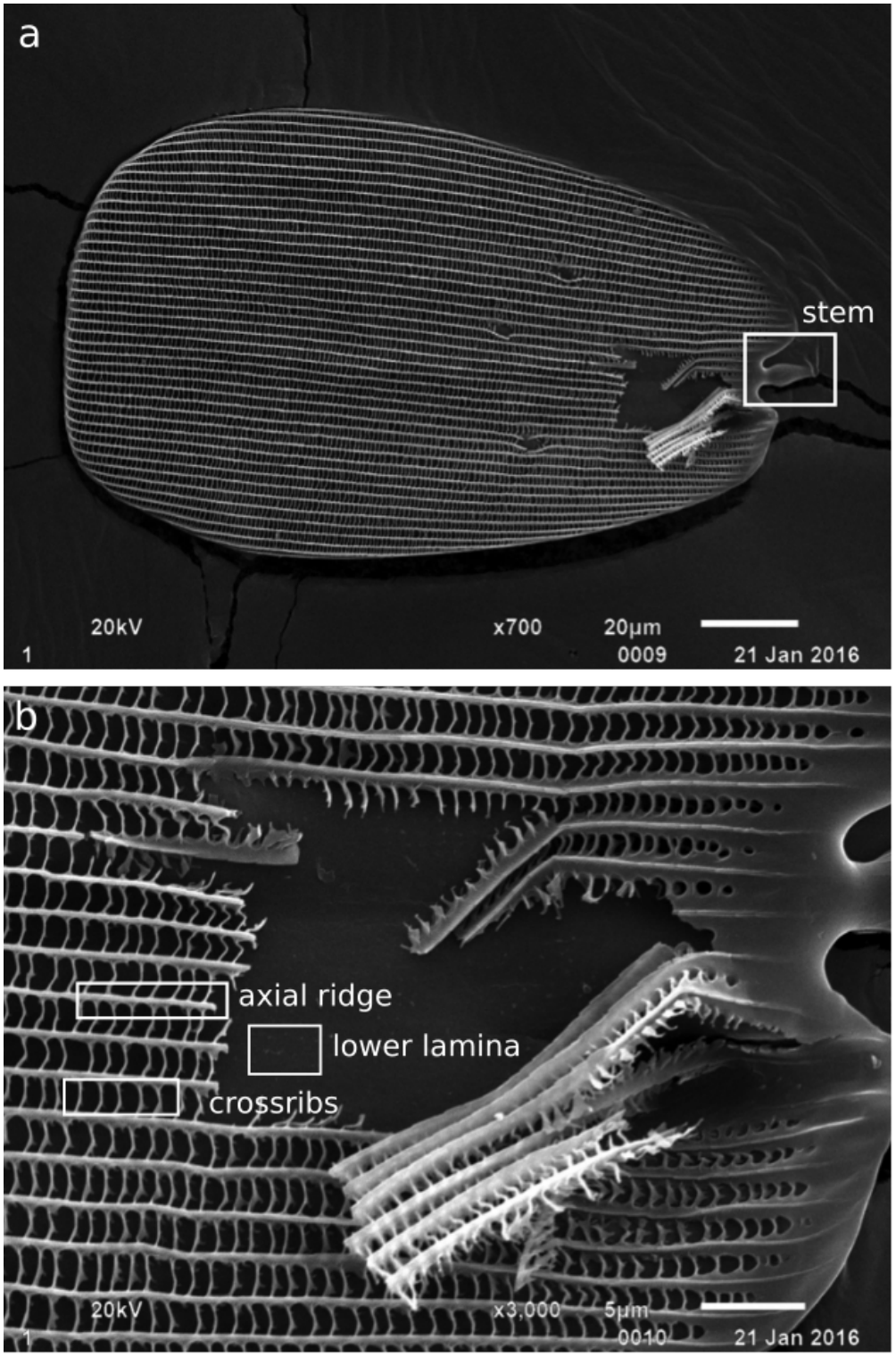

FIGURE 5.2: SEM images of the dorsal side of a blue cover scale extracted from the wing of a male pansy butterfly: (a) whole scale and (b) detail of scratched area. The wing's stem is labelled in (a). Axial ridges, crossribs and lower lamina are visible and some have been labelled in (b). SEM images have been produced and provided by the Evolutionary Developmental Biology group of the Department of Biological Sciences of the National University of Singapore.

5.1 Near-field experiment

A near-field PXCT experiment was carried out at the ID16A long (185 m) beamline (da Silva et al., 2017a) at ESRF with the aim of characterising a collection of cover scales extracted from wings of both female and male pansy butterflies. The experimental procedure and some results from ptychographic analysis are now outlined.

A 17.05 keV X-ray beam with a bandwidth of about 1% was generated by the undulator source and delivered to the experimental hutch where a set of adjustable slits formed a 550 µm aperture acting as secondary source. The beam propagating from it was then focused by graded multilayer coated KB mirrors (Morawe et al., 2015) down to a size of a few nanometres at the focal position some 100 mm downstream (da Silva et al., 2017b). A divergent beam geometry was exploited by positioning the sample downstream from the focus and adjusting its distance according to the desired reconstruction pixel size. Samples were mounted on a 3-axis high-precision translation stage as well as a rotation stage to allow for ptychography scans to be performed at different sample orientations. They were mounted inside the vacuum chamber (10^{-7} mbar) normally available at the beamline. A fast readout low noise (FReLoN) detector (Labiche et al., 2007) was positioned 1.2 m downstream from the sample position: this was an in-house developed CCD camera with 4096x4096 pixels, 15 µm each, further magnified by a 10X visible-light lens system resulting in a detector pixel size of 1.5 µm. Hardware binning by a factor of 2 was applied to reduce data size, effectively increasing the detector pixel size to 3 µm and decreasing frame size to 2048x2048 pixels. Given the divergent beam geometry, the detector pixel size was further translated into an effective pixel size in the range 27-35 nm, depending on the sample-to-detector distances used. Unlike other near-field ptychography experiments, in this case no diffuser was used as the X-ray beam delivered to the experimental hutch already showed significant diversity.

Several scales have been scanned, but the first attempts failed due to significant sample vibration. As measurements were performed in vacuum ruling out any air draft, vibrations were most likely caused by motor encoders: in fact, high-precision translation piezo stages actively maintain positioning, potentially giving rise to small vibrations which could propagate through poorly-mounted thin samples. In this case, scales around 1 µm thin were mounted free-standing on top of needles, using as little glue as possible and having as much of them as reasonable sticking out from the more strongly scattering holders – typically by 60-100 µm. After switching to more robustly glued samples, vibration effects were greatly reduced, though – at least judging from the unprocessed holograms – they seemed not to have completely disappeared.

For conciseness only one of the collected datasets is discussed in detail. This was a ptychographic CT scan performed on a cover scale from the wing of a male butterfly.

For this scan a focus-to-sample distance of 12 mm was used which resulted in a 30 nm effective pixel size and a 66 µm probe which did not fully fit the field-of-view (FOV) of the detector, corresponding to about 61 µm at the sample plane. Considering θ as the angle around the rotation axis of the rotation stage parallel to the y axis, 1301 projections were collected by varying θ in the range 0-180°. At each sample orientation a near-field ptychography scan was performed which consisted of recording 4 near-field holograms at individually-perturbed positions for each of the 4 corners of a 10x10 μm^2 area, plus one at its centre, for a total of 17 holograms per scan. A detector exposure time of 0.3 s was used throughout, making the overhead of the move-settle-measure routine the dominant factor of total acquisition time which reached 20 h. In order to correct raw frames, also 10 flats and 10 darks were collected every 200 scans, as detector readings with the empty beam and with the shutter close respectively.

Once collected, each hologram underwent dark subtraction and flat division in order to correct for hardware-induced readout artefacts by exploiting the means of the temporally-closest set of recorded flats and darks respectively. Binning by a factor of 2 was then applied to reduce computational cost leading to sets of 1024x1024-pixel frames with an effective pixel size of 60 nm. A position correction algorithm was also applied in order to get a better estimate of the sample positions as recorded motor positions have been occasionally found to be unreliable for this setup. This consisted of cross-correlating a masked version of the pre-processed holograms in order to assess displacement and led to a more reliable set of corrected positions. Pre-processed holograms and corrected positions were then fed into a mixed-state ptychography reconstruction algorithm available within the Python-based package *PtyPy* (Enders and Thibault, 2016). A 2-mode decomposition was used to model the object aimed at accounting for observed sample vibrations. 500 iterations of difference map (DM) algorithm were followed by 500 iterations of maximum likelihood (ML) refinement for every ptychographic scan.

On each reconstructed object a standard post-processing routine was performed in order to obtain a meaningful representation of the phase shift induced by the probe-object interaction (Guizar-Sicairos et al., 2011). As a first step a linear and a constant phase terms were removed from each projection equivalent to removing a phase ramp and a phase offset respectively. This was achieved exploiting areas of each projection falling outside the sample, i.e. areas for which X-rays travelled through vacuum without undergoing any phase shift. For this purpose, projection-specific masks were generated by thresholding the phase part of each reconstructed object after applying first order gaussian smoothing filters. After correcting for offset and linear ramp, phase unwrapping was carried out in order to obtain a continuous scale for the phase shift. Fig. 5.3 shows two examples of reconstructions obtained after post-processing for projections collected at two different sample orientations. Both reconstructions have been thresholded to a

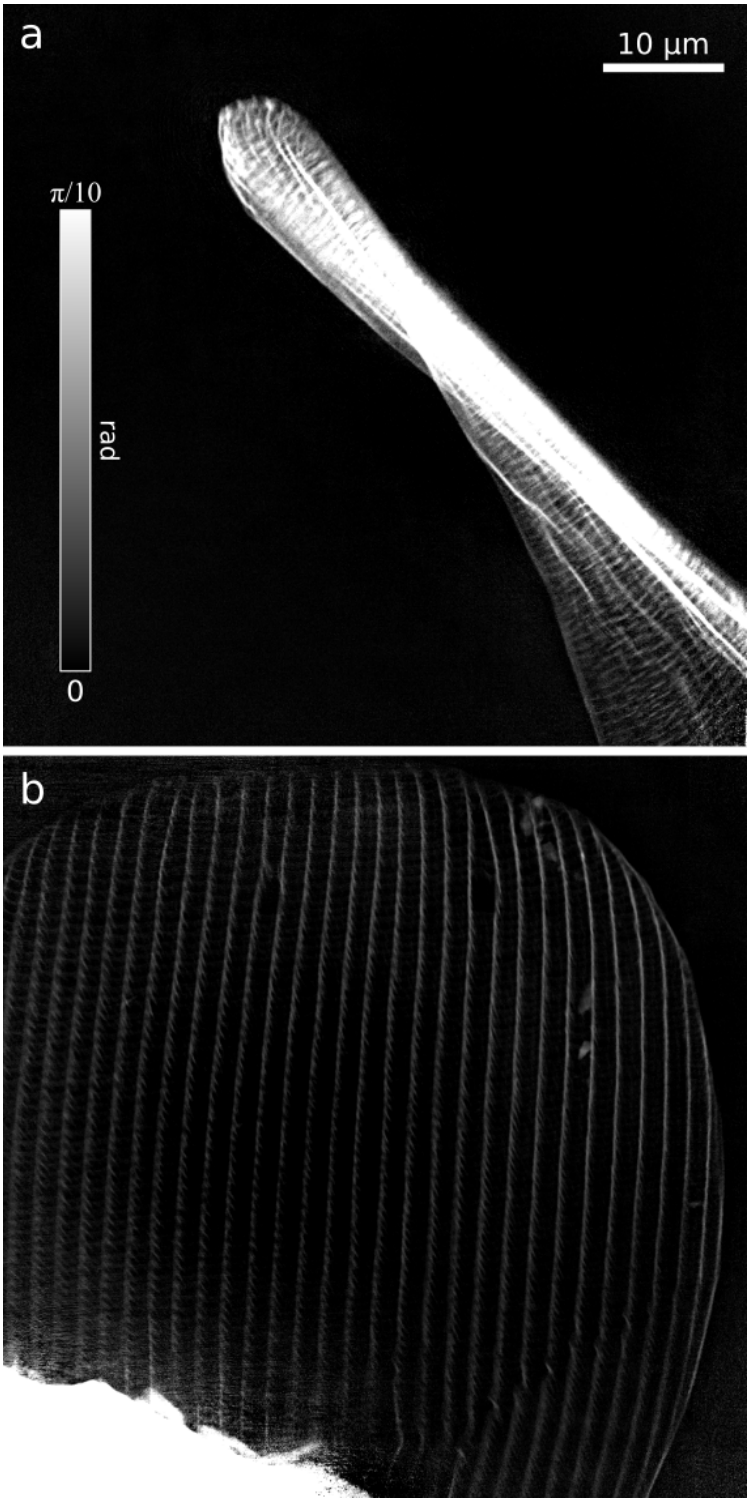

FIGURE 5.3: Phase images of whole blue cover scale extracted from the wing of a male pansy butterfly. Projections were reconstructed via near-field ptychography from scans collected at different sample orientations: (a) 54° and (b) 160°. The scale was slightly curled rather than flat, as visible from a sideways view in (a). A long-term sample drift upwards occurred during the tomographic scan, as revealed by the appearance of the strongly phase-shifting sample holder at the bottom left of (b). Axial ridges and crossribs (cf Fig. 5.2) are visible even at the widest sample orientation in (b), at which scattering is the weakest.

maximum phase shift of $\pi/10$ in order to highlight the features of the butterfly scale. This is necessary because for several projections a significant part of the tip of the needle holding the sample is visible which is much stronger a scatterer, as apparent from Fig. 5.3b. This also highlights the fact that a significant drift occurred during the long scanning procedure which at least for the vertical direction is already visible by comparing Fig. 5.3a and Fig. 5.3b.

Finally, the retrieved objects confirm the success of the ptychographic reconstruction. Weakly-scattering nanometric features were resolved, such as axial ridges and crossribs (cf Fig. 5.3b). The largest overall phase shift found for the widest sample orientations lies within the range 0.13-0.15. At 17 keV, a δ value of $1.0 \cdot 10^{-6}$ is found for the index of refraction of chitin ($(C_8H_{13}O_5N)_n$), taken from Fig. 2.3 and assuming a density of 1.37 g/cm^3. Therefore, based on Eq. 2.26 describing the relationship between phase shift φ, thickness z and δ at a given energy, an upper limit of $z = 1.2$-$1.7\,\mu m$ was found for the thickness of chitin interacting with the beam. Considering the sample tilt (ca. 45°) estimated from a perpendicular projection, this implies an overall thickness of 1.0-1.2 µm can be assigned to the largest chitin structures composing the butterfly scale, in agreement with the expected value (ca. 1 µm).

5.2 Far-field experiment

Another PXCT experiment was carried out at the I13-1 Coherence Branchline at DLS (Rau et al., 2011). A 9.7 keV X-ray beam obtained through the beamline pseudo-channel-cut crystals Si monochromator was focussed using a Fresnel focusing zone plate (FZP) with a diameter of 400 µm and an outermost zone width of 150 nm in combination with a central stop (CS) with a diameter of 40 µm and an order sorting aperture (OSA) with a diameter of 10 µm. In order to complement the information gathered from the experiment performed at ESRF on male scales, the samples used for this experiment were brown cover scales extracted from the wing of a female pansy butterfly. They were individually glued as in Fig. 5.1b and then mounted upright on the sample holder on both a 3-axis translation and a 3-axis rotation stages located some 15 mm downstream from the focal position in order to exploit a divergent beam with a diameter of 13 µm. The rotation stage provided 360° rotation around the y axis which fulfils the general requirement of tomography for a 180° rotation around an axis perpendicular to the optical axis z to be carried out. The detector EXCALIBUR was then positioned 14.6 m downstream from the sample. EXCALIBUR is the 2069x1796-pixel photon-counting beamline detector based on Medipix3 chips with 55 µm pixel size (Marchal et al., 2013). A He-filled flight tube was positioned between the sample and the detector in order to minimise scattering.

As a first step, optics alignment was carried out which consisted of aligning – or checking for the alignment of – all optical elements involved, namely the X-ray beam with respect to the adjustable slits, the monochromator, the focusing optics (CS, FZP, OSA), the sample stage and its rotation axis, the flight tube and the detector.

Then, routine beam characterisation checks followed exploiting a Siemens star test pattern in order to retrieve the wavefront at the sample position, both to validate geometry and probe size and to obtain a good initial guess for the probe for later reconstructions. The outcome of this procedure is reported in Fig.s 5.4a-b which show the phase image of the Siemens star and the dominant mode of the illumination impinging on it, respectively, both retrieved through ptychographic reconstruction. The robustness of the used algorithm is confirmed by the fact that high-resolution features are visible in the reconstruction of the object (cf Fig. 5.4a) and in good agreement with the expected morphology of the Siemens star test pattern. Two probe modes were found to be enough to account for decoherence effects thanks to the high degree of coherence available at the beamline, ensured also by operating with a relatively tight front-end slit opening. This assumption is validated by the fact that the main mode from Fig. 5.4b accounts for 96.5% of the overall power of the retrieved probe and shows a high degree of regularity and symmetry.

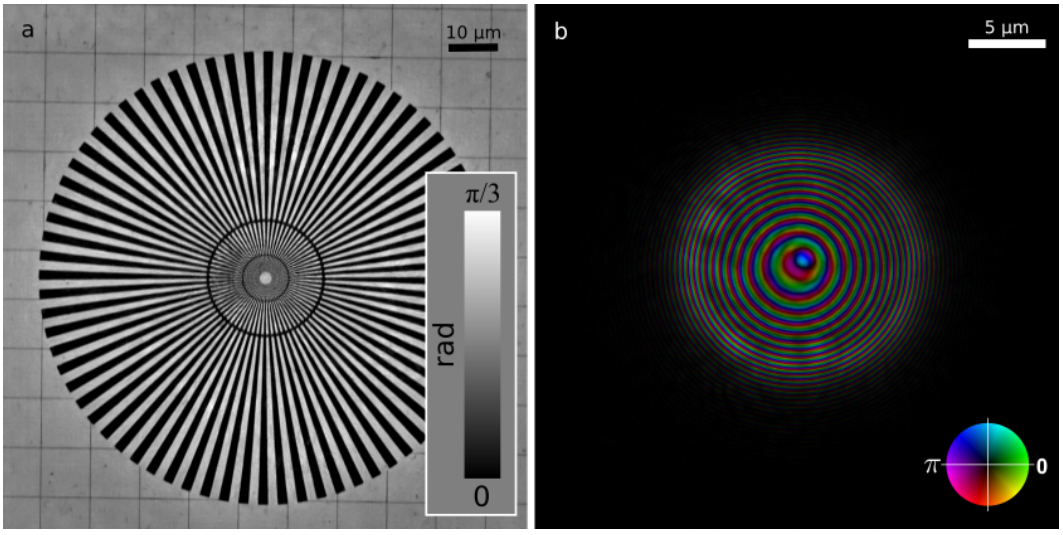

FIGURE 5.4: (a) Phase part of the object and (b) complex-valued wavefront of the dominant mode (96.5% of total power) of the probe, both obtained from a ptychographic reconstruction run on a Siemens star test pattern in order to validate and optimise the experimental setup. In (b) amplitude is mapped to brightness and phase to hue according to the colourwheel. In (a) high-resolution features towards the centre of the Siemens star test pattern are resolved, confirming the robustness of the reconstruction algorithm and the validity of the retrieved probe. As the main mode in (b) picked up most of the power, it is representative of the overall probe. Its high degree of regularity and symmetry suggests a high degree of coherence, confirming the available X-ray beam is suitable for ptychographic imaging.

After testing the experimental setup with the Siemens star, finer alignment was carried out on each mounted sample with particular care for aligning the area to be imaged in 3D with the rotation axis, which is a standard procedure whenever setting up tomographic experiments. Overview STXM scans were then performed confirming sample position and orientation as from Fig. 3.10a from Chapter 3. Finally ptychographic datasets were collected for each scale at different sample orientations.

For conciseness only one of the imaged scales is discussed and presented here, namely one has been chosen on which most measurements have been carried out and hence from which the best results were achieved. A PXCT dataset was collected by performing 6 interlaced series of ptychography scans in order to minimise risks from time limitation and potential failure of any setup component. Each series was made up of 224 scans within the angular range 0-180° with an increment of 0.8° for a total of 1344 scans. Each scan was collected in move-settle-measure mode exploiting a 10x9-point snake scan, i.e. a row-by-row raster scan inverting the order of the horizontal points at every row to reduce motor overhead. A step size of 4 µm was used to ensure a large amount of overlap among adjacent positions leading to the illumination of an overall area over 50x50 μm^2 wide featuring between 1 and 4 of the tips of the jagged apical region of the cover scale as visible in Fig. 5.5. Finally an exposure time of 0.9 s was selected as a compromise between high signal-to-noise ratio of each diffraction pattern and short scanning time leading to an overall scan duration of 55 h inclusive of pauses for optics realignment to correct for long term drifts. No radiation damage was observed throughout such long exposure confirming the dose resistance of this biogenic sample.

Ptychographic reconstruction was run on each scan in order to retrieve 2D projections at every angle of the tomographic dataset. A mixed-state approach was used with a 2-mode probe using the probe retrieved from the test pattern as an initial guess (cf Fig. 5.4b). Each diffraction pattern – already provided in units of number of photons – was cropped down to a size of 512x512 pixels which combined with the chosen geometry lead to a reconstruction pixel size of 66.3 nm. 1000 iterations of difference map (DM) algorithm were followed by another 1000 iterations of maximum likelihood (ML). The resulting objects underwent phase ramp and phase offset removal followed by phase unwrapping exploiting the same procedure used for the experiment at ESRF: namely the offset and linear ramp were determined from a masked version of the phase of the object aimed at including only areas containing air which – similarly to vacuum – was assumed to cause negligible phase shift. This led to results such those from Fig. 5.5 which shows the phase images of the scale for two different projections, i.e. at two different sample orientations.

As for the experiment at ESRF, the retrieved phase shift from the reconstructed objects was used to produce an estimate of the upper limit for the thickness z of the

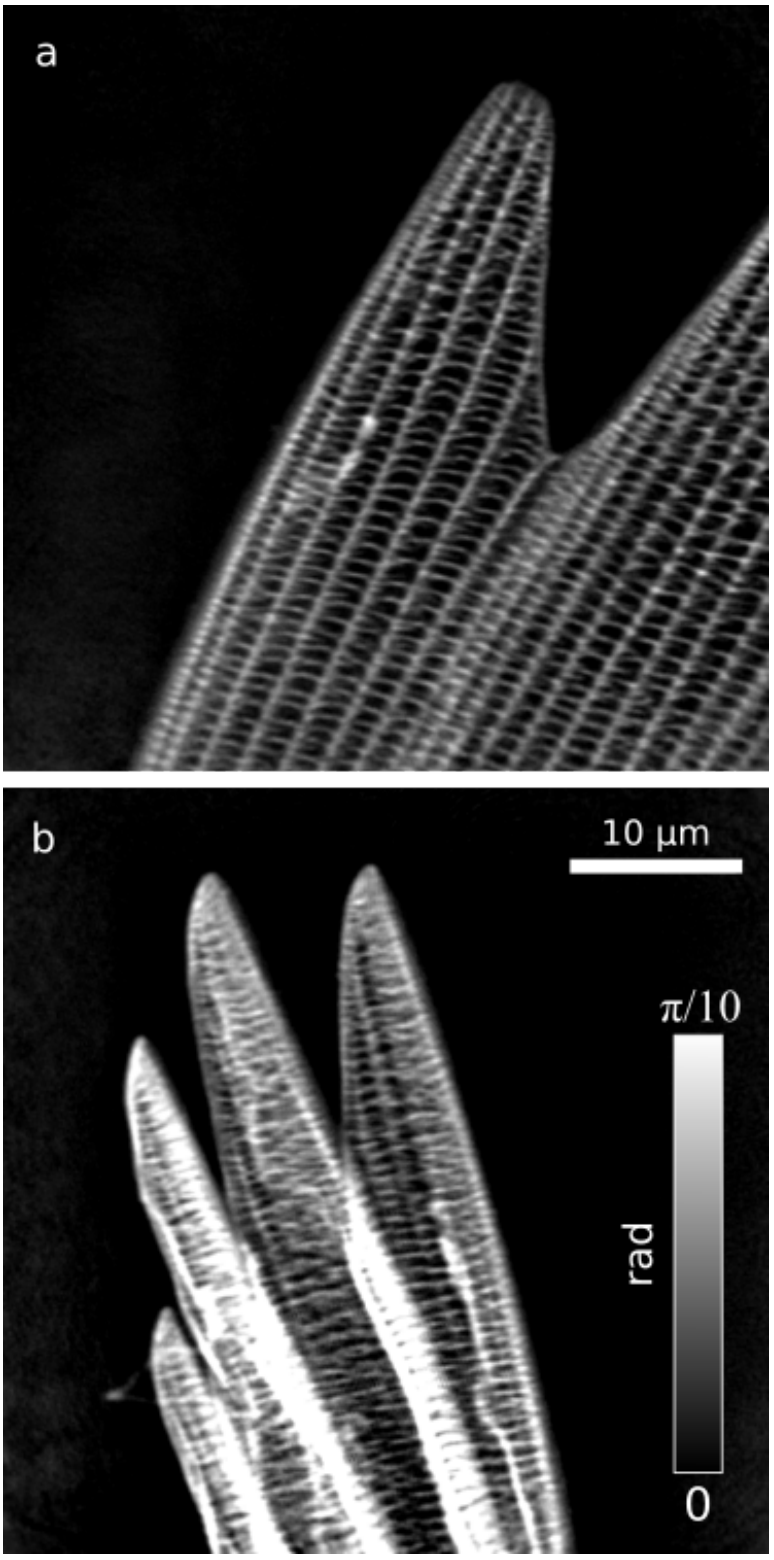

FIGURE 5.5: Phase images of the apical region of a brown cover scale extracted from the wing of a male pansy butterfly. Projections were reconstructed via far-field ptychography from scans collected at different sample orientations: (a) 0° and (b) 146°. Axial ridges and crossribs (cf Fig. 5.2) are clearly resolved at all sample orientations. Only one of the tips of the jagged scale was within the scanned area at all orientations, as in (a), but up to four tips were visible at more sideways orientations, as in (b).

butterfly scale. The largest phase shift φ found for the widest sample orientations lied in the range 0.24-0.27. Based on Eq. 2.26, using a δ value of $3.2 \cdot 10^{-6}$ as found in Fig. 2.3 for 9.7 keV and correcting for sample tilt (ca. 78°), this corresponds to a range of thickness of 0.9-1.0 µm for the largest chitin structures composing the butterfly scale, in agreement with the expected value (ca. 1 µm) as well as that found from the experiment at ESRF.

5.3 Tomographic analysis

Once all the 2D projections were retrieved and corrected from both experiments, they became datasets suitable for tomographic analysis. In order to produce sinograms suited for filtered back-projection (FBP), individual 2D projections had to be aligned with respect to each other, both vertically and horizontally. Some basic alignment procedure for ptychographic projections within PXCT experiments is well presented by Guizar-Sicairos et al. (2011). The fact that for these measurements parts of the imaged samples fell out of the FOV at several orientations required however a more elaborate aligning procedure, especially suited to tackle issues of missing wedge or – as it was the case for the reconstruction from the experiment at DLS presented in the previous section (Section 5.2) – partial local tomography. In particular, a customised implementation of the tomographic consistency approach (Guizar-Sicairos et al., 2015a) was found successful. For clarity and conciseness, only the alignment routine applied to the results from Section 5.2 is presented: customised variations of the same approach remain valid for all datasets produced by ptychographic analysis.

First, vertical alignment was carried out exploiting a first order – vertical derivative only – gaussian smoothing filter able to highlight the top pixel of the sample at every orientation by comparing the maximum values of each row. Cross-correlation was then applied to this collection of values for the topmost area of each projection to vertically align them within an estimated range of 2-3 pixels.

For horizontal alignment an iterative approach inspired by the principle of tomographic consistency was applied. A sinogram was produced as the mean of a series of sinograms within a narrow vertical range (10 pixels). Such mean sinogram was then padded, both to compensate for misalignment of the rotation axis with respect to the centre of the FOV of the reconstructions and to expand the FOV itself enough to include at least the second tip of the scale, visible only at about 2/3 of the collected sample orientations (cf Fig. 5.5). Then at each iteration a filtered back-projection is applied to the sinogram exploiting a Hamming window and an inverse Radon transform and generating a tomogram (step 1). A smoothing filter and some lower- and upper-value thresholding is applied to such tomogram (step 2) which is then projected back to

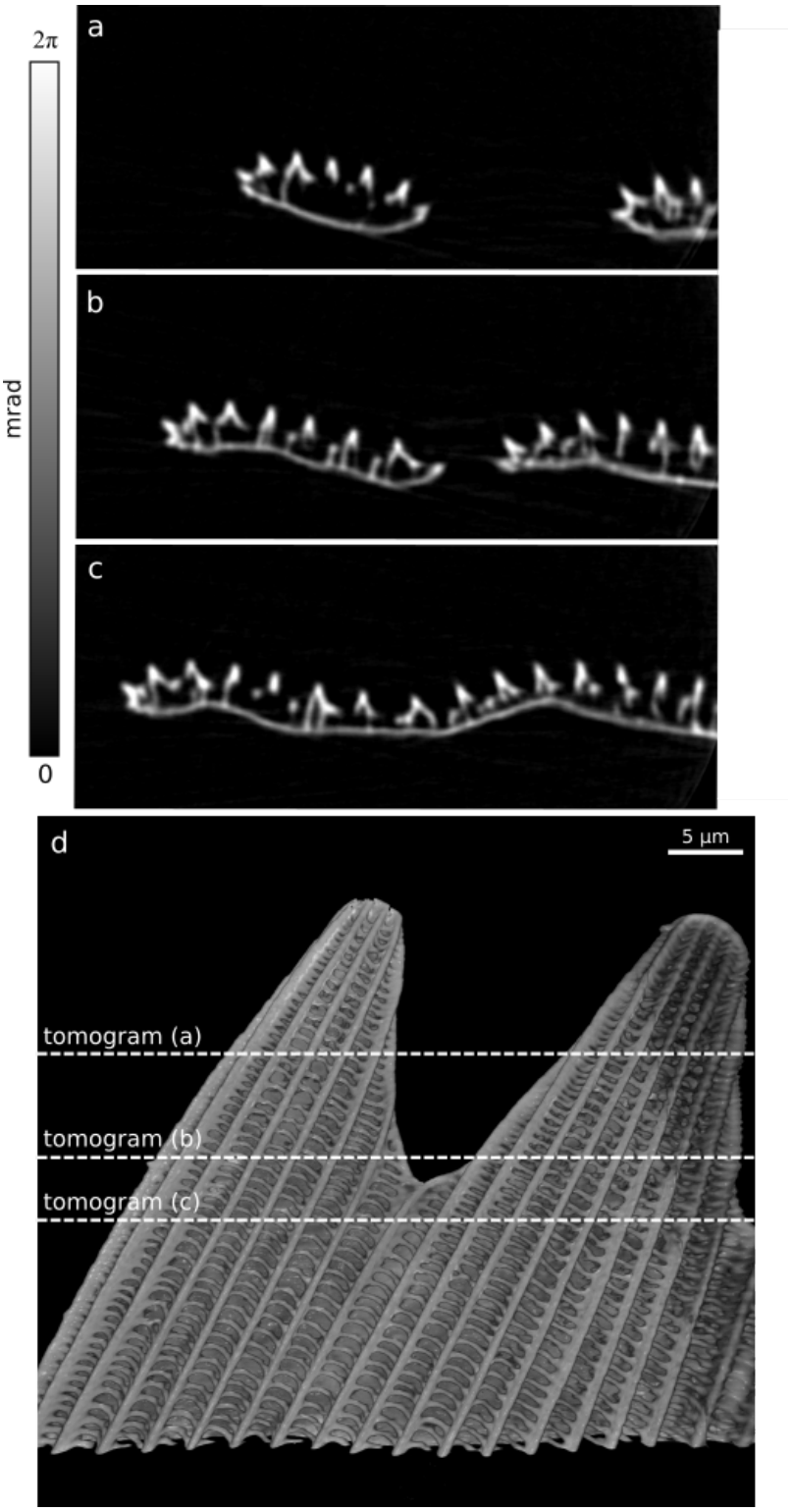

FIGURE 5.6: (a-c) Phase tomograms including two tips of the apical region of a brown cover scale extracted from the wing of a female pansy butterfly. (a), (b) and (c) represent horizontal slices produced at 12.8 µm, 20.9 µm and 25.6 µm from the top of the scale, respectively. (d) 3D rendering obtained from a stack of 750 such phase tomograms using Drishti (Limaye, 2012). Approximate regions to which tomograms from (a), (b) and (c) refer are annotated. Rendering allows to explore the reconstructed volume and in particular the pillar-like trabeculae connecting the lower lamina to the intricately patterned upper lamina formed of longitudinal ridges and crossribs as well as the windows, i.e. the open spaces between them.

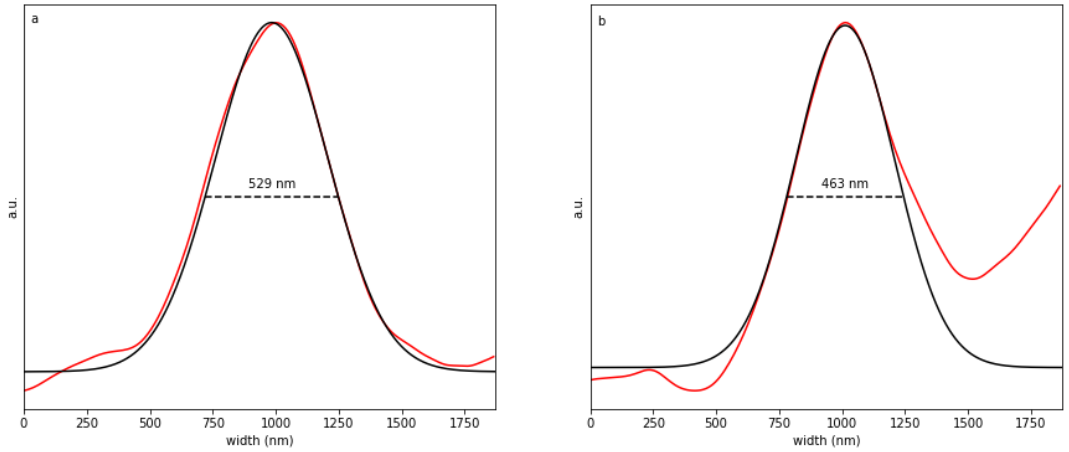

FIGURE 5.7: Gaussian fits along paths perpendicular to the lower lamina at different positions within a reconstructed phase tomogram of a brown cover scale from a female pansy butterfly. The full width at half maximum (FWHM) of the gaussian curve is annotated on each plot and is taken as an estimate of the thickness of the lower lamina.

the sinogram space via Radon transformation (step 3) generating a naturally aligned sinogram within the whole padded FOV. This is used as a reference to align the original projections contained within the sinogram from the previous iteration – i.e. before step 1 – via a windowed cross-correlation (step 4) concluding a full 4-step iteration. A few such iterations (3-6) were already enough to achieve horizontal alignment allowing for tomographic reconstruction to be run on the full dataset.

Applying FBP to the corrected phase part of the full stack of aligned projections led to the results shown in Fig. 5.6. In particular Fig.s 5.6a-c show phase tomograms of a region including 2 scale tips which was sectioned horizontally at different heights. Fig. 5.6d shows a 3D-rendered image of the whole reconstructed phase volume obtained exploiting the open-source volume exploration package Drishti (Limaye, 2012).

The retrieved tomograms were exploited to determine the thickness of the ventral side of the scale corresponding to the lower lamina. Using gaussian fits, an estimate of the FWHM in the range 460-530 nm was produced. Fig. 5.7 shows two examples of these fits for paths perpendicular to the lower lamina at different positions.

More in general the volumetric reconstruction of a scale and its 3D rendering reveal the pillar-like trabeculae connecting the lower lamina to the intricately patterned upper lamina formed of longitudinal ridges and crossribs as well as the windows, i.e. the open spaces between them. These are features hardly accessible via SEM which requires high-precision sectioning to reveal them.

5.4 Conclusions

PXCT experiments were successfully carried out in the near-field propagation regime at ID16A, ESRF and in the far-field at I13-1, DLS, on several weakly-scattering butterfly wing scales hosting chitin nanostructures. Ptychographic analysis produced full sets of phase-contrast 2D projections at several sample orientations. Tomographic analysis on such sets produced quantitative volumetric reconstructions of the scanned regions which – exploiting 3D rendering and exploration tools – could be investigated for structure determination and comparison at high resolution. In particular, scale features such as trabeculae and windows were revealed which were not previously accessible via SEM nor optical microscopy. As data were collected on scales belonging to both female and male sexes, high-resolution morphological information could directly be exploited to assess structural sexual dimorphism within pansy butterflies, especially within the context of artificial selection and evolution. Furthermore, these data are expected to be combined with other imaging modes, such as XRF and XAS, to provide complementary – especially chemical – information. However, this does not fall within the scope of this work but is rather the research interest of the collaborating synchrotron-user group.

This study and its results demonstrate the viability of PXCT as a high-resolution characterisation tool for reproducible and routine non-destructive analysis of butterfly scales from different individuals and species, suited to address the needs of evolutionary developmental biology and bioengineering studies on such species.

Sample drifts (and drops) partly hindered the achievable resolution and quality of 3D reconstructions, also giving rise to artefacts. This issue is expected to be addressed by increasing setup stability both by acting on the motor encoders but especially by improving sample mounting.

Finally, it is worth pointing out these results include the first successful implementation of PXCT on real-life samples at the I13-1 Coherence Branchline at DLS. This was made the object of a manuscript submitted to a scientific journal for publication and undergoing peer-review at the time of writing.

Chapter 6

Concluding remarks

This work presented three distinct pieces of research all sharing the development and implementation of ptychography as their central core and, at the same time, each advancing its realm of application in individually distinct directions.

After a short introduction containing a statement about the contribution of other researchers to this work (Chapter 1), some elements of X-ray physics in general and ptychography in particular have been briefly summarised in order to set the background for the general topic (Chapter 2).

Chapter 3 featured a detailed discussion on how to best exploit ptychography – in both its near-field and far-field variants – within X-ray imaging experiments, integrating it with other complementary imaging techniques in a way oriented towards time efficiency. It provided a rather practical view on real-life experiments at modern imaging beamlines where hardware and time requirements often lead to unforeseen constraints to be reckoned with within the time-limited high-investment experiments which are beamtimes. The theoretical and general comparison among compatible imaging techniques is intended to be used as guideline when preparing and managing such experiments. Such tool has been complemented by a collection of experimental results achieved exploiting it, which also give a taste of its range of applicability.

Chapter 4 presents a novel application of ptychography which contributes to the beam diagnostics toolkit available at high-brilliance sources. Ptychography is already established as a high-resolution phase-sensitive wavefront characterisation tool and its application is here expanded further to address the needs of the recent rise of ultra-short pulsed sources, namely FELs. The presented approach allows to retrieve single-pulse information providing an unprecedented insight into the properties of the X-ray pulses generated at such large-scale facilities. Its application at other end stations is sure to bear fruit, especially within the context of the upcoming European XFEL, cutting-edge source currently leading the advancement of FELs worldwide.

Chapter 5 presented the first successful implementation and demonstration of PXCT performed at the I13-1 Coherence Branchline at DLS on real-life samples, namely chitin scales from butterfly wings. Results from experiments at both I13-1 and ID16A at ESRF are discussed detailing the whole data processing pipeline from data acquisition to 3D-rendered images. On the one hand quantitative 3D characterisation of butterfly scales directly addresses the needs of some evolutionary developmental biology studies thus contributing to a diverse field of research. On the other hand the methodology further validated within these experiments contributes to the expansion of the range of application of X-ray ptychography and its availability to beamline users, external to the field of X-ray physics and synchrotron science.

All of these small individual achievements constitute steps in the further advancement of science, sitting somewhat halfway between applied and fundamental research. They contribute to enrich the body of knowledge from which both X-ray imaging specialists and external users can draw. In fact, the former benefit from the insight provided on ptychographic algorithms, methodology and ways of use within real-life experiments, whereas the latter are simply offered another high-resolution phase-contrast imaging tool, now slightly more user-friendly and hence accessible to non-specialists. In this regard, the long-term goals are to further establish ptychographic data acquisition and processing, expand its range of applicability in terms of relaxation of experimental constraints and improve its achievable resolving power, till one day phase-contrast ptychographic images will be as accessible and normal to collect as a hand X-ray.

Acknowledgements

I would like to thank my academic supervisor Pierre Thibault for giving me the opportunity to carry out my PhD, for the always profitable discussions and for providing several networking opportunities. I am also very grateful for his continuous support on *PtyPy*.

I would like to thank my Diamond supervisor Christoph Rau for hosting me at I13-1 and giving me several opportunities to carry out experiments there.

I would like to thank V. Charan Kuppili and Stefanos Chalkidis for support and discussions, especially during beamtimes.

I would like to thank Benedikt Daurer for the enjoyable and instructive collaboration on the XFEL project.

I am grateful to Filipe Maia, Julio da Silva, Peter Cloetens, Flavio Capotondi and Maya Kiskinova for hosting me at their labs. I would also like to thank them for their support for and during beamtimes along with Hans Deyhle, Sharif Ahmed, Darren Batey, Michal Odstrcil, Max Hantke, Duane Loh, Andy Aquila, Emanuele Pedersoli, Marie Zdora, Aaron Parson, Kaz Wanelik, Andy Wilson, Simon Logan, Ulrich Wagner, Stella Harrison and Leo Rowe-Brown.

I am grateful to Des McMorrow and John Rodenburg for their thorough review of this thesis and their valuable comments, and to Ian Robinson and Graeme Morrison for their precious input throughout my upgrade process.

I would like to acknowledge Zerina Johanson, Asa Barber and Anupama Prakash for providing samples on which X-ray ptychography imaging experiments have been performed.

Bibliography

B. Abbey, K. A. Nugent, G. J. Williams, J. N. Clark, A. G. Peele, M. A. Pfeifer, M. De Jonge, and I. McNulty. Keyhole coherent diffractive imaging. *Nature Physics*, 4(5): 394–398, 2008.

B. Abbey, L. W. Whitehead, H. M. Quiney, D. J. Vine, G. A. Cadenazzi, C. A. Henderson, K. A. Nugent, E. Balaur, C. T. Putkunz, A. G. Peele, G. J. Williams, and I. McNulty. Lensless imaging using broadband X-ray sources. *Nature Photonics*, 5(7): 420–424, 2011.

E. Allaria, L. Badano, S. Bassanese, F. Capotondi, D. Castronovo, P. Cinquegrana, M. B. Danailov, G. D'Auria, A. Demidovich, R. De Monte, G. De Ninno, S. Di Mitri, B. Diviacco, W. M. Fawley, M. Ferianis, E. Ferrari, G. Gaio, D. Gauthier, L. Giannessi, F. Iazzourene, G. Kurdi, N. Mahne, I. Nikolov, F. Parmigiani, G. Penco, L. Raimondi, P. Rebernik, F. Rossi, E. Roussel, C. Scafuri, C. Serpico, P. Sigalotti, C. Spezzani, M. Svandrlik, C. Svetina, M. Trovó, M. Veronese, D. Zangrando, and M. Zangrando. The FERMI free-electron lasers. *Journal of Synchrotron Radiation*, 22(March):485–491, 2015.

J. Als-Nielsen and D. McMorrow. *Elements of modern X-ray physics*. Wiley, second edition, 2011.

A. V. Baez. Fresnel Zone Plate for Optical Image Formation Using Extreme Ultraviolet and Soft X Radiation. *Journal of the Optical Society of America*, 51(4):405–412, 1961.

A. H. Barber, D. Lu, and N. M. Pugno. Extreme strength observed in limpet teeth. *Journal of the Royal Society, Interface / the Royal Society*, 12(105):20141326–, 2015.

I. Barke, H. Hartmann, D. Rupp, L. Flückiger, M. Sauppe, M. Adolph, S. Schorb, C. Bostedt, R. Treusch, C. Peltz, S. Bartling, T. Fennel, K. H. Meiwes-Broer, and T. Möller. The 3D-architecture of individual free silver nanoparticles captured by X-ray scattering. *Nature Communications*, 6:1–7, 2015.

R. H. T. Bates and J. M. Rodenburg. Sub-ångström transmission microscopy: A fourier transform algorithm for microdiffraction plane intensity information. *Ultramicroscopy*, 31(3):303–307, 1989.

M. Beckers, T. Senkbeil, T. Gorniak, M. Reese, K. Giewekemeyer, S. C. Gleber, T. Salditt, and A. Rosenhahn. Chemical contrast in soft X-ray ptychography. *Physical Review Letters*, 107(20):1–4, 2011.

M. Beckers, T. Senkbeil, T. Gorniak, K. Giewekemeyer, T. Salditt, and A. Rosenhahn. Drift correction in ptychographic diffractive imaging. *Ultramicroscopy*, 126:44–47, 2013.

Y. M. Bruck and L. G. Sodin. On the ambiguity of the image reconstruction problem. *Optics Communications*, 30(3):304–308, 1979.

F. Capotondi, E. Pedersoli, F. Bencivenga, M. Manfredda, N. Mahne, L. Raimondi, C. Svetina, M. Zangrando, A. Demidovich, I. Nikolov, M. Danailov, C. Masciovecchio, and M. Kiskinova. Multipurpose end-station for coherent diffraction imaging and scattering at FERMI@Elettra free-electron laser facility. *Journal of Synchrotron Radiation*, 22:544–552, 2015.

J. Chalupsky, P. Bohacek, V. Hajkova, S. P. Hau-Riege, P. A. Heimann, L. Juha, J. Krzywinski, M. Messerschmidt, S. P. Moeller, B. Nagler, M. Rowen, W. F. Schlotter, M. L. Swiggers, and J. J. Turner. Comparing different approaches to characterization of focused X-ray laser beams. *Nuclear Instruments and Methods in Physics Research, Section A: Accelerators, Spectrometers, Detectors and Associated Equipment*, 631(1): 130–133, 2011.

H. N. Chapman. Phase-retrieval X-ray microscopy by Wigner-distribution deconvolution. *Ultramicroscopy*, 66(3-4):153–172, 1996.

H. N. Chapman. Phase-retrieval X-ray microscopy by Wigner-distribution deconvolution: signal processing. *Scanning microscopy*, 11:67–80, 1997.

H. N. Chapman, C. Jacobsen, and S. Williams. Applications of a CCD detector in scanning transmission x-ray microscope. *Review of Scientific Instruments*, 66(2):1332–1334, 1995.

H. N. Chapman, A. Barty, M. J. Bogan, S. Boutet, M. Frank, S. P. Hau-Riege, S. Marchesini, B. W. Woods, S. Bajt, W. H. Benner, R. A. London, E. Plönjes, M. Kuhlmann, R. Treusch, S. Düsterer, T. Tschentscher, J. R. Schneider, E. Spiller, T. Möller, C. Bostedt, M. Hoener, D. A. Shapiro, K. O. Hodgson, D. van der Spoel, F. Burmeister, M. Bergh, C. Caleman, G. Huldt, M. M. Seibert, F. R. N. C. Maia, R. W. Lee,

A. Szöke, N. Timneanu, and J. Hajdu. Femtosecond diffractive imaging with a soft-X-ray free-electron laser. *Nature Physics*, 2(12):839–843, 2006a.

H. N. Chapman, A. Barty, S. Marchesini, A. Noy, A. P. Hau-Riege, C. Cui, M. Howells, R. Rosen, H. He, J. C. H. Spence, U. Weiestall, T. Beetz, C. Jacobsen, and D. Saphiro. High Resolution ab initio three-dimensional X-ray diffraction microscopy. *Journal of the Optical Society of America A*, 23(5):1179–1200, 2006b.

J. N. Clark and A. G. Peele. Simultaneous sample and spatial coherence characterisation using diffractive imaging. *Applied Physics Letters*, 99(15), 2011.

J. N. Clark, X. Huang, R. J. Harder, and I. K. Robinson. Continuous scanning mode for ptychography. *Optics Letters*, 39(20):6066, 2014.

R. A. Crowther, D. J. DeRosier, and A. Klug. The reconstruction of a three-dimensional structure from projections and its application to electron microscopy. *Proceedings of the Royal Society of London A: Mathematical and Physical Sciences*, 317:319–340, 1970.

J. C. da Silva, K. Mader, M. Holler, D. Haberthür, A. Diaz, M. Guizar-Sicairos, W. C. Cheng, Y. Shu, J. Raabe, A. Menzel, and J. A. van Bokhoven. Assessment of the 3-D pore structure and individual components of preshaped catalyst bodies by X-ray imaging. *ChemCatChem*, 7(3):413–416, 2015.

J. C. da Silva, J. Haubrich, G. Requena, M. Hubert, A. Pacureanu, L. Bloch, Y. Yang, and P. Cloetens. High energy near- and far-field ptychographic tomography at the ESRF. *Proceedings of SPIE*, 10391(September 2017):1039106, 2017a.

J. C. da Silva, A. Pacureanu, Y. Yang, S. Bohic, C. Morawe, R. Barrett, and P. Cloetens. Efficient concentration of high-energy x-rays for diffraction-limited imaging resolution. *Optica*, 4(5):492, 2017b.

J. C. da Silva, A. Pacureanu, Y. Yang, F. Fus, M. Hubert, L. Bloch, M. Salome, S. Bohic, and P. Cloetens. High-energy cryo x-ray nano-imaging at the ID16A beamline of ESRF. *Proceedings of SPIE*, 10389(September 2017):103890F, 2017c.

B. J. Daurer, M. F. Hantke, C. Nettelblad, and F. R. Maia. Hummingbird: Monitoring and analyzing flash X-ray imaging experiments in real time. *Journal of Applied Crystallography*, 49:1042–1047, 2016.

C. David, B. Nöhammer, H. H. Solak, and E. Ziegler. Differential x-ray phase contrast imaging using a shearing interferometer. *Applied Physics Letters*, 81(17):3287–3289, 2002.

J. Deng, Y. S. G. Nashed, S. Chen, N. W. Phillips, T. Peterka, R. Ross, S. Vogt, C. Jacobsen, and D. J. Vine. Continuous motion scan ptychography: characterization for increased speed in coherent x-ray imaging. *Optics Express*, 23(5):5438–5451, 2015a.

J. Deng, D. J. Vine, S. Chen, Y. S. G. Nashed, Q. Jin, N. W. Phillips, T. Peterka, R. Ross, S. Vogt, and C. J. Jacobsen. Simultaneous cryo X-ray ptychographic and fluorescence microscopy of green algae. *Proceedings of the National Academy of Sciences*, 112(8): 2314–2319, 2015b.

A. Diaz, P. Trtik, M. Guizar-Sicairos, A. Menzel, P. Thibault, and O. Bunk. Quantitative x-ray phase nanotomography. *Physical Review B*, 85:1–4, 2012.

M. Dierolf, A. Menzel, P. Thibault, P. Schneider, C. M. Kewish, R. Wepf, O. Bunk, and F. Pfeiffer. Ptychographic X-ray computed tomography at the nanoscale. *Nature*, 467 (7314):436–9, 2010.

B. Dromey, M. Zepf, A. Gopal, K. Lancaster, M. S. Wei, K. Krushelnick, M. Tatarakis, N. Vakakis, S. Moustaizis, R. Kodama, M. Tampo, C. Stoeckl, R. Clarke, H. Habara, D. Neely, S. Karsch, and P. Norreys. High harmonic generation in the relativistic limit. *Nature Physics*, 2(7):456–459, 2006.

E. Eggl, M. Dierolf, K. Achterhold, C. Jud, B. Günther, E. Braig, B. Gleich, and F. Pfeiffer. The Munich Compact Light Source: Initial performance measures. *Journal of Synchrotron Radiation*, 23:1137–1142, 2016.

D. Einfeld, M. Plesko, and J. Schaper. First multi-bend achromat lattice consideration. *Journal of Synchrotron Radiation*, 21(5):856–861, 2014.

T. Ekeberg, M. Svenda, C. Abergel, F. R. N. C. Maia, V. Seltzer, J. M. Claverie, M. Hantke, O. Jönsson, C. Nettelblad, G. Van Der Schot, M. Liang, D. P. Deponte, A. Barty, M. M. Seibert, B. Iwan, I. Andersson, N. D. Loh, A. V. Martin, H. Chapman, C. Bostedt, J. D. Bozek, K. R. Ferguson, J. Krzywinski, S. W. Epp, D. Rolles, A. Rudenko, R. Hartmann, N. Kimmel, and J. Hajdu. Three-dimensional reconstruction of the giant mimivirus particle with an X-ray free-electron laser. *Physical Review Letters*, 114(9):1–6, 2015.

V. Elser. Phase retrieval by iterated projections. *Journal of the Optical Society of America A*, 20(1):40–55, 2003.

P. Emma, R. Akre, J. Arthur, R. Bionta, C. Bostedt, J. Bozek, A. Brachmann, P. Bucksbaum, R. Coffee, F.-J. Decker, Y. Ding, D. Dowell, S. Edstrom, A. Fisher, J. Frisch, S. Gilevich, J. Hastings, G. Hays, P. Hering, Z. Huang, R. Iverson, H. Loos, M. Messerschmidt, A. Miahnahri, S. Moeller, H.-D. Nuhn, G. Pile, D. Ratner, J. Rzepiela,

D. Schultz, T. Smith, P. Stefan, H. Tompkins, J. Turner, J. Welch, W. White, J. Wu, G. Yocky, and J. Galayda. First lasing and operation of an ångstrom-wavelength free-electron laser. *Nature Photonics*, 4(9):641–647, 2010.

B. Enders and P. Thibault. A computational framework for ptychographic reconstructions. *Proceedings of the Royal Society of London A: Mathematical, Physical and Engineering Sciences*, 472(2196), 2016.

B. Enders, M. Dierolf, P. Cloetens, M. Stockmar, F. Pfeiffer, and P. Thibault. Ptychography with broad-bandwidth radiation. *Applied Physics Letters*, 104(17):171104, 2014.

H. M. L. Faulkner and J. M. Rodenburg. Movable aperture lensless transmission microscopy: A novel phase retrieval algorithm. *Physical Review Letters*, 93(2):023903–1, 2004.

J. Feldhaus, E. L. Saldin, J. R. Schneider, E. A. Schneidmiller, and M. V. Yurkov. Possible application of X-ray optical elements for reducing the spectral bandwidth of an X-ray SASE FEL. *Nuclear Instruments and Methods in Physics Research, Section A: Accelerators, Spectrometers, Detectors and Associated Equipment*, 393(1-3):162–166, 1997.

K. R. Ferguson, M. Bucher, J. D. Bozek, S. Carron, J. C. Castagna, R. Coffee, G. I. Curiel, M. Holmes, J. Krzywinski, M. Messerschmidt, M. Minitti, A. Mitra, S. Moeller, P. Noonan, T. Osipov, S. Schorb, M. Swiggers, A. Wallace, J. Yin, and C. Bostedt. The Atomic, Molecular and Optical Science instrument at the Linac Coherent Light Source. *Journal of Synchrotron Radiation*, 22:492–497, 2015.

J. Fienup. Reconstruction of an object from the modulus of its Fourier transform. *Optics letters*, 3(1):27–29, 1978.

J. R. Fienup. Phase retrieval algorithms: a comparison. *Applied Optics*, 21(15):2758–2769, 1982.

M. Fuchs, R. Weingartner, A. Popp, Z. Major, S. Becker, J. Osterhoff, I. Cortrie, B. Zeitler, R. Hörlein, G. D. Tsakiris, U. Schramm, T. P. Rowlands-Rees, S. M. Hooker, D. Habs, F. Krausz, S. Karsch, and F. Grüner. Laser-driven soft-X-ray undulator source. *Nature Physics*, 5(11):826–829, 2009.

D. Gabor. A new microscopic principle. *Nature*, 161(4098):777–778, 1948.

R. W. Gerchberg and W. O. Saxton. A practical algorithm for the determination of phase from image and diffraction plane pictures. *Optik*, 35(2):237–246, 1972.

H. Ghiradella. Structure of butterfly scales: Patterning in an insect cuticle. *Microscopy Research and Technique*, 27(5):429–438, 1994.

H. Ghiradella. Insect Cuticular Surface Modifications: Scales and Other Structural Formations. In *Advances in Insect Physiology*, chapter 4, pages 135–180. Elsevier Ltd, 2010.

A. Gianoncelli, G. R. Morrison, B. Kaulich, D. Bacescu, and J. Kovac. Scanning transmission x-ray microscopy with a configurable detector. *Applied Physics Letters*, 89 (25):10–13, 2006.

M. Guizar-Sicairos and J. R. Fienup. Phase retrieval with transverse translation diversity: a nonlinear optimization approach. *Optics Express*, 16(10):7264, 2008.

M. Guizar-Sicairos, A. Diaz, M. Holler, M. S. Lucas, A. Menzel, R. a. Wepf, and O. Bunk. Phase tomography from x-ray coherent diffractive imaging projections. *Optics Express*, 19(22):21345, 2011.

M. Guizar-Sicairos, J. J. Boon, K. Mader, A. Diaz, A. Menzel, and O. Bunk. Quantitative interior x-ray nanotomography by a hybrid imaging technique. *Optica*, 2(3): 259–266, 2015a.

M. Guizar-Sicairos, M. Holler, A. Diaz, J. C. da Silva, E. H. R. Tsai, O. Bunk, C. Martinez-Perez, P. C. J. Donoghue, C. H. Wellman, and A. Menzel. Ptychographic nanotomography at the Swiss Light Source. *Proceedings of SPIE*, 9592:95920A, 2015b.

M. F. Hantke, D. Hasse, F. R. N. C. Maia, T. Ekeberg, K. John, M. Svenda, N. D. Loh, A. V. Martin, N. Timneanu, D. S. D. Larsson, G. van der Schot, G. H. Carlsson, M. Ingelman, J. Andreasson, D. Westphal, M. Liang, F. Stellato, D. P. DePonte, R. Hartmann, N. Kimmel, R. a. Kirian, M. M. Seibert, K. Mühlig, S. Schorb, K. Ferguson, C. Bostedt, S. Carron, J. D. Bozek, D. Rolles, A. Rudenko, S. Epp, H. N. Chapman, A. Barty, J. Hajdu, and I. Andersson. High-throughput imaging of heterogeneous cell organelles with an X-ray laser. *Nature Photonics*, 8(12):943–949, 2014.

P. Hart, S. Boutet, G. Carini, M. Dubrovin, B. Duda, D. Fritz, G. Haller, R. Herbst, S. Herrmann, C. Kenney, N. Kurita, H. Lemke, M. Messerschmidt, M. Nordby, J. Pines, D. Schafer, M. Swift, M. Weaver, G. Williams, D. Zhu, N. Van Bakel, and J. Morse. The CSPAD megapixel x-ray camera at LCLS. *Proceedings of SPIE*, 8504:85040C, 2012.

R. Hegerl and W. Hoppe. Dynamische Theorie der Kristallstrukturanalyse durch Elektronenbeugung im inhomogenen Primärstrahlwellenfeld. *Berichte der Bunsengesellschaft für physikalische Chemie*, 74(3):1148–1154, 1970.

O. Hemberg, M. Otendal, and H. M. Hertz. Liquid-metal-jet anode electron-impact x-ray source. *Applied Physics Letters*, 83(7):1483–1485, 2003.

R. Henderson. The potential and limitations of neutrons, electrons and X-rays for atomic resolution microscopy of unstained biological molecules. *Quarterly Reviews of Biophysics*, 28(02):171, 1995.

B. L. Henke, E. M. Gullikson, and J. C. Davis. X-ray interactions: Photoabsorption, scattering, transmission, and reflection at E = 50-30,000 eV, Z = 1-92. *Atomic Data and Nuclear Data Tables*, 54(2):181–342, 1993.

R. Hettel. DLSR design and plans: An international overview. *Journal of Synchrotron Radiation*, 21(5):843–855, 2014.

M. Holler, A. Diaz, M. Guizar-Sicairos, P. Karvinen, E. Färm, E. Härkönen, M. Ritala, A. Menzel, J. Raabe, and O. Bunk. X-ray ptychographic computed tomography at 16 nm isotropic 3D resolution. *Scientific reports*, 4:3857, 2014.

M. Holler, M. Guizar-Sicairos, E. H. Tsai, R. Dinapoli, E. Müller, O. Bunk, J. Raabe, and G. Aeppli. High-resolution non-destructive three-dimensional imaging of integrated circuits. *Nature*, 543(7645):402–406, 2017.

J. M. Holton. A beginner's guide to radiation damage. *Journal of Synchrotron Radiation*, 16(2):133–142, 2009.

S. Hönig, R. Hoppe, J. Patommel, A. Schropp, S. Stephan, S. Schöder, M. Burghammer, and C. G. Schroer. Full optical characterization of coherent x-ray nanobeams by ptychographic imaging. *Optics Express*, 19(17):16324, 2011.

W. Hoppe. Beugung im inhomogenen Primärstrahlwellenfeld. III. Amplituden- und Phasenbestimmung bei unperiodischen Objekten. *Acta Crystallographica Section A*, 25(4):508–514, 1969.

P. Horowitz and J. a. Howell. A scanning x-ray microscope using synchrotron radiation. *Science*, 178(61):608–611, 1972.

A. Hosseinizadeh, G. Mashayekhi, J. Copperman, P. Schwander, A. Dashti, R. Sepehr, R. Fung, M. Schmidt, C. H. Yoon, B. G. Hogue, G. J. Williams, A. Aquila, and A. Ourmazd. Conformational landscape of a virus by single-particle X-ray scattering. *Nature Methods*, 14(9):877–881, 2017.

M. R. Howells, T. Beetz, H. N. Chapman, C. Cui, J. M. Holton, C. J. Jacobsen, J. Kirz, E. Lima, S. Marchesini, H. Miao, D. Sayre, D. A. Shapiro, J. C. H. Spence, and

D. Starodub. An assessment of the resolution limitation due to radiation-damage in X-ray diffraction microscopy. *Journal of Electron Spectroscopy and Related Phenomena*, 170(1-3):4–12, 2009.

Z. Huang and K. J. Kim. Review of x-ray free-electron laser theory. *Physical Review Special Topics - Accelerators and Beams*, 10(3):1–26, 2007.

Z. Huang and R. D. Ruth. Laser-Electron Storage Ring. *Physical Review Letters*, 80(5): 976–979, 1998.

Y. Jiang, Z. Chen, Y. Han, P. Deb, H. Gao, S. Xie, P. Purohit, M. W. Tate, J. Park, S. M. Gruner, V. Elser, and D. A. Muller. Electron ptychography of 2D materials to deep sub-ångström resolution. *Nature*, 559(7714):343–349, 2018.

Z. Johanson, M. Smith, A. Kearsley, P. Pilecki, E. Mark-Kurik, and C. Howard. Origins of bone repair in the armour of fossil fish: response to a deep wound by cells depositing dentine instead of dermal bone. *Biology letters*, 9(5):20130144, 2013.

M. Kahnt, G. Falkenberg, J. Garrevoet, J. Hartmann, T. Krause, M. Niehle, M. Scholz, M. Seyrich, A. Trampert, A. Waag, H.-H. Wehmann, F. Wittwer, H. Zhou, M. Hanke, and C. G. Schroer. Simultaneous Hard X-ray Ptychographic Tomography and X-ray Fluorescence To-mography of Isolated Hollow Core-Shell GaN Rods. *Microscopy and Microanalysis*, 24(S2):34–35, 2018.

B. Kaulich, P. Thibault, A. Gianoncelli, and M. Kiskinova. Transmission and emission x-ray microscopy: operation modes, contrast mechanisms and applications. *Journal of Physics: Condensed Matter*, 23(8):083002, 2011.

B. Keitel, E. Plönjes, S. Kreis, M. Kuhlmann, K. Tiedtke, T. Mey, B. Schäfer, and K. Mann. Hartmann wavefront sensors and their application at FLASH. *Journal of Synchrotron Radiation*, 23:43–49, 2016.

C. M. Kewish, P. Thibault, M. Dierolf, O. Bunk, A. Menzel, J. Vila-Comamala, K. Jefimovs, and F. Pfeiffer. Ptychographic characterization of the wavefield in the focus of reflective hard X-ray optics. *Ultramicroscopy*, 110(4):325–329, 2010.

P. Kirkpatrick and A. V. Baez. Formation of Optical Images by X-Rays. *Journal of the Optical Society of America*, 38(9):766–774, 1948.

S. Kneip, C. McGuffey, J. L. Martins, S. F. Martins, C. Bellei, V. Chvykov, F. Dollar, R. Fonseca, C. Huntington, G. Kalintchenko, A. Maksimchuk, S. P. Mangles, T. Matsuoka, S. R. Nagel, C. A. Palmer, J. Schreiber, K. T. Phuoc, A. G. Thomas, V. Yanovsky, L. O. Silva, K. Krushelnick, and Z. Najmudin. Bright spatially coherent synchrotron X-rays from a table-top source. *Nature Physics*, 6(12):980–983, 2010.

J. C. Labiche, O. Mathon, S. Pascarelli, M. A. Newton, G. G. Ferre, C. Curfs, G. Vaughan, A. Homs, and D. F. Carreiras. Invited article: The fast readout low noise camera as a versatile x-ray detector for time resolved dispersive extended x-ray absorption fine structure and diffraction studies of dynamic problems in materials science, chemistry, and catalysis. *Review of Scientific Instruments*, 78(9), 2007.

M. Liang, G. J. Williams, M. Messerschmidt, M. M. Seibert, P. A. Montanez, M. Hayes, D. Milathianaki, A. Aquila, M. S. Hunter, J. E. Koglin, D. W. Schafer, S. Guillet, A. Busse, R. Bergan, W. Olson, K. Fox, N. Stewart, R. Curtis, A. A. Miahnahri, and S. Boutet. The Coherent X-ray Imaging instrument at the Linac Coherent Light Source. *Journal of Synchrotron Radiation*, 22:514–519, 2015.

A. Limaye. Drishti: a volume exploration and presentation tool. *Proceedings of SPIE*, 8506:85060X, 2012.

L. Liu, N. Milas, A. H. C. Mukai, X. R. Resende, and F. H. De Sá. The sirius project. *Journal of Synchrotron Radiation*, 21(5):904–911, 2014.

Y. Liu, M. Seaberg, D. Zhu, J. Krzywinski, F. Seiboth, C. Hardin, D. Cocco, A. Aquila, B. Nagler, H. J. Lee, S. Boutet, Y. Feng, Y. Ding, G. Marcus, and A. Sakdinawat. High-accuracy wavefront sensing for x-ray free electron lasers. *Optica*, 5(8):967, 2018.

N. D. Loh, C. Y. Hampton, A. V. Martin, D. Starodub, R. G. Sierra, A. Barty, A. Aquila, J. Schulz, L. Lomb, J. Steinbrener, R. L. Shoeman, S. Kassemeyer, C. Bostedt, J. Bozek, S. W. Epp, B. Erk, R. Hartmann, D. Rolles, A. Rudenko, B. Rudek, L. Foucar, N. Kimmel, G. Weidenspointner, G. Hauser, P. Holl, E. Pedersoli, M. Liang, M. M. Hunter, L. Gumprecht, N. Coppola, C. Wunderer, H. Graafsma, F. R. Maia, T. Ekeberg, M. Hantke, H. Fleckenstein, H. Hirsemann, K. Nass, T. A. White, H. J. Tobias, G. R. Farquar, W. H. Benner, S. P. Hau-Riege, C. Reich, A. Hartmann, H. Soltau, S. Marchesini, S. Bajt, M. Barthelmess, P. Bucksbaum, K. O. Hodgson, L. Strüder, J. Ullrich, M. Frank, I. Schlichting, H. N. Chapman, and M. J. Bogan. Fractal morphology, imaging and mass spectrometry of single aerosol particles in flight. *Nature*, 486(7404):513–517, 2012.

N. D. Loh, D. Starodub, L. Lomb, C. Y. Hampton, A. V. Martin, R. G. Sierra, A. Barty, A. Aquila, J. Schulz, J. Steinbrener, R. L. Shoeman, S. Kassemeyer, C. Bostedt, J. Bozek, S. W. Epp, B. Erk, R. Hartmann, D. Rolles, A. Rudenko, B. Rudek, L. Foucar, N. Kimmel, G. Weidenspointner, G. Hauser, P. Holl, E. Pedersoli, M. Liang, M. S. Hunter, L. Gumprecht, N. Coppola, C. Wunderer, H. Graafsma, F. R. N. C. Maia, T. Ekeberg, M. Hantke, H. Fleckenstein, H. Hirsemann, K. Nass, T. a. White, H. J. Tobias, G. R. Farquar, W. H. Benner, S. Hau-Riege, C. Reich, A. Hartmann,

H. Soltau, S. Marchesini, S. Bajt, M. Barthelmess, L. Strueder, J. Ullrich, P. Bucksbaum, M. Frank, I. Schlichting, H. N. Chapman, and M. J. Bogan. Sensing the wavefront of x-ray free-electron lasers using aerosol spheres. *Optics express*, 21(10): 12385–94, 2013.

A. M. Maiden and J. M. Rodenburg. An improved ptychographical phase retrieval algorithm for diffractive imaging. *Ultramicroscopy*, 109(10):1256–1262, 2009.

A. M. Maiden, M. J. Humphry, and J. M. Rodenburg. Ptychographic transmission microscopy in three dimensions using a multi-slice approach. *Journal of the Optical Society of America A*, 29(8):1606, 2012a.

A. M. Maiden, M. J. Humphry, M. C. Sarahan, B. Kraus, and J. M. Rodenburg. An annealing algorithm to correct positioning errors in ptychography. *Ultramicroscopy*, 120:64–72, 2012b.

A. M. Maiden, G. R. Morrison, B. Kaulich, A. Gianoncelli, and J. M. Rodenburg. Soft X-ray spectromicroscopy using ptychography with randomly phased illumination. *Nature Communications*, 4:1666–1669, 2013.

J. Marangos. New Light Source (NLS) Project: Conceptual Design Report. Technical report, STFC, 2010.

J. Marangos. Introduction to the new science with X-ray free electron lasers. *Contemporary Physics*, 52:551–569, 2011.

J. Marchal, I. Horswell, B. Willis, R. Plackett, E. N. Gimenez, J. Spiers, D. Ballard, P. Booker, J. A. Thompson, P. Gibbons, S. R. Burge, T. Nicholls, J. Lipp, and N. Tartoni. EXCALIBUR: a small-pixel photon counting area detector for coherent X-ray diffraction - Front-end design, fabrication and characterisation. *Journal of Physics: Conference Series*, 425(6):062003, 2013.

S. Marchesini, H. Krishnan, B. J. Daurer, D. A. Shapiro, T. Perciano, J. A. Sethian, and F. R. N. C. Maia. SHARP: A distributed GPU-based ptychographic solver. *Journal of Applied Crystallography*, 49(4):1245–1252, 2016.

G. Margaritondo and P. Rebernik Ribic. A simplified description of X-ray free-electron lasers. *Journal of Synchrotron Radiation*, 18(2):101–108, 2011.

J. Miao, P. Charalambous, J. Kirz, and D. Sayre. Extending the methodology of X-ray crystallography to allow imaging of micrometre-sized non-crystalline specimens. *Nature*, 400(6742):342–344, 1999.

I. Mohacsi, I. Vartiainen, B. Rösner, M. Guizar-Sicairos, V. A. Guzenko, I. McNulty, R. Winarski, M. V. Holt, and C. David. Interlaced zone plate optics for hard X-ray imaging in the 10 nm range. *Scientific Reports*, 7:43624, 2017.

A. Momose. Recent Advances in X-ray Phase Imaging. *Japanese Journal of Applied Physics*, 44(9A):6355–6367, 2005.

C. Morawe, R. Barrett, P. Cloetens, B. Lantelme, J.-C. Peffen, and A. Vivo. Graded multilayers for figured Kirkpatrick-Baez mirrors on the new ESRF end station ID16A. *Proceedings of SPIE*, 9588:958803, 2015.

G. R. Morrison and J. N. Chapman. A comparison of three difrerential phase contrast systems suitable for use in STEM. *Optik*, 64(1):1–12, 1983.

A. Munke, J. Andreasson, A. Aquila, S. Awel, K. Ayyer, A. Barty, R. J. Bean, P. Berntsen, J. Bielecki, S. Boutet, M. Bucher, H. N. Chapman, B. J. Daurer, H. Demirci, V. Elser, P. Fromme, J. Hajdu, M. F. Hantke, A. Higashiura, B. G. Hogue, A. Hosseinizadeh, Y. Kim, R. A. Kirian, H. K. Reddy, T. Y. Lan, D. S. Larsson, H. Liu, N. D. Loh, F. R. Maia, A. P. Mancuso, K. Mühlig, A. Nakagawa, D. Nam, G. Nelson, C. Nettelblad, K. Okamoto, A. Ourmazd, M. Rose, G. Van Der Schot, P. Schwander, M. M. Seibert, J. A. Sellberg, R. G. Sierra, C. Song, M. Svenda, N. Timneanu, I. A. Vartanyants, D. Westphal, M. O. Wiedorn, G. J. Williams, P. L. Xavier, C. H. Yoon, and J. Zook. Coherent diffraction of single Rice Dwarf virus particles using hard X-rays at the Linac Coherent Light Source. *Scientific Data*, 3: 1–12, 2016.

R. Neutze, R. Wouts, D. van der Spoel, E. Weckert, and J. Hajdu. Potential for biomolecular imaging with femtosecond X-ray pulses. *Nature*, 406(6797):752–757, 2000.

M. Odstrcil, P. Baksh, S. A. Boden, R. Card, J. E. Chad, J. G. Frey, and W. S. Brocklesby. Ptychographic coherent diffractive imaging with orthogonal probe relaxation. *Optics Express*, 24(8):8360, 2016.

M. Odstrčil, A. Menzel, and M. Guizar-Sicairos. Iterative least-squares solver for generalized maximum-likelihood ptychography. *Optics Express*, 26(3):3108, 2018.

E. Pedersoli, F. Capotondi, D. Cocco, M. Zangrando, B. Kaulich, R. H. Menk, A. Locatelli, T. O. Mentes, C. Spezzani, G. Sandrin, D. M. Bacescu, M. Kiskinova, S. Bajt, M. Barthelmess, A. Barty, J. Schulz, L. Gumprecht, H. N. Chapman, A. J. Nelson, M. Frank, M. J. Pivovaroff, B. W. Woods, M. J. Bogan, and J. Hajdu. Multipurpose modular experimental station for the DiProI beamline of Fermi@Elettra free electron laser. *Review of Scientific Instruments*, 82(4), 2011.

P. M. Pelz, M. Guizar-Sicairos, P. Thibault, I. Johnson, M. Holler, and A. Menzel. On-the-fly scans for X-ray ptychography. *Applied Physics Letters*, 105(25):3–8, 2014.

F. Pfeiffer. X-ray ptychography. *Nature Photonics*, 12(1):9–17, 2018.

A. Prakash and A. Monteiro. apterous A specifies dorsal wing patterns and sexual traits in butterflies. *Proceedings of the Royal Society B: Biological Sciences*, 285(1873): 20172685, 2018.

C. Rau, U. Wagner, Z. Pešić, and A. De Fanis. Coherent imaging at the Diamond beamline I13. *Physica Status Solidi (A) Applications and Materials Science*, 208(11): 2522–2525, 2011.

H. K. Reddy, C. H. Yoon, A. Aquila, S. Awel, K. Ayyer, A. Barty, P. Berntsen, J. Bielecki, S. Bobkov, M. Bucher, G. A. Carini, S. Carron, H. Chapman, B. Daurer, H. Demirci, T. Ekeberg, P. Fromme, J. Hajdu, M. F. Hanke, P. Hart, B. G. Hogue, A. Hosseinizadeh, Y. Kim, R. A. Kirian, R. P. Kurta, D. S. Larsson, N. Duane Loh, F. R. Maia, A. P. Mancuso, K. Mühlig, A. Munke, D. Nam, C. Nettelblad, A. Ourmazd, M. Rose, P. Schwander, M. Seibert, J. A. Sellberg, C. Song, J. C. Spence, M. Svenda, G. Van Der Schot, I. A. Vartanyants, G. J. Williams, and P. Lourdu Xavier. Coherent soft X-ray diffraction imaging of coliphage PR772 at the Linac coherent light source. *Scientific Data*, 4:1–9, 2017.

J. M. Rodenburg. Ptychography and related diffractive imaging methods. *Advances in Imaging and Electron Physics*, 150(07):87–184, 2008.

J. M. Rodenburg and R. H. T. Bates. The Theory of Super-Resolution Electron Microscopy Via Wigner-Distribution Deconvolution. *Philosophical Transactions of the Royal Society A: Mathematical, Physical and Engineering Sciences*, 339(1655):521–553, 1992.

J. M. Rodenburg and H. M. L. Faulkner. A phase retrieval algorithm for shifting illumination. *Applied Physics Letters*, 85(20):4795–4797, 2004.

J. M. Rodenburg, B. C. McCallum, and P. D. Nellist. Experimental tests on double-resolution coherent imaging via STEM. *Ultramicroscopy*, 48(3):304–314, mar 1993.

J. M. Rodenburg, A. C. Hurst, A. G. Cullis, B. R. Dobson, F. Pfeiffer, O. Bunk, C. David, K. Jefimovs, and I. Johnson. Hard-X-ray lensless imaging of extended objects. *Physical Review Letters*, 98(3):1–4, 2007.

S. Rutishauser, L. Samoylova, J. Krzywinski, O. Bunk, J. Grünert, H. Sinn, M. Cammarata, D. M. Fritz, and C. David. Exploring the wavefront of hard X-ray free-electron laser radiation. *Nature communications*, 3:947, 2012.

S. Sala, V. S. C. Kuppili, S. Chalkidis, D. J. Batey, X. Shi, C. Rau, and P. Thibault. Multiscale X-ray imaging using ptychography. *Journal of Synchrotron Radiation*, 25 (4):1214–1221, 2018.

E. L. Saldin, E. A. Schneidmiller, Y. V. Shvyd'ko, and M. V. Yurkov. X-ray FEL with a meV bandwidth. *Nuclear Instruments and Methods in Physics Research, Section A: Accelerators, Spectrometers, Detectors and Associated Equipment*, 475(1-3):357–362, 2001.

D. Sayre. Some implications of a theorem due to Shannon. *Acta Crystallographica*, 5 (6):843–843, 1952.

M. Schneider, C. M. Günther, B. Pfau, F. Capotondi, M. Manfredda, M. Zangrando, N. Mahne, L. Raimondi, E. Pedersoli, D. Naumenko, and S. Eisebitt. In situ single-shot diffractive fluence mapping for X-ray free-electron laser pulses. *Nature Communications*, 9(1):1–6, 2018.

A. Schropp, P. Boye, J. M. Feldkamp, R. Hoppe, J. Patommel, D. Samberg, S. Stephan, K. Giewekemeyer, R. N. Wilke, T. Salditt, J. Gulden, A. P. Mancuso, I. A. Vartanyants, E. Weckert, S. Schöder, M. Burghammer, and C. G. Schroer. Hard x-ray nanobeam characterization by coherent diffraction microscopy. *Applied Physics Letters*, 96(9):091102, 2010.

A. Schropp, R. Hoppe, J. Patommel, D. Samberg, F. Seiboth, S. Stephan, G. Wellenreuther, G. Falkenberg, and C. G. Schroer. Hard x-ray scanning microscopy with coherent radiation: Beyond the resolution of conventional x-ray microscopes. *Applied Physics Letters*, 100(25):10–13, 2012.

A. Schropp, R. Hoppe, V. Meier, J. Patommel, F. Seiboth, H. J. Lee, B. Nagler, E. C. Galtier, B. Arnold, U. Zastrau, J. B. Hastings, D. Nilsson, F. Uhlén, U. Vogt, H. M. Hertz, and C. G. Schroer. Full spatial characterization of a nanofocused x-ray free-electron laser beam by ptychographic imaging. *Scientific reports*, 3:1633, 2013.

M. M. Seibert, T. Ekeberg, F. R. Maia, M. Svenda, J. Andreasson, O. Jönsson, D. Odić, B. Iwan, A. Rocker, D. Westphal, M. Hantke, D. P. Deponte, A. Barty, J. Schulz, L. Gumprecht, N. Coppola, A. Aquila, M. Liang, T. A. White, A. Martin, C. Caleman, S. Stern, C. Abergel, V. Seltzer, J. M. Claverie, C. Bostedt, J. D. Bozek, S. Boutet, A. A. Miahnahri, M. Messerschmidt, J. Krzywinski, G. Williams, K. O. Hodgson, M. J. Bogan, C. Y. Hampton, R. G. Sierra, D. Starodub, I. Andersson, S. Bajt, M. Barthelmess, J. C. Spence, P. Fromme, U. Weierstall, R. Kirian, M. Hunter, R. B. Doak, S. Marchesini, S. P. Hau-Riege, M. Frank, R. L. Shoeman, L. Lomb, S. W. Epp, R. Hartmann, D. Rolles, A. Rudenko, C. Schmidt, L. Foucar, N. Kimmel, P. Holl,

B. Rudek, B. Erk, A. Hömke, C. Reich, D. Pietschner, G. Weidenspointner, L. Strüder, G. Hauser, H. Gorke, J. Ullrich, I. Schlichting, S. Herrmann, G. Schaller, F. Schopper, H. Soltau, K. U. Kühnel, R. Andritschke, C. D. Schröter, F. Krasniqi, M. Bott, S. Schorb, D. Rupp, M. Adolph, T. Gorkhover, H. Hirsemann, G. Potdevin, H. Graafsma, B. Nilsson, H. N. Chapman, and J. Hajdu. Single mimivirus particles intercepted and imaged with an X-ray laser. *Nature*, 470(7332):78–82, 2011.

C. E. Shannon. Communication in the Presence of Noise. *Proceedings of the IRE*, 37 (1):10–21, 1949.

D. A. Shapiro, Y. S. Yu, T. Tyliszczak, J. Cabana, R. Celestre, W. Chao, K. Kaznatcheev, A. L. Kilcoyne, F. Maia, S. Marchesini, Y. S. Meng, T. Warwick, L. L. Yang, and H. A. Padmore. Chemical composition mapping with nanometre resolution by soft X-ray microscopy. *Nature Photonics*, 8(10):765–769, 2014.

M. Sikorski, S. Song, A. Schropp, F. Seiboth, Y. Feng, R. Alonso-Mori, M. Chollet, H. T. Lemke, D. Sokaras, T. C. Weng, W. Zhang, A. Robert, and D. Zhu. Focus characterization at an X-ray free-electron laser by coherent scattering and speckle analysis. *Journal of Synchrotron Radiation*, 22:599–605, 2015.

A. Singer, L. Boucheron, S. H. Dietze, K. E. Jensen, D. Vine, I. McNulty, E. R. Dufresne, R. O. Prum, S. G. J. Mochrie, and O. G. Shpyrko. Domain morphology, boundaries, and topological defects in biophotonic gyroid nanostructures of butterfly wing scales. *Science Advances*, 2(6):e1600149, 2016.

A. Snigirev, V. Kohn, I. Snigireva, and B. Lengeler. A compound refractive lens for focusing high-energy X-rays. *Nature*, 384(6604):49–51, 1996.

M. Stampanoni, R. Mokso, F. Marone, J. Vila-comamala, S. Gorelick, P. Trtik, K. Jefimovs, and C. David. Phase-contrast tomography at the nanoscale using hard x rays. *Physical Review B*, 81:1–4, 2010.

M. Stockmar, P. Cloetens, I. Zanette, B. Enders, M. Dierolf, F. Pfeiffer, and P. Thibault. Near-field ptychography: phase retrieval for inline holography using a structured illumination. *Scientific reports*, 3:1927, 2013.

M. Stockmar, M. Hubert, M. Dierolf, B. Enders, R. Clare, S. Allner, A. Fehringer, I. Zanette, J. Villanova, J. Laurencin, P. Cloetens, F. Pfeiffer, and P. Thibault. X-ray nanotomography using near-field ptychography. *Optics Express*, 23(10):12720, 2015a.

M. Stockmar, I. Zanette, M. Dierolf, B. Enders, R. Clare, F. Pfeiffer, P. Cloetens, A. Bonnin, and P. Thibault. X-ray near-field ptychography for optically thick specimens. *Physical Review Applied*, 3(1):014005, 2015b.

L. Strüder, S. Epp, D. Rolles, R. Hartmann, P. Holl, G. Lutz, H. Soltau, R. Eckart, C. Reich, K. Heinzinger, C. Thamm, A. Rudenko, F. Krasniqi, K. U. Kühnel, C. Bauer, C. D. Schröter, R. Moshammer, S. Techert, D. Miessner, M. Porro, O. Hälker, N. Meidinger, N. Kimmel, R. Andritschke, F. Schopper, G. Weidenspointner, A. Ziegler, D. Pietschner, S. Herrmann, U. Pietsch, A. Walenta, W. Leitenberger, C. Bostedt, T. Möller, D. Rupp, M. Adolph, H. Graafsma, H. Hirsemann, K. Gärtner, R. Richter, L. Foucar, R. L. Shoeman, I. Schlichting, and J. Ullrich. Large-format, high-speed, X-ray pnCCDs combined with electron and ion imaging spectrometers in a multipurpose chamber for experiments at 4th generation light sources. *Nuclear Instruments and Methods in Physics Research, Section A: Accelerators, Spectrometers, Detectors and Associated Equipment*, 614(3):483–496, 2010.

J. Sun, C. Zuo, L. Zhang, and Q. Chen. Resolution-enhanced Fourier ptychographic microscopy based on high-numerical-aperture illuminations. *Scientific Reports*, 7(1): 1–11, 2017.

A. Suzuki, S. Furutaku, K. Shimomura, K. Yamauchi, Y. Kohmura, T. Ishikawa, and Y. Takahashi. High-resolution multislice X-ray ptychography of extended thick objects. *Physical Review Letters*, 112(5):1–5, 2014.

Y. Takahashi, A. Suzuki, N. Zettsu, Y. Kohmura, Y. Senba, H. Ohashi, K. Yamauchi, and T. Ishikawa. Towards high-resolution ptychographic x-ray diffraction microscopy. *Physical Review B - Condensed Matter and Materials Physics*, 83(21):1–5, 2011.

P. F. Tavares, S. C. Leemann, M. Sjöström, and Å. Andersson. The max iv storage ring project. *Journal of Synchrotron Radiation*, 21(5):862–877, 2014.

P. Thibault and M. Guizar-Sicairos. Maximum-likelihood refinement for coherent diffractive imaging. *New Journal of Physics*, 14, 2012.

P. Thibault and A. Menzel. Reconstructing state mixtures from diffraction measurements supplement. *Nature*, 494(7435):68–71, 2013.

P. Thibault, M. Dierolf, A. Menzel, O. Bunk, C. David, and F. Pfeiffer. High-Resolution Scanning X-ray Diffraction Microscopy. *Science*, 321(5887):379–382, 2008.

P. Thibault, M. Dierolf, O. Bunk, A. Menzel, and F. Pfeiffer. Probe retrieval in ptychographic coherent diffractive imaging. *Ultramicroscopy*, 109(4):338–343, 2009.

A. Tripathi, I. McNulty, and O. Shpyrko. Ptychographic overlap constraint errors and the limits of their numerical recovery using conjugate gradient descent methods. *Optics Express*, 22(2):1452–1466, 2014.

E. H. R. Tsai, I. Usov, A. Diaz, A. Menzel, and M. Guizar-Sicairos. X-ray ptychography with extended depth of field. *Optics Express*, 24(1):29089–29108, 2016.

G. Van Der Schot, M. Svenda, F. R. Maia, M. Hantke, D. P. Deponte, M. M. Seibert, A. Aquila, J. Schulz, R. Kirian, M. Liang, F. Stellato, B. Iwan, J. Andreasson, N. Timneanu, D. Westphal, F. N. Almeida, D. Odic, D. Hasse, G. H. Carlsson, D. S. Larsson, A. Barty, A. V. Martin, S. Schorb, C. Bostedt, J. D. Bozek, D. Rolles, A. Rudenko, S. Epp, L. Foucar, B. Rudek, R. Hartmann, N. Kimmel, P. Holl, L. Englert, N. T. Duane Loh, H. N. Chapman, I. Andersson, J. Hajdu, and T. Ekeberg. Imaging single cells in a beam of live cyanobacteria with an X-ray laser. *Nature Communications*, 6: 1–9, 2015.

I. A. Vartanyants, A. Singer, A. P. Mancuso, O. M. Yefanov, A. Sakdinawat, Y. Liu, E. Bang, G. J. Williams, G. Cadenazzi, B. Abbey, H. Sinn, D. Attwood, K. A. Nugent, E. Weckert, T. Wang, D. Zhu, B. Wu, C. Graves, A. Scherz, J. J. Turner, W. F. Schlotter, M. Messerschmidt, J. Lüning, Y. Acremann, P. Heimann, D. C. Mancini, V. Joshi, J. Krzywinski, R. Soufli, M. Fernandez-Perea, S. Hau-Riege, A. G. Peele, Y. Feng, O. Krupin, S. Moeller, and W. Wurth. Coherence properties of individual femtosecond pulses of an x-ray free-electron laser. *Physical Review Letters*, 107(14): 1–5, 2011.

J. Vila-Comamala, A. Diaz, M. Guizar-Sicairos, A. Mantion, C. M. Kewish, A. Menzel, O. Bunk, and C. David. Characterization of high-resolution diffractive X-ray optics by ptychographic coherent diffractive imaging. *Optics Express*, 19(22):21333, 2011.

D. J. Vine, D. Pelliccia, C. Holzner, S. B. Baines, A. Berry, I. McNulty, S. Vogt, a. G. Peele, and K. a. Nugent. Simultaneous X-ray fluorescence and ptychographic microscopy of Cyclotella meneghiniana. *Optics Express*, 20(16):18287, 2012.

U. Vogt, K. Parfeniukas, T. Stankevic, S. Kalbfleisch, Z. Matej, A. Björling, M. Liebi, G. Carbone, A. Mikkelsen, and U. Johansson. First x-ray nanoimaging experiments at NanoMAX. *Proceedings of SPIE*, 10389(September 2017):103890K, 2017.

B. R. Wasik, S. F. Liew, D. a. Lilien, A. J. Dinwiddie, H. Noh, H. Cao, and A. Monteiro. Artificial selection for structural color on butterfly wings and comparison with natural evolution. *Proceedings of the National Academy of Sciences of the United States of America*, 111(33):12109–14, 2014.

T. Weitkamp, A. Diaz, C. David, F. Pfeiffer, M. Stampanoni, P. Cloetens, and E. Ziegler. X-ray phase imaging with a grating interferometer. *Optics express*, 13(16):6296–6304, 2005.

L. W. Whitehead, G. J. Williams, H. M. Quiney, D. J. Vine, R. A. Dilanian, S. Flewett, K. A. Nugent, A. G. Peele, E. Balaur, and I. McNulty. Diffractive imaging using partially coherent X rays. *Physical Review Letters*, 103(24):1–4, 2009.

P. Willmott. *An introduction to synchrotron radiation*. Wiley, 2011.

L. H. Yu. Generation of intense uv radiation by subharmonically seeded single-pass free-electron lasers. *Physical Review A*, 44(8):5178–5193, 1991.

Y. S. Yu, M. Farmand, C. Kim, Y. Liu, C. P. Grey, F. C. Strobridge, T. Tyliszczak, R. Celestre, P. Denes, J. Joseph, H. Krishnan, F. R. Maia, A. L. Kilcoyne, S. Marchesini, T. P. C. Leite, T. Warwick, H. Padmore, J. Cabana, and D. A. Shapiro. Three-dimensional localization of nanoscale battery reactions using soft X-ray tomography. *Nature Communications*, 9(1):1–7, 2018.

F. Zhang, J. Vila-Comamala, A. Diaz, F. Berenguer, R. Bean, B. Chen, A. Menzel, I. K. Robinson, and J. M. Rodenburg. Translation position determination in ptychographic coherent diffraction imaging. *Optics Express*, 21(11):13592, 2013.